DOE/NV/0003590-43

Development of Upscaling Techniques and Construction of Calibrated Models for Fractured Rocks Using Discrete Fracture Network Approaches

Prepared by

Rishi Parashar, Hai V. Pham, and Nicole L. Sund

Submitted to

U.S. Department of Energy
Environmental Management Nevada Program
Las Vegas, Nevada

November 2019

Publication No. 45289

Nevada System of Higher Education

Available for sale to the public from:

U.S. Department of Commerce
National Technical Information Service
5301 Shawnee Rd.
Alexandria, VA 22312
Phone: 800.363.2068
Fax: 703.605.6880
Email: info@ntis.gov
Online ordering: https://ntrl.ntis.gov/NTRL/

Available electronically at https://www.osti.gov/

DOE/NV/0003590-43

Development of Upscaling Techniques and Construction of Calibrated Models for Fractured Rocks Using Discrete Fracture Network Approaches

Prepared by
Rishi Parashar, Hai V. Pham, and Nicole L. Sund

Division of Hydrologic Sciences
Desert Research Institute
Nevada System of Higher Education

Publication No. 45289

Submitted to

U.S. Department of Energy
Environmental Management Nevada Program
Las Vegas, Nevada

November 2019

The work upon which this report is based was supported by the U.S. Department of Energy under Contract #DE-NA0003590. Approved for public release; further dissemination unlimited.

THIS PAGE LEFT INTENTIONALLY BLANK

EXECUTIVE SUMMARY

The Pahute Mesa Corrective Action Unit on the Nevada National Security Site (NNSS) contains several fractured aquifers that can potentially provide high-permeability pathways for radionuclides to migrate away from underground nuclear testing locations. Although the geometric properties of fractures, such as length and orientation, can be found using geophysical methods and borehole image analyses, the hydraulic property of fractures (which are primarily influenced by apertures) are often unknown or have a high degree of uncertainty attached to their values. The aperture values have a profound impact on groundwater velocity and are critical to understanding transport scales at Pahute Mesa. Fracture aperture values and their distributions also have dominant control over radionuclide transport with potential for long-range correlations or scale-invariant dynamics. Understanding of the small-scale transport variability in fractures could lead to identification of distinct characteristics on larger scales. Furthermore, upscaling techniques need to be developed to adequately predict transport behavior at field scales by capturing the transport trends of smaller scale networks. This report explores these vital modeling needs to understand the role of fractures in Pahute Mesa. Discrete fracture network (DFN) models are the basis for constructing a well-calibrated model to ascertain aperture values of fractures in lava-flow aquifers. These models are also used to develop and compare the usefulness of several random-walk-based models to perform transport upscaling.

Discrete fracture network approaches were designed to capture the high degree of heterogeneity that fractures impart on a flow system, particularly with respect to very broad ranges in fluid flow and solute transport behavior. By solving for flow and transport in individual elements of a fracture network, DFN approaches have an advantage over traditional methods of assigning an upscaled equivalent conductivity tensor and porosity to continuum grid cells because the local density of fracture networks is rarely high enough to satisfy the representative elementary volume criterion. This study used two-dimensional DFN models as the basis for developing random-walk-based upscaling techniques for fractured rocks. The random walk method provided a framework for modeling non-Fickian transport through fracture networks by using probability distributions to generate particle jump lengths and residence times spanning multiple orders of magnitude. The Markov-directed random walk (MDRW), Monte Carlo solution of the Boltzmann transport equation (BTE), and spatial Markov model (SMM) were used to explicitly compare the predictive capability of these models in a variety of scenarios. These upscaling methods were applied in both correlated and uncorrelated forms. For DFNs with low heterogeneity in fracture transmissivity, accounting for correlation generally leads to less accurate predictions. However, as the fracture transmissivity distribution widens, preferential pathways form and correlating the modeling steps becomes important, particularly for early breakthrough predictions.

The three-dimensional DFN code, dfnWorks, was used to develop a calibrated model (using fracture aperture as the calibration tool) for the lava-flow aquifer at the site of the BULLION forced-gradient experiment (FGE). This experiment injected and pumped tracers from a system of three wells to obtain site-specific information about radionuclide transport in fractured rock aquifers at Pahute Mesa in Area 20 of the NNSS. A well package was developed for dfnWorks to develop a high-fidelity model for the BULLION FGE. Six

parameters were introduced to define a well and the connectivity between the well and fracture network. Additionally, the particle tracking code in dfnWorks was modified to track particles to a pumping well.

Verification of the well package against MODFLOW and MODPATH found an excellent match in simulated hydraulic head and particle tracking. By integrating the well package with dfnWorks, multiple conceptual models were developed to simulate flow and transport in subsurface fractured rocks downgradient from the BULLION test. The model domain included the three tracer-test wells of the BULLION FGE and the Pahute Mesa lava-flow aquifer. The model scenarios considered differed from each other in terms of boundary conditions and fracture aperture conceptualizations. For each conceptual model, a number of statistically equivalent fracture network realizations were generated using data from fracture characterization studies. The aperture values in each model were estimated by performing model calibration. Calibrating the DFN model to hydraulic drawdown data limited the range of aperture values. These ranges were further constrained when the DFN models were calibrated to tracer breakthrough data using postprocessors to numerically include the effects of dispersion and matrix diffusion. The fracture aperture values resulting from this study will enhance our understanding of radionuclide transport in fractured rocks and support the development of improved large-scale flow and transport models in Pahute Mesa.

CONTENT

EXECUTIVE SUMMARY iii
LIST OF FIGURES vi
LIST OF TABLES ix
LIST OF ACRONYMS ix
INTRODUCTION 1
DFN METHODS FOR 2-D AND 3-D MODELS 3
2-D DFN 4
3-D DFN: dfnWorks 6
Representation of a Well in 3-D DFN 7
Method Implementation in dfnWorks 9
Verification of the Method 10
Examples to Demonstrate Method Application 12
Discussion of the Method 19
UPSCALING OF TRANSPORT IN 2-D DFNs VIA RANDOM WALK MODELS 20
DFN Simulation Setup 21
Effect of Transmissivity Distribution on DFN Simulations 24
Upscaled Modeling 27
Markov-directed Random Walk (MDRW) 28
Monte Carlo Solution of the Boltzmann Transport Equation (BTE) 29
Spatial Markov Model (SMM) 31
Results 33
Longitudinal Predictions: Error in the Ensemble Cumulative Travel-time Distributions 34
Transverse Predictions: Error in Total Mass in Ensemble Breakthrough Curves 36
Effect of Changing Modeling Scale 38
Discussion of the Methods 39
CALIBRATION OF 3-D DFNs TO FLOW DATA 39
DFN Model Development and Parametrization 40
Model Calibration 41
Case Study: The BULLION Forced-gradient Experiment (FGE) 42
DFN Model for BULLION FGE 43
3-D Fractured Network Generation and Meshing 44

Flow and Transport Simulation 47
Results 52
Simulated Groundwater Levels 52
Impacts of Aperture Distributions 54
Water Flow and Mass Conservation 55
Tortuosity and Breakthroughs 57
Discussion 59
CALIBRATION OF 3-D DFNs TO TRANSPORT DATA 60
Dispersion 60
Matrix Diffusion 62
Metrics to Assess Model Error 63
Results 64
Discussion 66
SUMMARY AND CONCLUSIONS 66
REFERENCES 69

LIST OF FIGURES

1. (a) A fracture network on a 100 m^2 size domain and (b) the connected portion of network after deleting isolated features and dead ends. 4
2. Location of nonzero elements is shown by solid dots in visual representation of the sparsity pattern of a coefficient matrix of size 5340 (99.92 percent elements are zero). 5
3. Comparison between MATLAB and 2-D DFN code solutions for a linear system consisting of 586 fracture intersection points. 6
4. Illustration of a well in a 3-D DFN model that shows: (a) intersections between the well and fractures, (b) the plan view of the well, and (c) the 3-D view of the well intersected by one horizontal fracture. 8
5. Comparison of simulation results of dfnWorks and MODFLOW and MODPATH for (a) simulated hydraulic heads (in meters) and (b) simulated BTCs at the pumping well. 11
6. The configuration of Example 1 showing (a) a DFN network with wells and simulated hydraulic head solution, and (b) a closer look at the pumping well with Delaunay triangulations 14
7. Particle pathlines and BTCs for Example 1 that show particles uniformly distributed over the west side of the model domain ([a] and [b]) and particles uniformly distributed at the injection well ([c] and [d]). 15

8. Simulated BTCs using four different values of injection well skin permeability for: (a) Example 1, the 100 m DFN model; and (b) Example 2, the 500 m DFN model. 16

9. Simulated BTCs using five different values of injection well skin radii for: (a) Example 1, the 100 m DFN model domain; and (b) Example 2, the 500 m DFN model domain..... 17

10. Simulated steady-state hydraulic heads and particle pathlines for the 3-D DFN of Example 3: (a) 3-D perspective of the hydraulic head distribution, (b) a top view, and (c) a ZX cross-sectional view..... 18

11. Modeling domain: one realization of a DFN with injection region highlighted in red and parameterization region highlighted in yellow. 22

12. Fracture flux magnitude for various values of the standard deviation of the transmissivity distribution (σ): (a) PDF ($f_{|q|}(x)$) and (b) complementary cumulative density function (CCDF) ($(1-F_{|q|}(x))$. 25

13. Flux magnitude ($\log_{10}(|q|)$) distribution for one realization of each transmissivity distribution of the DFN (top) $\sigma = 0$, (center) $\sigma = 0.5$, and (bottom) $\sigma = 1$. 26

14. Method for partitioning particle trajectories into MDRW modeling steps..... 28

15. Ensemble averaged transition matrix ($P(q_n \in s_i | q_{n-1} \in s_j)$) over all realizations with modeling step size $k = 1$ fracture segments for transmissivity distributions with (a) $\sigma = 0$, (b) $\sigma = 0.5$, and (c) $\sigma = 1$. 29

16. Ensemble averaged transition matrix ($P((q_n, \theta_n) \in si | (q_{n-1}, \theta_{n-1}) \in s_j)$) over all realizations with modeling step size $k = 1$ fracture segments for transmissivity distributions with (a) $\sigma = 0$, (b) $\sigma = 0.5$, and (c) $\sigma = 1$. 31

17. Ensemble averaged transition matrix ($P(\delta t_n \in s_i | \delta t_{n-1} \in s_j)$) over all realizations with modeling step size $L_k = 1$ (the average length of 1 fracture segment) for transmissivity distributions with (a) $\sigma = 0$, (b) $\sigma = .5$, and (c) $\sigma = 1$. 32

18. Ensemble cumulative and complementary cumulative travel time distributions at $x = 500$ m of DFN simulations and of upscaled random walk model simulations with modeling step size $k = 1$ with transmissivity distributions (a) $\sigma = 0$, (b) $\sigma = .5$, and (c) $\sigma = 1$, and (d) the corresponding relative error. The range of errors among individual realizations are also shown with error bars for the upscaled models and with a shaded yellow region for the DFN simulations. 35

19. Ensemble cumulative and complementary cumulative travel time distributions at $x = 1$ km of DFN simulations and of upscaled random walk model simulations with modeling step size $k = 1$ with transmissivity distributions (a) $\sigma = 0$, (b) $\sigma = 0.5$, and (c) $\sigma = 1$, and (d) the corresponding relative error. 36

20. Total mass in ensemble breakthrough curves of DFN simulations and of upscaled random walk model simulations with modeling step size $k = 1$ with transmissivity distributions (a) $\sigma = 0$, (b) $\sigma = 0.5$, and (c) $\sigma = 1$, and (d) the corresponding average relative error. 37

21. Relative errors in upscaled ensemble random walk model simulations as a function of modeling scale for $\sigma = 0$: (a) relative error in cumulative breakthrough at $X = 1$ km and (b) average relative error in mass. 38

22. Location of the BULLION FGE in Pahute Mesa of the Nevada National Security Site. 42

23. Fracture sizes and their distributions for each of the five fracture families for a realization. 46

24. A DFN realization showing (a) all five fracture families, (b) cooling joints SP, (c) cooling joints DP, (d) cooling joints BP, (e) tectonic fracture T1, and (f) tectonic fracture T2. 47

25. The simulated number of fracture intersections at three wells in the model domain. ... 49

26. Model calibration convergence profile for the three conceptual models under BC2 boundary conditions. 51

27. Fracture apertures of three calibrated DFN models under the BC2 boundary conditions. 52

28. Model calibration results with the optimal model parameters: (a) CFA-BC1, (b) LOG-BC1, (c) LCA-BC1, (d) CFA-BC2, (e) LOG-BC2, and (f) LCA-BC2. 53

29. Simulated steady-state groundwater level solution for a calibrated model using the length-correlated fracture apertures. 54

30. Impact of aperture distributions on simulated groundwater levels for (a) LNA models where standard deviations of fracture apertures were varied from 144.39 microns to 271.81 microns. The mean was fixed at 487 microns; and (b) LCA models where standard deviations of fracture apertures were varied from 54.67 microns to 80.25 microns. The mean was fixed at 241 microns. 55

31. Simulated water inflow and outflow from the model domain: (a) CFA-BC2, (b) LNA-BC2, and (c) LCA-BC2. 56

32. Simulated particle travel lengths from well ER 20-6 #1 to well ER 20-6 #3. 57

33. Simulated breakthrough curves for the three calibrated models under BC2 boundary conditions: (a) CFA-BC2, (b) LOG-BC2, and (c) LCA-BC2. 58

34. Comparison between observed breakthrough curve (actual) and postprocessed breakthrough curve for: (a) CFA model using BC1, (b) CFA model using BC2, (c) LNA model using BC1, (d) LNA model using BC2, (e) LCA model using BC1, and (f) LCA model using BC2. 65

LIST OF TABLES

1. Parameters used for three hypothetical examples. 13
2. Configurations of Examples 1 and 2 to evaluate the influences of well skin radius and permeability on simulated BTCs at a pumping well. Particles are released at an injection well. 16
3. Fracture statistics used to generate 3-D fracture networks. 44
4. Statistics of 30 DFN realizations before and after eliminating isolated fractures. 45
5. Optimized fracture apertures and errors between observed and simulated groundwater levels at two observation wells. Fracture apertures were averaged over 30 DFN realizations and after deleting isolated fractures. 50
6. Best-fit values for the parameters of the memory kernel and the error metrics for various aperture distribution models under BC1 and BC2. 64

LIST OF ACRONYMS

2-D	two-dimensional
3-D	three-dimensional
ADE	advection-dispersion equation
BC	Boundary Conditions
BTC	breakthrough curve
BTE	Boltzmann transport equation
CCDF	complementary cumulative density function
CDF	cumulative density function
CFA	constant fracture apertures
CHB	constant head boundary
CTRW	continuous time random walk
DFN	discrete fracture network
DOE	Department of Energy
DRI	Desert Research Institute
EPM	equivalent porous medium
FGE	forced-gradient experiment
FRAM	feature rejection algorithm for meshing
GB	gigabyte

HGU	hydrogeologic unit
km	kilometer
LANL	Los Alamos National Laboratory
LCA	length correlated aperture
LFA	lava-flow aquifer
LNA	lognormal distribution aperture
LPF	layer property flow
m	meter
m/s	meters per second
MAE	mean absolute error
MDRW	Markov-directed random walk
NNSS	Nevada National Security Site
Pa	pascal
PDF	probability density function
SMM	spatial Markov model
TCU	tuff confining unit
UGTA	Underground Test Area
USGS	U.S. Geological Survey
WPM	Western Pahute Mesa
WTA	welded-tuff aquifer
VTA	vitric-tuff aquifer

INTRODUCTION

Fracture aperture has immense influence on flow and transport, and therefore reducing its uncertainty is key to developing a model that accurately describes groundwater velocity. The difficulty of establishing representative elementary volume is that fractured rocks, particularly in case of sparse to moderately dense networks, also necessitate the development of upscaling methodologies to successfully capture trends at smaller scales that can be used to predict behavior at larger scales. This report documents the development and application of two-dimensional (2-D) and three-dimensional (3-D) discrete fracture network (DFN) models using both site-specific fracture attributes from Western Pahute Mesa (WPM) and generic networks to study techniques for upscaling transport and calibrating DFN models with respect to observed field data. Fracture aperture was used as a calibration tool in the DFN models, which resulted in a more realistic and less uncertain measure of this important network property.

Groundwater flow and transport within Pahute Mesa are largely dictated by the highly variable hydraulic properties of the volcanic rock within the area. The eruption and cooling patterns, degree of welding, and pervasiveness of primary and secondary fracturing determine these properties. Ash-flow tuff is prevalent in many of the volcanic rock aquifers in the northern portion of the Nevada National Security Site (NNSS). These units have a high tendency of fracturing and can form well-connected fracture networks if they are densely welded (Fenelon *et al*., 2010). As depositional welding increases between volcanic rocks, there is a reduction in bulk porosity but an increase in fracture permeability and connectivity. Complex stratigraphic sequences are produced and welded zones form between nonwelded segments. Partially/nonwelded tuff that has undergone burial in saturated conditions normally has a lower permeability and less extensive fracturing, which creates a volcanic confining unit (Drellack *et al*., 1997)). Because of the layering nature of the volcanic rocks, highly conductive units are often interbedded with less conductive units in an alternating pattern with frequent stratigraphic juxtapositions along faults (Fenelon *et al.*, 2010). Rhyolitic lava-flow units are also found in Pahute Mesa as a caldera-filling unit and are characterized by a wide range of transmissivities and water yield potentials. Both lava-flow and partially to densely welded ash-flow tuffs often form aquifers because of their tendency to form highly permeable and connected fracture networks. These extensively layered volcanic aquifer systems may preclude the vertical flow of water and contaminants between units, resulting in a largely horizontal transport for each layer.

In fractured geologic media, fractures (e.g., joints, faults, and veins) and fracture networks are often complex because of their naturally occurring discontinuities. Therefore, they are the principal pathways for fluids. Fractures are spatially discontinuous features that exhibit strong variability in geometric and hydraulic properties. This variability is a result of the complex interplay between current and past stress fields, rock mechanical properties (i.e., Young's modulus and Poisson's ratio), mechanical fracture interactions, and distributions of flaws or weakness in a rock mass. Fractures provide the bulk of transport for contaminants in many geologic formations. Movement of contaminants in fracture networks is often characterized by the presence of preferential pathways along which the plume moves rapidly. The linear motion of contaminants along fracture segments and their residence time in a fracture network depend on both the fluid flow and the fracture network characteristics (Reeves *et al.*, 2008). The combination of randomly varying fracture attributes spread over

several orders of magnitude gives rise to a flow field, which is highly heterogeneous and anisotropic. Therefore, the resulting plume geometry can form highly variable shapes that are dramatically different from the ones observed in homogeneous porous media systems.

The traditional advection-dispersion equation (ADE) was derived for transport in a relatively homogeneous geologic media that facilitates the dispersive growth described by Fick's Law (Bear, 1972). In the case of a fractured media in which transport is driven by a heterogeneous and anisotropic permeability field, the classical ADE is often found to be inadequate in capturing the dynamics of contaminant migration (Schumer *et al.*, 2001). In many cases, solute particles will move at a super-Fickian rate, meaning that the dispersive growth of the plume will be faster than the linear rate of growth of variance with respect to time as predicted by the classical ADE model (Elfeki *et al.*, 1997). In a homogeneous geologic media, solute particles make short jumps in random directions guided by the flow field in a process akin to the Brownian motion, altering their path as they come in contact with the surrounding environment. In fractured rocks, the jump length (the linear motion along a single fracture) experienced by migrating particles may span multiple orders of magnitude. Therefore, the transport process in fractured media becomes more complex not only because of the large variations in length of the forward linear motions, but also because of the rate at which those motions occur.

Fractured rock masses are typically characterized during field campaigns that measure fracture attributes from a number of sources, such as boreholes, rock outcrops, road cuts, and tunnel complexes. Seismic techniques can also be used to image fault structures in the subsurface. Hydraulic properties of fractured media can be either inferred from the fracture aperture or hydraulic tests performed on boreholes. Fracture length, density, orientation, aperture, and connectivity are all needed to construct an accurate representation of a fracture network in transport models (Parashar and Reeves, 2012). The distribution of fracture length is a factor that has a strong influence on the connectivity of a network (Wellman *et al.*, 2009). Fracture lengths provide a control on the uninterrupted jump distance experienced by a particle moving through the system. Therefore, longer fractures tend to provide proportionally longer travel times than shorter fractures when transmissivity and aperture are constant (Darcel *et al.*, 2003; Reeves *et al.*, 2012).

The fracture density of a network denotes the total length of all fracture segments in a given area. Increasing the fracture density increases connectivity in the network and the migrating particles tend to sample a higher number of fractures, resulting in transport that is more similar to that of movement through homogenous media. Variation in fracture density from a very sparse to highly dense network tends to have a nonmonotonous effect on particle arrival times. A sparse network may result in long arrival times because shorter pathways to the domain boundaries are often not available. A highly dense network may also result in long arrival times because of the many tortuous pathways that connect the source location to the domain boundary. This also affects the plume geometry and the amount of spreading because the fractures sampled by the particles play a key role in determining the relative distances between the particles as time progresses and the rate at which they converge or diverge in space (Smith and Schwartz, 1984; National Research Council, 1996; Darcel *et al.*, 2003). It is only at an extremely high fracture density that particles travelling through the network will experience enough unresolved heterogeneities that the transport pattern and plume growth rate will begin to resemble movement through a homogeneous medium.

Aperture is the characteristic length between two walls of a fracture. A larger aperture allows for a higher volume of fluid flow to occur through a particular segment of the network, whereas a smaller aperture restricts the occurrence of flow through a segment of the network (Smith and Schwartz, 1984).

The orientation of a fracture is represented by its dip and strike angle in three dimensions and by the angle the fracture trace lengths make with the axis of reference in two dimensions. Fractures in a given set are typically grouped around a mean orientation with some amount of dispersion to represent variability about the mean. Less dispersion around the mean orientation results in a more uniform fracture ensemble (i.e., a higher number of fractures closer to the mean orientation) and can either decrease or increase arrival times depending on the relation of the fracture orientation with the hydraulic gradient. More dispersion in the distribution of angles typically leads to larger spread in the plume geometry in sparsely to intermediately dense networks (Rouleau and Gale, 1985; Wellman *et al.*, 2009; Reeves *et al.*, 2012).

Of the approaches to solve for flow and transport through fractured rocks (Sahimi, 2011; Hadgu *et al.*, 2017), DFN modeling has advanced significantly with the increase in computational power and the wide availability of high-performance computing systems. The DFN explicitly represents individual fractures. It assumes the rock matrix is impermeable and fluid flow can only occur through a connected fracture network (Cacas *et al.*, 1990a,b; Dershowitz *et al.*, 1993; Erhel *et al.*, 2009; Pichot *et al.*, 2012; de Dreuzy *et al.*, 2012; Parashar and Reeves, 2012; Reeves *et al.*, 2013; Hyman *et al.*, 2015a; Huang *et al.*, 2016). By including a detailed geometric representation of the connectivity structure in a network, DFN models allow for more accurate predictive simulations of flow and transport through fractured rocks. Discrete fracture network approaches are favored in mechanistic studies because the local density of fracture networks is rarely sufficient for the representative elementary volume criterion to be satisfied, and traditional approaches of assigning an equivalent conductivity tensor and porosity to continuum grid cells tend to overly homogenize the representation of networks (Berkowitz, 2002; Hagdu *et al.*, 2017; Neuman, 2005, 2008; Klimczak *et al.*, 2010). Despite their high computational expense, DFN simulations produce realistic distributions of velocity that result from multiscale heterogeneity and fracture connectivity that often manifest as rapid transport in longer, highly connected fracture segments and retention in weakly connected fractures. Using DFNs to develop high-fidelity models for fractured rocks is supported by several studies that have successfully linked fracture network attributes to fluid flow and solute transport behavior (Smith and Schwartz, 1984; Reeves *et al.*, 2008b,c, 2014; Zhang *et al.*, 2013; Kang *et al.*, 2015a; Parashar and Reeves, 2017).

DFN METHODS FOR 2-D AND 3-D MODELS

The DFN models were constructed by incrementally adding fractures with random attributes (e.g., orientation, length, aperture, and location) to a network until a specified density criterion was reached. Models included both deterministic and stochastic features, and the process consisted of selecting the length values and orientations from separate, specified distributions. This section provides a brief summary of Desert Research Institute's (DRI) in-house 2-D DFN code and the 3-D DFN suite of software, dfnWorks, developed at the Los Alamos National Laboratory (LANL). A well package was developed at DRI for

dfnWorks, the details of which are also provided in this section. The 2-D DFN models, less computationally intensive than the 3-D models, allows for construction of large scale models and hence are used in this study to explore development of upscaling techniques for fractured media. The 3-D models on the other hand are used in this study to understand dynamics of flow and transport at more limited scale where the accuracy of predictions and investigation of the influence of various parameters on flow and transport simulations justifies the higher computational cost.

2-D DFN

The 2-D DFN flow and transport computation and fracture mapping code was developed at DRI during a previous project supported by the Department of Energy (DOE) at the NNSS (Reeves *et al.*, 2014). The code was reviewed by Underground Test Area (UGTA) participants for: (1) correctness of equations algorithms and numerical solution techniques, (2) conformance of methods to accepted/published concepts, (3) code functional requirements and verification, (4) test problems and acceptance criteria, and (5) documentation to ensure proper installation.

There are a number of inputs to the DFN code that allow the user to create network length characteristics through fracture generation. One of these inputs is the length of the initial fractures themselves. The input of a minimum fracture length allows the user to condition the smallest sizing of the initial fractures. Fractures can be stochastically generated until a user-designated network density threshold is reached. For a 2-D network, this is defined as the total length of all fractures divided by the domain area (Parashar and Reeves, 2012). Using a seed number to initialize the random variates for each run allows the program to recreate a statistically similar network for a set of conditions. Once the raw fracture file is generated, further geometric analyses can be conducted to determine the number of times a fracture is intersected by other fractures in the network, and the corresponding distribution of segment lengths. The code is also designed to scan the network for clusters, individual fractures that are unconnected to the rest of the networks, and dead-end portions. Figure 1 shows a process that removes these isolated fractures to help extract the connected portion of the network.

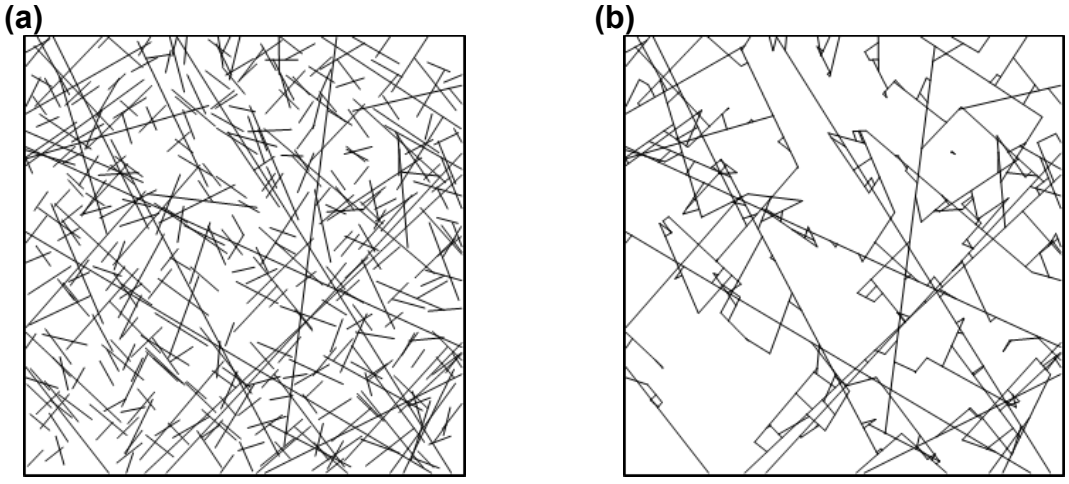

Figure 1. (a) A fracture network on a 100 m^2 size domain and (b) the connected portion of network after deleting isolated features and dead ends.

The DFN models are computationally intensive and the central feature of the code is computation of flow in fracture segments, which results in a set of N linear algebraic equations of hydraulic head h (N being the total number of points at which two fractures intersect). The equations are cast in matrix form $AX = B$, where A is an N x N diagonally dominant sparse matrix representing the connectedness of internal nodes, X is the vector of unknowns (the value of hydraulic head at the internal nodes), and B is the known vector defining the connection between the boundary nodes and the internal nodes. The sparsity pattern of the coefficient matrix is irregular and it is not unreasonable to expect that more than 99.9 percent of the matrix elements equal zero for a moderately sized network (see Figure 2). The eigenvalues of such matrices are spread over several orders and lack the clustering necessary for the fast convergence of iterative techniques for linear systems (Parashar and Reeves, 2012). The matrices are iteratively solved using either a biconjugate gradient solver or a minimum-residual method for sparse matrices. These methods are part of Krylov subspace's Lacoz biorthogonalization methods, the details of which can be found in advance linear algebra texts. Figure 3 shows the verification check for the biconjugate gradient solver in the 2-D DFN code by comparing the solution obtained from the coded subroutine to the solution obtained using MATLAB.

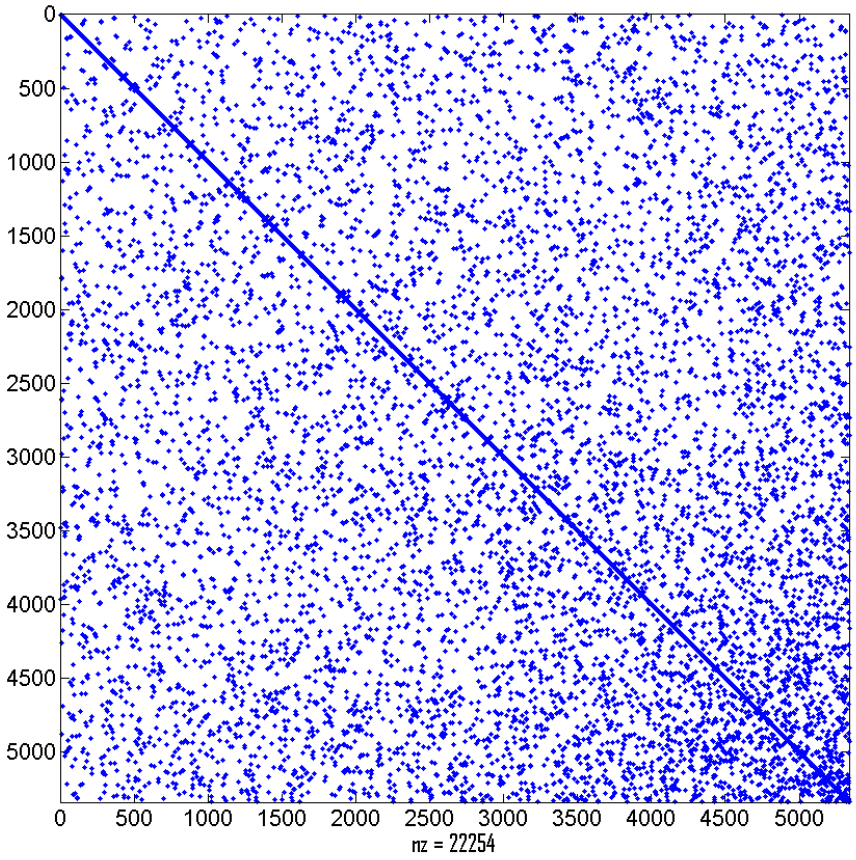

Figure 2. Location of nonzero elements is shown by solid dots in visual representation of the sparsity pattern of a coefficient matrix of size 5340 (99.92 percent elements are zero).

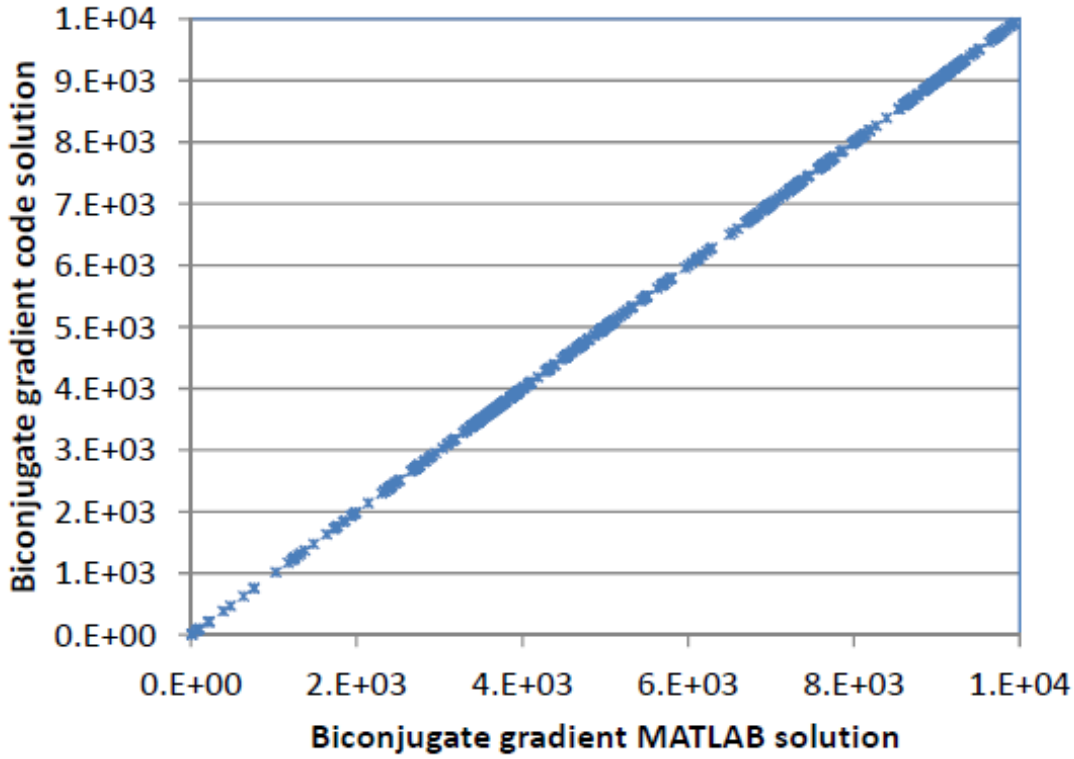

Figure 3. Comparison between MATLAB and 2-D DFN code solutions for a linear system consisting of 586 fracture intersection points.

3-D DFN: dfnWorks

The computational suite dfnWorks (Hyman *et al.*, 2015a) is a state-of-the-art DFN simulator that solves for fluid flow and Lagrangian solute transport within complex, 3-D fracture networks. dfnWorks has three modules: dfnGen, dfnFlow, and dfnTrans. dfnGen stochastically generates 3-D DFNs, removes isolated fractures using the feature rejection algorithm for meshing (FRAM) (Hyman *et al.*, 2014), and creates high-quality conforming Delaunay triangular meshes on the generated DFNs using the LaGriT meshing toolbox (George *et al.*, 1999). Near fracture intersections, the mesh is refined to allow for smooth and accurate representation of high-pressure gradients and sharp velocity contrasts. Discretization of the mesh coarsens farther away from fracture intersections to reduce computational costs. Once a network is constructed and meshed, the dfnFlow module solves for steady-state or transient saturated flow conditions using the massively parallel, open-source, subsurface flow and reactive transport finite volume code PFLOTRAN (Lichtner *et al.*, 2015). dfnTrans, an extension of the Walkabout particle tracking method (Painter, 2011; Painter *et al.*, 2012; Makedonska *et al.*, 2015), is used to determine pathlines through the DFN and simulate solute transport. The dfnWorks suite has been successfully applied in the areas of nuclear waste repository science, hydraulic fracturing, and CO_2 sequestration (Hyman *et al.*, 2015b, 2016; Karra *et al.*, 2015; O'Malley *et al.*, 2015; Makedonska *et al.*, 2016; Hyman and Jiménez-Martínez, 2018; Hyman *et al.*, 2018). The entire workflow of dfnWorks 1.0 was validated in Hyman *et al.* (2015a).

In its current form, dfnWorks does not include a well package. Therefore, this study developed a method to represent wells in 3-D DFN models and applied it to site-specific models. The method was validated against numerical solutions using MODFLOW (Harbaugh, 2005), MODPATH (Pollock, 2012), and three hypothetical examples. The details of this well package are provided below.

Representation of a Well in 3-D DFN

In DFN models, fractures are randomly generated and placed in the model domain. The volume of fractures is often very small compared with the volume of the rock matrix. As a result, computational cells on a planar fracture may not be available at the necessary location to represent a well (Figure 4a, Well 1 has no intersections with the fracture backbone). Furthermore, fracture planes may only represent a small portion of the well screen (Figure 4a, Well 2 only intersects one fracture in the well screen interval). This study introduced a conceptualization that used two rectangular fractures to represent a well in a 3-D DFN model, as shown in Figure 4. Alternative conceptualization of wells such as line elements (2-noded elements) are not amenable for integration with a finite elements based code such as dfnWorks. The two fractures were orthogonal and of equal width and length. Additional parameters used to define a well included: (1) well screen top (z_{top}), the top of the open, saturated well-screen interval equals the top of the two fractures (note that unsaturated conditions cannot be simulated here as the cubic law requires the void space between fracture walls to be completely filled by water); (2) well screen bottom (z_{bot}), the bottom of the open well-screen interval equals the bottom of the two fractures; (3) well radius (r_w), the distance from the center of the well to the inner edge of the well casing (as shown in Figure 4b), which is always kept equal to the actual well radius; and (4) the permeability of the well screen (k_w). The area defined by z_{top}, z_{bot}, and r_w represents the well screen. The first three well parameters were determined based on well construction diagrams. The last parameter was used to assign high permeability to the well screen. Because the permeability of well-sorted gravel can be as high as 10^{-7} m^2 (Bear, 1988), this study assigned $k_w = 10^{-7}$ m^2 to allow free movement of water in the well screen area. The purpose of this conceptualization was to model a typical water well that had well casing and well screens with packing material in the annular space between the well screen and the borehole wall. For a well without well screens, z_{top} can be equal to the top of the saturated borehole and z_{bot} can be equal to the bottom of the borehole.

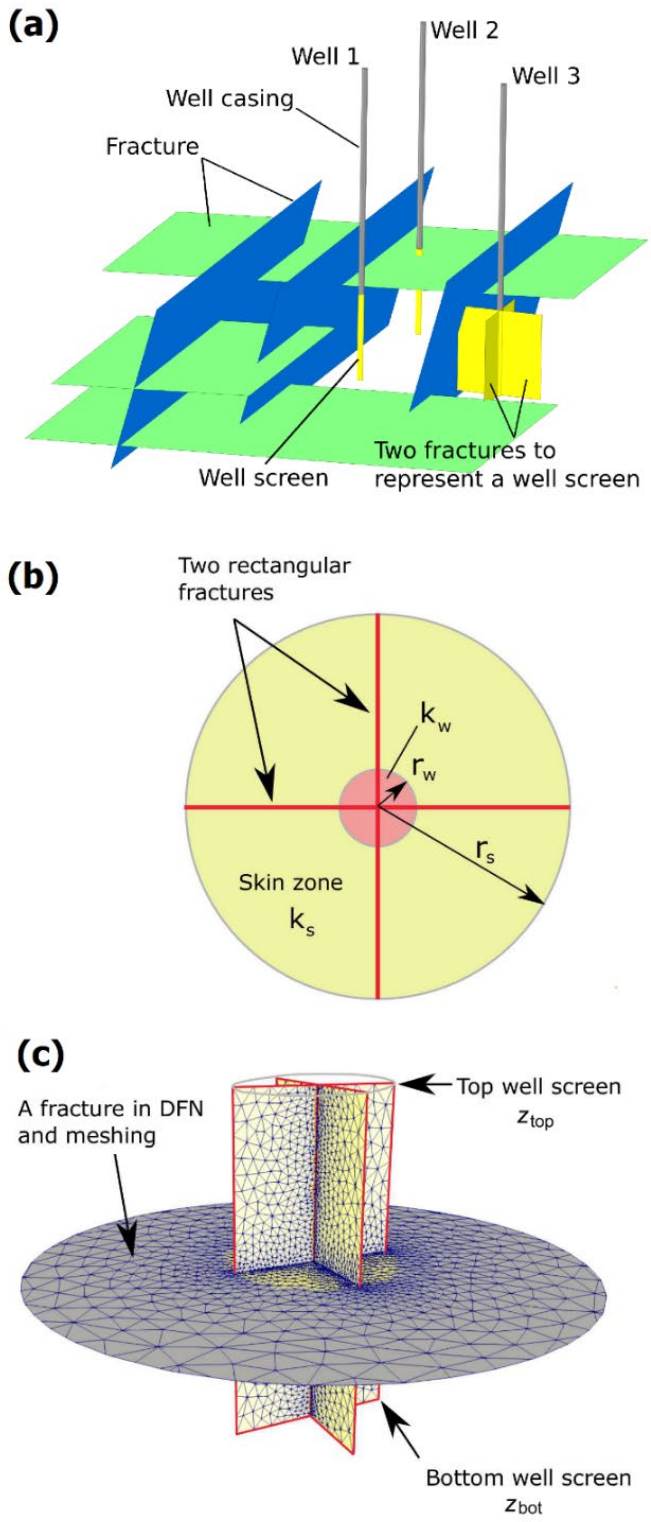

Figure 4. Illustration of a well in a 3-D DFN model that shows: (a) intersections between the well and fractures, (b) the plan view of the well, and (c) the 3-D view of the well intersected by one horizontal fracture. Blue solid lines show the Delaunay triangulations. The mesh is coarsened as the distance from the well center increases.

In reality, a water well often has a small diameter (on the order of inches). However, small well diameters run the risk of having no intersection between a well and fractures in the DFNs. Additionally, a small well diameter requires an extremely small cell size in discretizing the well screen. As a result, dfnWorks may fail to converge when simulating a pumping well and resolving flux and hydraulic gradient over very small lengths. To overcome these issues, this study introduced two nonphysical parameters (i.e., a parameter not related to the physical design of the borehole or screen interval) to define a well. The first parameter was the well skin radius (r_s), which is the distance from the axis of the well to the outer edge of the skin zone. The term 'skin zone' here should not be confused with the physical zone of enhanced or reduced permeability around a borehole formed during the completion of a well. The term 'skin zone' is an artificial construct here (without any connection to a physically measureable quantity) intended to be carefully adjusted in simulations to provide desired level of connection between a well and the rest of the fracture network. This parameter controls the connection between a well and fracture backbones, and it can be increased to enhance the connectivity. The well skin radius needs to be large enough to allow at least one intersection between the well and fracture backbones. Using too small of r_s may lead to no intersections, or a small number of intersections between the well and the surrounding fractures. Using too large of r_s may lead to an overestimation of intersections. Therefore, it is best to constrain this value to observed fracture intensity, P_{10} (i.e., the number of fractures per unit length of borehole), where possible. The second parameter is well skin permeability (k_s), which represents the permeability of the area around a well screen. In practice, this parameter would mainly depend on the permeability of rock matrix, drilling equipment, and drilling methods. The well skin permeability is difficult to measure. A good starting point to fix the value of well skin permeability in DFN simulations is to make it equal to the value of the rock matrix permeability. The well skin radius and the well skin permeability are the most important components of this well package because they provide the necessary connection between a well and the fractured aquifer.

Computational issues may arise from using rectangular orthogonal fractures to represent the well radius, r_w. The DFN models assume that the rock matrix is impermeable and often ignore tiny fractures (submeter scale) to stay within computational constraints. In reality, rock matrix does conduct flow (albeit small), and tiny fractures do play a role in defining connectivity between a well and the fracture backbones. The roles of rock matrix and tiny fractures are especially important near pumping wells because the large head gradient can induce a significant amount of flow. In our conceptual model, the well skin zone was a substitute for the rock matrix and tiny fractures.

Method Implementation in dfnWorks

Defining two orthogonal rectangular fractures in dfnWorks is straightforward. Two additional tasks to successfully integrate a well in dfnWorks are: (1) to identify cells that represent a well and (2) to assign a pumping rate for each cell in the well zone.

For the first task, LaGriT was used to identify the model cells that represented the well screen and the well skin zone in the same way that dfnWorks identifies boundary cells. The file "lagrit_scripts.py" in dfnWorks was modified to include this enhancement. Figure 4c shows the discretization of the well screen into multiple finite element cells. Total volumetric flow rate of a pumping well is:

$$Q = \sum_{i=1}^{n} Q_i \tag{1}$$

where n is the total number of model cells representing the well screen, i is the index, and Q_i is the flow at the ith cell of the well screen. For the second task, a built-in function in PFLOTRAN was used to assign a flow rate for a pumping well. Depending on which scaling options are selected, the total volumetric flow rate of a pumping well can be allocated for the pumping cells as: (1) a function of cell volume and permeability, (2) a function of the interfacial area and permeability of neighboring cells, and (3) a function of cell volume. Therefore, a pumping cell that has a large cell volume, high permeability, and/or large interfacial area of neighboring cells will be assigned a higher pumping rate. Because the permeability values assigned to all pumping cells are the same in our method, Option 1 is equivalent to Option 3. Option 2 is recommended when there is a significant difference in the permeability between k_s and k_w. Injection wells can be simulated in the same way as pumping wells, except that the flow rate is positive instead of negative.

Tracking particles to a pumping well was modified in dfnWorks such that if any particles at any time intersected the well screen (i.e., the horizontal distance between a particle and pumping well is less than or equal to r_w), they were removed from the system and the particle tracking for that particle ends. dfnWorks outputs flow solutions at all model cells in terms of hydrostatic pressures. This study developed a code to convert pressure values into hydraulic head because hydraulic head data are widely available for model calibration in groundwater modeling studies. Three dfnWorks source files (i.e., lagrit_scripts.py, flow.py, and TrackingPart1.c) were modified in this study to incorporate wells and track particles to a pumping well. Several new parameters were added to the input files of dfnWorks. To access the well package, a user would need to update these files before installing dfnWorks 2.0.

Verification of the Method

The proposed method was verified against U.S. Geological Survey (USGS) MODFLOW (Harbaugh, 2005) and MODPATH (Pollock, 2012) models. MODFLOW simulates groundwater flow through porous media using the equivalent porous medium (EPM) modeling approach. However, it can be used to design a numerical test to verify the methods and codes introduced, such as a system of two parallel rectangular fractures with a pumping well in the center. Fractures can be represented by a microscale-layer-thickness model and the impermeable rock matrix around the fractures can be represented as aquitards. MODPATH is a particle-tracking, postprocessing program that computes 3-D flow paths using output from MODFLOW. The verification focused on the accuracy of the hydraulic head simulations (excluding the heads at the location of the well) and tracking particles into a well.

dfnWorks was used to create a simple DFN model with two deterministic rectangular fractures in a model domain of 100 m × 100 m × 10 m. The fractures were 100 m × 100 m, placed in the horizontal plane, and crosscut four sides of the model domain. The fracture apertures were fixed at 200×10^{-6} m. The well screen intervals were 10 m and spanned the entire domain thickness. The pumping well was placed in the middle and constant hydraulic

heads were assigned at the four sides of the model domain. The top and bottom of the model domain were assigned no-flow boundary conditions. Particles were released uniformly at the left of the model domain, on the edge of each fracture.

This DFN model can be interpreted as an EPM model that includes five model layers. Layers 1, 3, and 5 are aquitards that represent impermeable rock matrix. Layers 2 and 4 are aquifers that represent the two fractures with the aquifer thickness equal to the fracture aperture. For the flow model, the layer property flow (LPF) package in MODFLOW was used to specify properties controlling flow between cells. The time-variant specified head (constant head boundary [CHB]) package was used to assign constant heads for all cells on the side boundaries. The well was represented by two model cells, one in Layer 2 and the other in Layer 4, and simulated using the WEL Package. MODPATH (Pollock, 2012) was used to track the movement of conservative particles to the pumping well.

The cubic law (Witherspoon *et al.*, 1980) was used to relate fracture aperture to fracture hydraulic conductivity:

$$K_f = \frac{b^2 \rho g}{12\mu} \tag{2}$$

where K_f is fracture hydraulic conductivity, a is fracture aperture, ρ is the water density, g is the acceleration because of gravity, and μ is the dynamic viscosity. Using $b = 200\text{x}10^{-6}$ m, $\rho = 997.16$ kg/m^3, $g = 9.81$ (m/s^2), and $\mu = 8.9\times10^{-4}$ kg/(m.s) at 25^{0}C resulted in $K_f = 3{,}163$ m/day. By rearranging Equation 2 and using the relation of hydraulic conductivity to permeability, the fracture permeability is $\kappa = b^2/12 = 3.33\times10^{-9}$ m^2.

dfnWorks and MODFLOW were run in steady state and particle travel times were grouped into one-hour increments. The simulated hydraulic heads (Figure 5a) and breakthrough curves (BTCs) showed a perfect match at the pumping well (Figure 5b). This verified the successful implementation of the proposed method in dfnWorks.

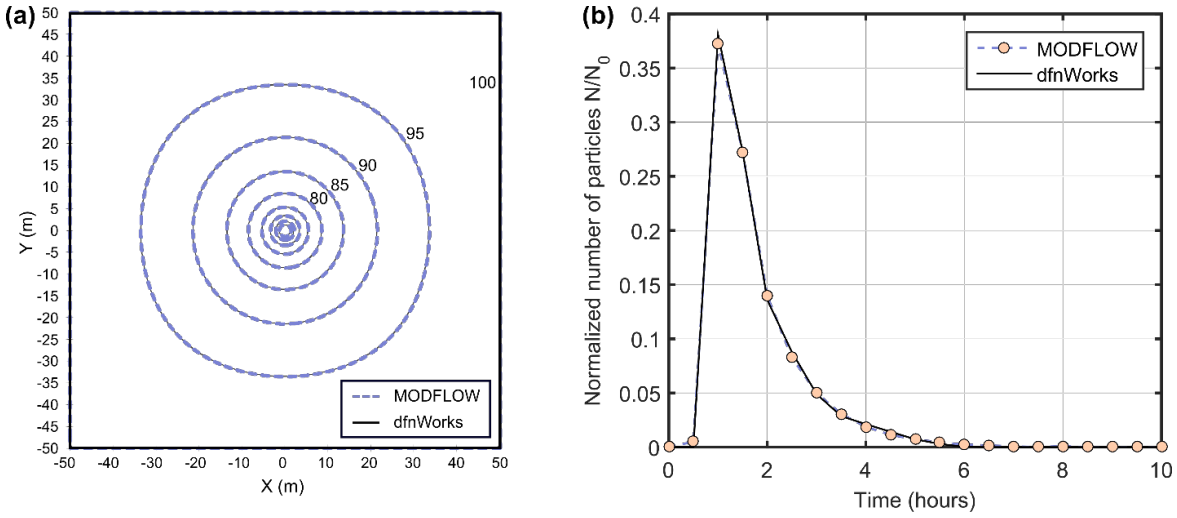

Figure 5. Comparison of simulation results of dfnWorks and MODFLOW and MODPATH for (a) simulated hydraulic heads (in meters) and (b) simulated BTCs at the pumping well.

The following section uses three hypothetical examples to investigate: (1) how to assign well skin radius and permeability values, and (2) determine the influence of these two parameters on transport simulations.

Examples to Demonstrate Method Application

Examples 1 and 2 use deterministic DFNs (which are different from the stochastic DFN used in Example 3) to investigate questions about the well skin radius and permeability given different model domain sizes. For Example 1, a DFN model was created using four deterministic rectangular fractures in a cubic model domain of 100 m in each dimension. Of these fractures, three were in the horizontal direction and one was in the vertical direction (Figure 6). All four fractures were 100 m × 100 m and crosscut four sides of the model domain. Two wells were placed at different depths within the model domain. The injection well was placed at $x = -25$ m, $y = 0$ m and the pumping well was placed at $x = 25$ m, $y = 0$ m. The well screens were 10 m long and located from $z = -25$ m for the pumping well and to $z = 25$ m for the injection well. Constant hydraulic heads were assigned to the four sides of the model domain. The top and the bottom of the model domain were assigned no-flow boundary conditions. Pumping rates were scaled by cell volume, which means that the assigned pumping rate of 10^{-4} m^3/s was proportionally distributed among the pumping cells based on the cell volumes. For Example 2, a DFN similar to the one in Example 1 was generated, except the model domain was 500 m × 500 m × 100 m; the injection well was placed at $x = -250$ m, $y = 0$ m; and the pumping well was placed at $x = 250$ m, $y = 0$ m.

Example 3 was inspired by a case study at the BULLION forced-gradient experiment (FGE) (IT Corporation, 1998; Reimus and Haga, 1999) with the hope that the method would mimic a tracer experiment in fractured geologic media. The BULLION FGE was a tracer experiment designed to obtain site-specific information about the transport of radionuclides in saturated fractured volcanic rock at Pahute Mesa in Area 20 of the NNSS. Three wells were installed downgradient from the location of the BULLION test. The well farthest from the test was pumped to produce a hydraulic gradient while tracers were injected into the other two wells. The model domain was 250 m × 250 m × 100 m in which fractures were uniformly distributed with random dip and random strike. Fracture sizes followed a truncated power law distribution with a power law exponent of 2.5 and had minimum and maximum sizes of 2 m and 500 m, respectively. The boundary conditions were the same as Example 1. In the steady-state condition (before pumping), a hydraulic head of 250 m was applied to the bottom face, which was converted to the equivalent hydrostatic pressure of 2.446×10^6 pascal (Pa). Three wells were placed inside the model domain to represent the injection well (Wel-01), the monitoring well (Wel-02), and the pumping well (Wel-03). The well screens were 20 m long and located from $z = -10$ m to $z = 10$ m. Table 1 provides more information on the three examples.

dfnWorks was used to generate fracture networks, and then simulate steady-state pressure. The codes developed in this study were used to simulate hydraulic heads and perform particle tracking to a pumping well. The results were analyzed with respect to simulated hydraulic heads, water balance, particle pathlines, and simulated breakthrough curves.

Table 1. Parameters used for three hypothetical examples.

Parameters	**Example 1**	**Example 2**	**Example 3**
Model domain size (m)	100 × 100 × 100	500 × 500 × 100	250 × 250 × 100
Fracture characteristics	4 deterministic rectangular fractures	4 deterministic rectangular fractures	Randomly distributed elliptical fractures
Fracture density P_{32} (m^2/m^3)	0.040	0.032	0.35
Number of wells	2	2	3
Well screen interval (m)	10	10	20
Well skin radius (m)	2	2	1 and 5
Well permeability (m^2)	10^{-7}	10^{-7}	10^{-7}
Constant fracture aperture (m)	200×10^{-6}	200×10^{-6}	200×10^{-6}
Constant fracture permeability* (m^2)	3.33×10^{-9}	3.33×10^{-9}	3.33×10^{-9}
Number of initial particles	90,000	90,000	100,000
Pumping rate (m^3/s)	10^{-4}	10^{-4}	10^{-3} and 10^{-4}
Water column at bottom boundaries (m)	250	250	250
Hydrostatic pressure at bottom boundaries $z = -50$ m (Pa)	2.5×10^6	2.5×10^6	2.5×10^6

*Fracture permeability is calculated from fracture aperture using the cubic law (Klimczak *et al.*, 2010).

Figure 6a shows the DFN in Example 1 and the locations of the two wells. This figure also illustrates the simulated steady-state hydraulic head converted from the pressure solution by PFLOTRAN. Figure 6b shows the high-resolution mesh around the pumping well and highlights (in red) the cells used to represent the actual well screen. The 121 red cells represent the well screen, with the small cell sizes near the well center and the coarser cell sizes farther away. The total volumetric flow from 121 pumping cells was 8.64 m^3/day (0.1 L/sec). Inflows were from four sides of the model domain. The inflow from the north was equal to the inflow from the south (1.82 m^3/d). The largest inflow (4.43 m^3/d) was from the east, whereas the smallest inflow (0.57 m^3/d) was from west.

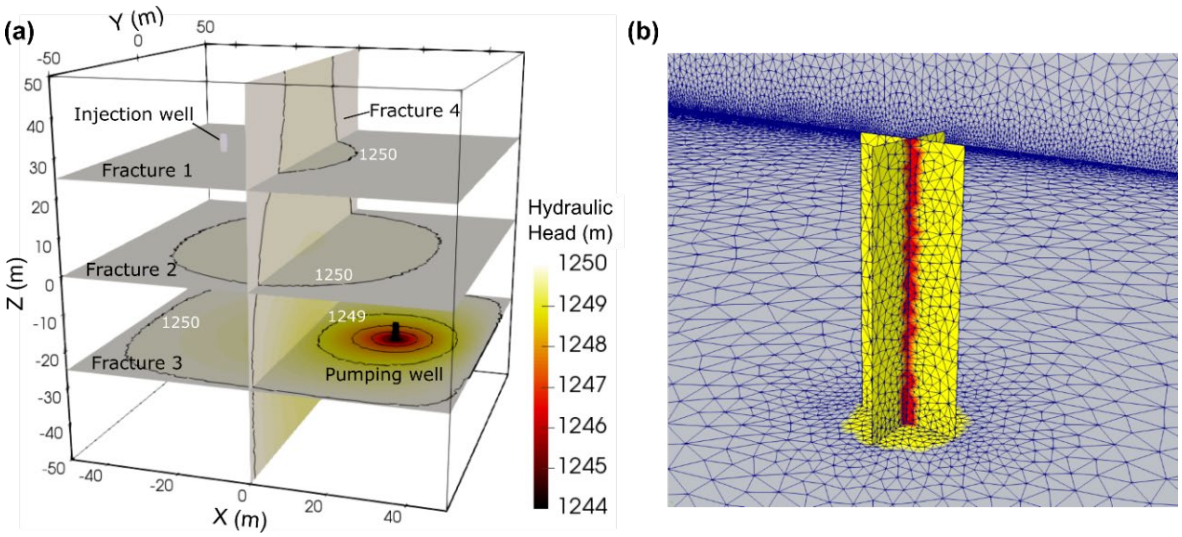

Figure 6. The configuration of Example 1 showing (a) a DFN network with wells and simulated hydraulic head solution, and (b) a closer look at the pumping well with Delaunay triangulations. Red cells mark the pumping well screen and yellow cells represent the highly conductive area around the well.

Figure 7a shows the particle pathlines for Example 1, in which 90,000 particles were instantaneously and uniformly released on three edges of each fracture at the west side of the model domain (30,000 particles on each left edge of fractures 1 to 3). Figure 7b shows the BTCs. All 90,000 particles were captured by the pumping well, resulting in a 100 percent recovery rate. The earliest and latest particle arrival times were 25.6 (hours) and 2,056.8 (hours), respectively. The BTCs revealed three peaks owing to the release of particles from three different distances from the pumping well. The recovery rate was lower for the case in which the particles were released from the injection well (Figure 7c). Only 85,686 particles (95.21 percent) were captured at the pumping well in this scenario. Figure 7d shows the BTC with only one peak because all particles were initially released at the same location.

Based on Examples 1 and 2, four experiments were designed to evaluate the influences of well skin permeability and radius on simulated BTCs at a pumping well. Given the fixed number of intersections between a well and the fracture backbones (which equals one in these examples), the two parameters control: (1) how quickly particles move into fracture backbones after they are released at an injection well and (2) how quickly particles are removed by a pumping well. Therefore, the two parameters will potentially affect the simulated BTC at a pumping well depending on: (1) how large the well skin radius is compared with the distance between an injection well and a pumping well, and (2) the flow dynamics around the injection well and the pumping well (i.e., a high flow velocity value around and along a well may make the BTCs less sensitive to these two parameters). In addition, the two parameters can affect the convergence of flow simulation.

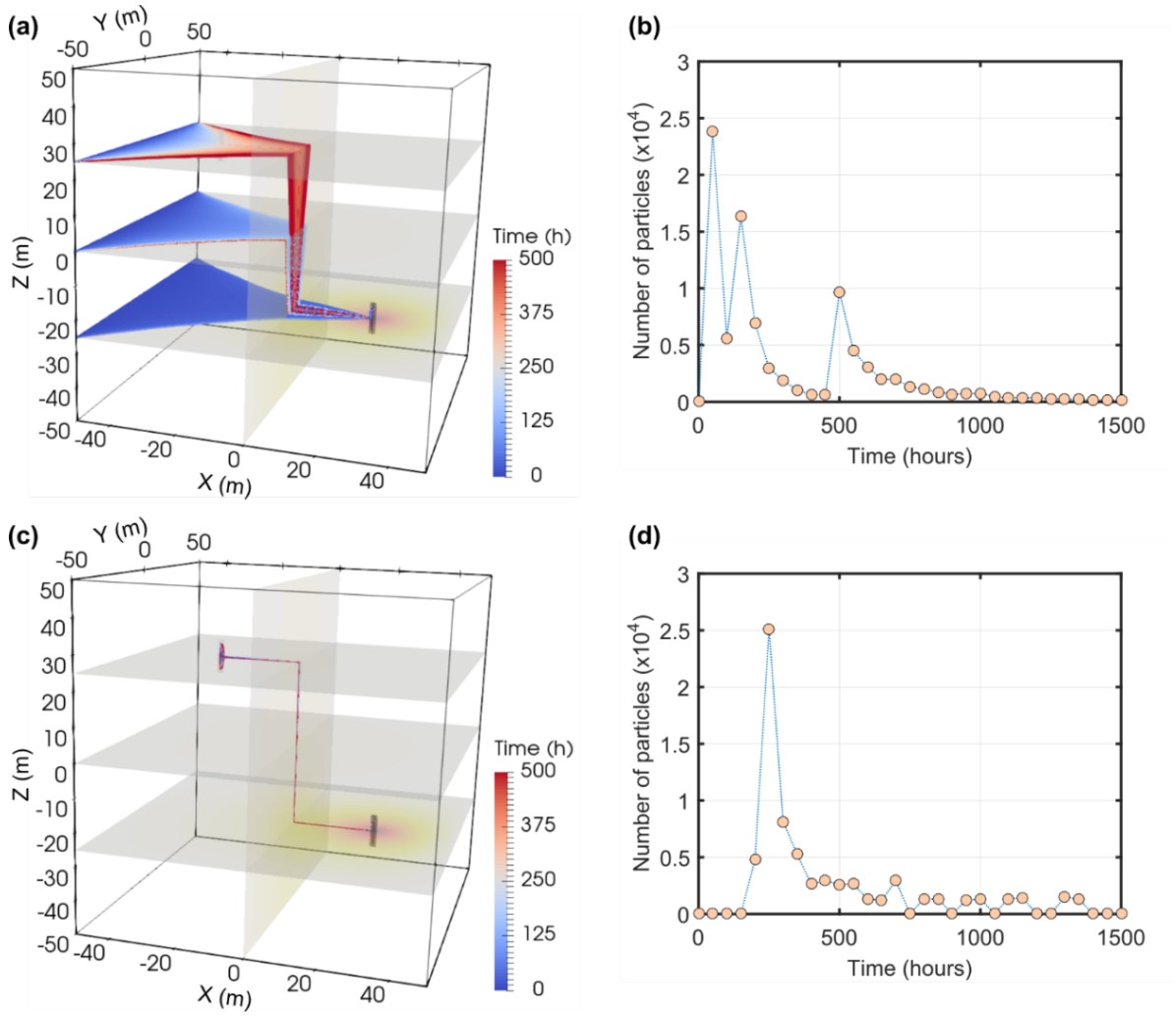

Figure 7. Particle pathlines and BTCs for Example 1 that show particles uniformly distributed over the west side of the model domain ([a] and [b]) and particles uniformly distributed at the injection well ([c] and [d]).

Table 2 shows detailed parameters for four numerical experiments. In these experiments, the permeability of both the injection well and the pumping well varied over a range of 10^{-7} m^2 to 10^{-10} m^2 at intervals of one order of magnitude. The well skin radius varied from 1 m to 5 m at 1 m intervals. All experiments were conducted for the 100 m DFN model domain in Example 1 and the 500 m DFN model domain in Example 2. The experiments focused on cases in which particles were released at an injection well.

Table 2. Configurations of Examples 1 and 2 to evaluate the influences of well skin radius and permeability on simulated BTCs at a pumping well. Particles are released at an injection well.

Experiment	Skin Permeability (m^2)		Skin Radius (m)	
	Injection Well	Pumping Well	Injection Well	Pumping Well
1	10^{-7} to 10^{-10}	10^{-7}	2.0	2.0
2	10^{-7}	10^{-7} to 10^{-10}	2.0	2.0
3	10^{-7}	10^{-7}	1.0 to 5.0	2.0
4	10^{-7}	10^{-7}	2.0	1.0 to 5.0

Experiment 1 evaluated the effects of injection well skin permeabilities on simulated BTCs at the pumping well for both the 100 m and 500 m DFN model domains. Figure 8a shows that BTC of conservative particles at the pumping well gets delayed (i.e., transport time is longer) as the well skin permeability of the injection well reduces. The 500 m DFN model domain showed similar results (Figure 8b). In the second experiment, varying the pumping well skin permeabilities showed no effect on the simulated BTCs. Therefore, transport is sensitive to injection well permeability but not as sensitive to pumping well permeability. This was likely caused by the short range (less variability) of travel times in the vicinity of a pumping well (owing to the steep hydraulic gradient induced by the pumping), whereas the travel times were wide ranging in the vicinity of an injection well.

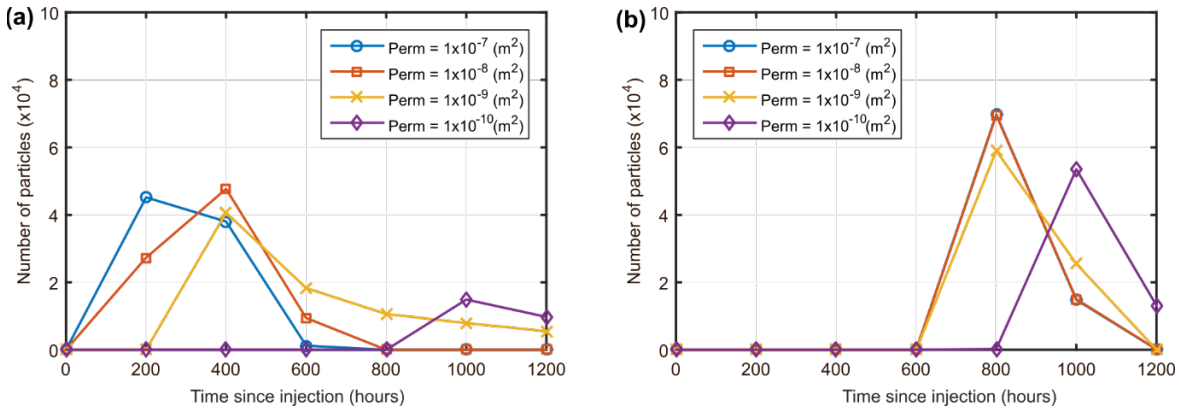

Figure 8. Simulated BTCs using four different values of injection well skin permeability for: (a) Example 1, the 100 m DFN model; and (b) Example 2, the 500 m DFN model.

Experiment 3 examined the effects of injection well skin radii on simulated BTCs at the pumping well. The skin radius here is conceptualized as a calibrated parameter as it cannot be measured directly. The results showed that injection well skin radii had significant effects on simulated BTCs at the pumping well for the 100 m DFN model, as shown in Figure 9a. Reducing the injection well skin radii from 5 m to 1 m significantly decreased the peaks of the simulated BTCs. For the 500 m DFN model, the BTCs had similar trends when using injection well skin radii of 3 m, 4 m, and 5 m, as shown in Figure 9b. Using smaller values such as 1 m and 2 m resulted in different BTCs, potentially because of numerical issues. The results revealed that injection well radii had a significant impact on simulated BTCs and that the impact was less in a large model domain. In the fourth experiment, pumping well skin radii showed no effects on the simulated BTCs.

For the BULLION FGE case study (Example 3), four stochastic DFNs were generated at two pumping rates (10^{-4} m^3/s and 10^{-3} m^3/s) and two well skin radius values (1 m and 5 m). This created 16 model scenarios. Using a 5 m well skin radius, the results showed that only one of the four stochastic DFNs had all three wells intersecting one or more fractures. For this DFN, the number of fractures that intersected Wel-01, Wel-02, and Wel-03 were 2, 4, and 3, respectively. Figures 10a and 10b show the simulated hydraulic heads and particle tracks for this DFN using the low pumping rate of 10^{-4} m^3/s. The results showed noncircular contours of simulated hydraulic heads around the pumping well exhibiting drawdown characteristics for this DFN.

Particles were distributed uniformly along the vertical profile of the injection well (Wel-01) (Figure 10). Particles moved out of Wel-01 into the hydraulic backbone through a single preferential pathway. Most of the particles then migrated through Wel-02 (since Wel-02 was collinear with Well-01 and Wel-03 and was assigned a higher permeability than the surrounding fractures), and underwent enhanced spreading because of the higher number of intersections between Wel-02 and the backbone (Figures 10a and 10b). Finally, the particles exited the computational domain via the pumping well, Wel-03.

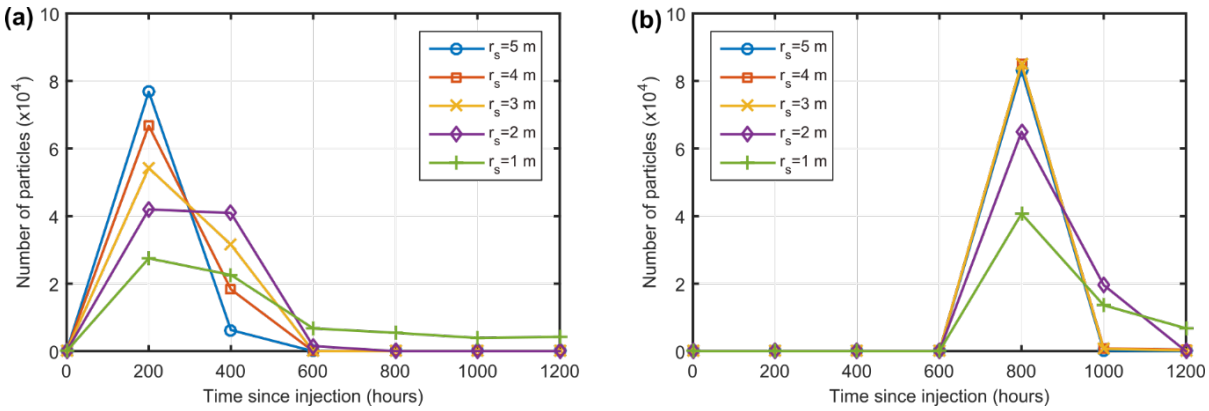

Figure 9. Simulated BTCs using five different values of injection well skin radii for: (a) Example 1, the 100 m DFN model domain; and (b) Example 2, the 500 m DFN model domain.

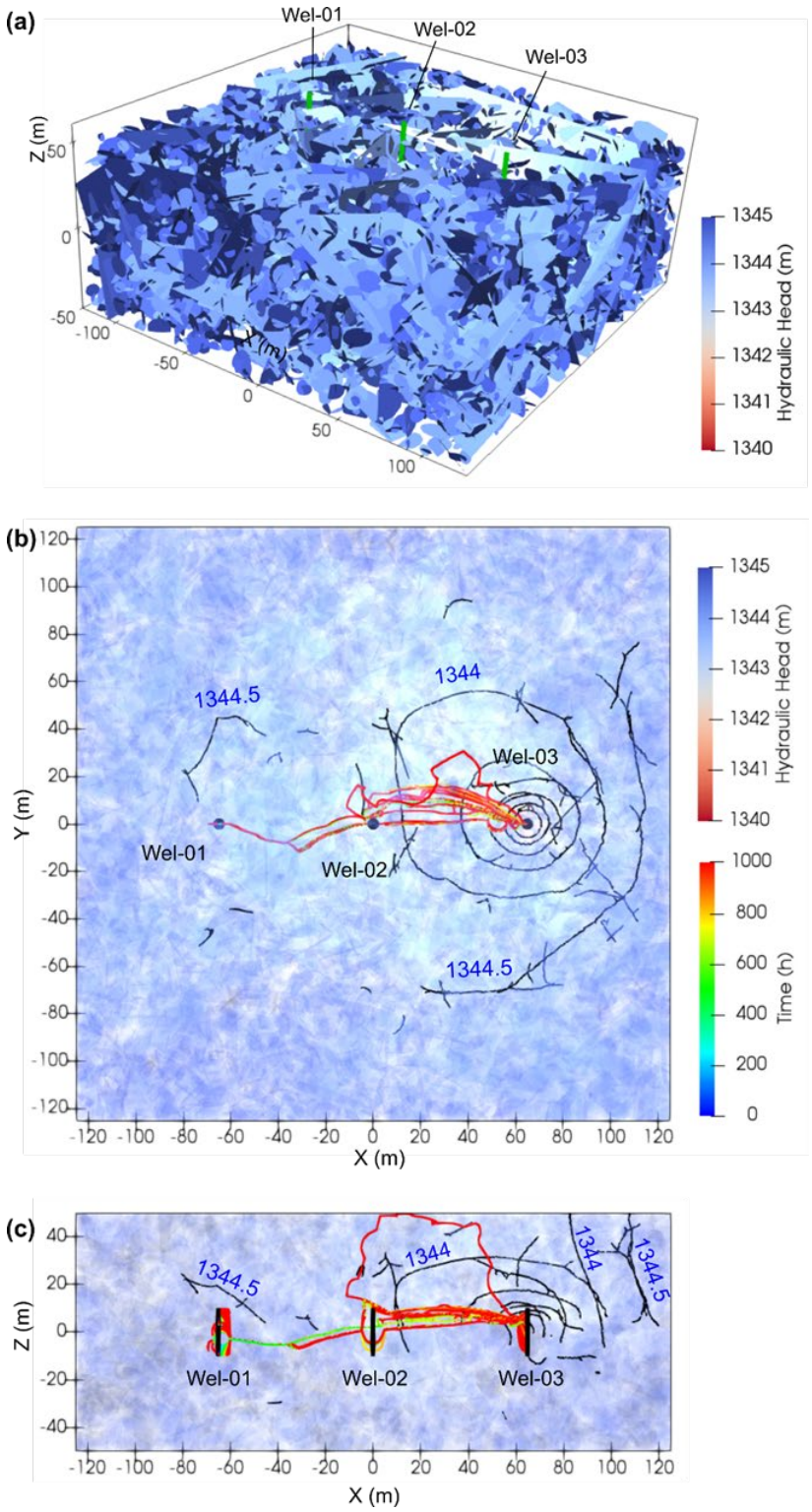

Figure 10. Simulated steady-state hydraulic heads and particle pathlines for the 3-D DFN of Example 3: (a) 3-D perspective of the hydraulic head distribution, (b) a top view, and (c) a ZX cross-sectional view. Background colors illustrate the simulated hydraulic heads. Black lines are hydraulic head contours and colored lines depict particle tracks (color coded according to travel time).

The models failed to converge when using the high pumping rate of 10^{-3} m^3/s. The convergence issues are likely related to the steep hydraulic gradients which are not properly resolved by the iterative solvers in the vicinity of a pumping well. Use of a 1 m well skin radius resulted in zero intersections between one or more wells and the hydraulic backbone.

Discussion of the Method

The method used in this study provided a way to integrate a well into a DFN model and ensure that the well was connected to the hydraulic backbone. Two orthogonal fractures were used to represent a well. Two new parameters, the well skin radius (r_s) and the well skin permeability (k_s), establish the connection between a well and the fracture network. This method is different from available DFN modeling codes such as HydroGeoSphere (Brunner and Simmons, 2012), in which a well is represented by a one-dimensional line, or FracMan (Dershowitz *et al.*, 1993), in which a well is represented by model cells at the well location. The method presented in this section defines a physical screen interval and includes an injection/pumping well in a DFN via a discretized model grid. High-resolution mesh at a well improved the accuracy of flow and transport simulations. The meshes allowed for the smooth transition of pressure and particles from one fracture to another, from a well to the backbones, and from the backbones to a well. The method was implemented in dfnWorks and verified against the widely used MODFLOW and MODPATH codes. Modifications were made that allowed hydraulic heads to be simulated and particles to be tracked to a pumping well. A user needs to overwrite three source code files and recompile dfnWorks to use this method.

Injection well skin radii and permeability affect the simulated BTCs when particles are released at an injection well. These effects lessen when applying the method to a larger domain DFN. In contrast, pumping well skin radii and permeability have a negligible effect on simulated BTCs. This is because the time taken by a particle to travel in the skin zone of a pumping well is extremely small compared with the overall ranges of transport time. Particles experience higher velocity in the pumping well skin zones, and therefore quickly exit the model after coming in close proximity to a pumping well. However, the pumping well skin radius has a more important role than well skin permeability. The radius could be increased to enhance connectivity between a pumping well and the hydraulic backbone, and improve numerical stability when conducting flow simulations.

Pumping rates also influence the convergence of the flow solution. At higher pumping rates, the hydraulic gradient in the vicinity of a pumping well can increase to unrealistic values causing nonconvergence of the flow solution. To overcome this problem, the pumping well skin radius can be increased to enhance connectivity and numerical performance of the DFN model.

Well skin radii play an important role in defining the connectivity between a well and fractures in complex and realistic networks (as shown in the BULLION FGE example). Using radii that are too small may result in no connection, but using radii that are too large may overestimate the connectivity. Well skin radii are case-specific parameters and depend on fracture density, orientation, and length. Ideally, the well skin radius should be determined by computing and comparing fracture intensity, P_{10}, along the vertical profile of a well (by varying the well skin radius until a good match is found between simulated and observed P_{10}).

UPSCALING OF TRANSPORT IN 2-D DFNs VIA RANDOM WALK MODELS

Flow and transport in fractured rock are often characterized by a wide range of velocities. The velocity of solute within the fracture network can be several orders of magnitude higher than the velocity of solute within the surrounding rock matrix (Berkowitz, 2002; Neuman, 2005). This makes numerical solution of the transport behavior computationally intensive because high gradients require fine grids. Therefore, to model flow and transport in fractured rock, it is often desirable to upscale using some type of averaging procedure so that the fine details of the flow are accounted for in an effective way, rather than explicitly resolved. This can be done by establishing effective hydraulic conductivity tensors that account for both the fractures and the matrix (Klimczak *et al.*, 2010; Liu *et al.*, 2016; Margolin *et al.*, 1998; Oda, 1985). For transport, however, this type of approach is insufficient. Using effective hydraulic conductivity in transport models leads to the use of an advection dispersion equation, which assumes that transport is Fickian. Variations in small-scale velocity lead to enhanced solute spreading (as defined by the change in the variance of the solute plume), which scales faster than linear in time until it asymptotes to linear spreading. If the region of the domain over which the effective hydraulic conductivity is defined is large enough for this asymptotic behavior to occur, then this approach is valid (Klimczak *et al.*, 2010). However, the higher the variation in velocity, the larger the region must be for the transport within it to become Fickian.

An alternative approach is to model transport only within the high-velocity regions of the flow. In fractured rock, this is done using DFN models, which assume no flow within the rock matrix (Hyman *et al.*, 2015; Painter and Cvetkovic, 2005; Parashar and Reeves, 2012). This approach gives a more accurate description of transport within the fractures, but it is restricted to small-scale use because of computational expense. Therefore, there is clearly a need for upscaling models that accurately extrapolate transport behavior from small-scale DFNs to larger scales.

Many models, both Lagrangian and Eulerian, have been created for and applied to upscaled transport modeling in DFNs. This section focuses specifically on Lagrangian random walk models, which use particle trajectories from the DFN simulations to create empirical space and time step distributions that are sampled from in the random walk simulations. In a broad sense, these models can all be categorized as continuous time random walk (CTRW) models (Berkowitz *et al.*, 2005; Berkowitz and Scher, 1997, 1998). However, the models have different definitions of what constitutes a step and have different ways of modeling correlations between steps. The three models discussed are the Markov-directed random walk (MDRW) (Painter and Cvetkovic, 2005), Monte Carlo solution of the Boltzmann transport equation (BTE) (Benke and Painter, 2003), and the Spatial Markov model (SMM) (Le Borgne *et al.*, 2008). Each model successfully reproduced the results of full resolution transport simulations in DFNs (Benke and Painter, 2003; Kang *et al.*, 2011, Painter and Cvetkovic, 2005). This section presents a side-by-side comparison of the predictive capability of these models in both correlated and uncorrelated forms. The correlated forms of all models use a Markov chain. A set of realizations of random 2-D DFNs for three different fracture transmissivity distributions were used to compare the models. As the variance of the transmissivity distribution increased, the range of velocities

within the DFN widened while the number of high flux fractures decreased (Reeves *et al.*, 2013). This had a profound effect on the predictive capability of the upscaled models, particularly with regard to comparing correlated and uncorrelated models.

The ability of the upscaled models to predict transport in real fractured rock is dependent on both the accuracy of the DFN simulations and on how well the upscaled models match the DFN simulations. The scope of the work presented in this section is limited to the latter. The transport results of the DFN simulations were taken to be the truth, and the upscaled models were developed to capture features of DFN results. Although the upscaled models were analyzed based on their ability to match DFN simulations, this approach could be used to assess their predictive capabilities, assuming the accuracy of the DFN simulations.

The "DFN Simulation Setup" section describes the DFN simulations, including the effect of widening the distribution of fracture transmissivity and what information was collected to parameterize the upscaled models. The "Upscaled Modeling" section describes the upscaled modeling. The "Results" section following the "Upscaled Modeling" section discusses both the correlated and uncorrelated versions of the models, with varying modeling scales. Finally, the "Discussion of Methods" section following the "Effect of Changing Modeling Scale" section covers the relevance of the results.

DFN Simulation Setup

The DFN simulations formed the basis of both testing and parametrizing the set of upscaled transport models. Large-scale DFN simulations were conducted, generating detailed transport behavior that the upscaled models were expected to predict. Another set of transport simulations was done on a smaller region of the DFN in which particle trajectories were analyzed to create empirical space and time step distributions, which were then used to develop predictions of the large-scale DFN transport using each upscaled random walk model. All fracture networks were generated and flow was solved using DRI's in-house DFN generator, solver, and transport simulator (Parashar and Reeves, 2012).

The first step was to create the large-scale fracture network itself. Discreet fracture networks were stochastically generated through the incremental addition of fractures with statistically defined random locations, lengths, and orientations until a specified density criterion was reached (Parashar and Reeves, 2012). Fracture network density was defined as the total length of all fractures normalized by the domain area. Once the fracture network was generated, the network was split into segments, which were defined as the part of a fracture between two fracture intersections (Berkowitz and Scher, 1997, 1998). Isolated fractures and dead-end segments were identified and deleted because they were not hydraulically connected to the boundaries, and therefore could not convey any flow. Several analyses of field data determined that fracture trace length often followed a power-law distribution (Bonnet *et al.*, 2001; Davy, 1993; Odling, 1997; Renshaw, 1999). The assumption that the DFN was scale free supports the use of power law distributions for fracture trace length. Studies indicated that the values of the power law's exponent, α, typically ranged between 1 and 3 for natural rock fracture networks (Bonnet *et al.*, 2001; Davy, 1993; Renshaw, 1999). Fracture angles were drawn from a von Mises distribution, which is analogous to a normal distribution on a circle. The fracture density was fixed at 1/2 m/m^2 and the domain size was fixed at 1,000 m × 200 m. Figure 11 shows a realization of the DFN before the isolated segments were removed. The only fracture characteristic parameter that was varied between

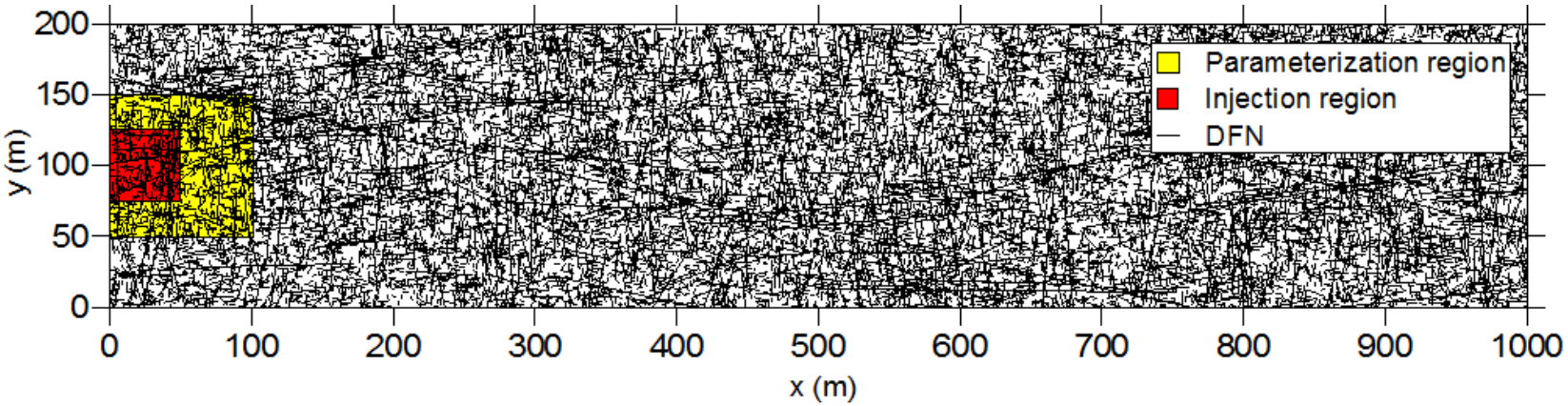

Figure 11. Modeling domain: one realization of a DFN with injection region highlighted in red and parameterization region highlighted in yellow.

DFNs was the standard deviation, σ, of the transmissivity distribution. When $\sigma = 0$, the transmissivity of all fractures were the same, but as σ increased, the range of fracture transmissivity increased.

Particle jump length in a fracture network was guided by the distribution of the length of fracture segments created because of the intersections between individual fractures of the network. It also depended on the connectivity of the network, because a poorly connected network precludes migrating particles from sampling the entire set of segment lengths available during transport across the model domain. Individual fractures that form the components of a network intersect each other to generate a large number of smaller fracture segments through which migrating inert particles travel linearly between two successive intersection points.

The next step was to solve for the flow through the network. This was done by imposing CHB conditions such that the global hydraulic head gradient was $\partial h/\partial x = -0.1$ and $\partial h/\partial y = 0$, and therefore the dominant flow direction was from left to right. The steady state head distribution was then solved, and defined at each fracture intersection according to:

$$\nabla^2 h = 0 \tag{3}$$

This assumes that the fracture network is fully saturated with incompressible fluid. From the head distribution, we defined the flux of fluid through each fracture segment according to Darcy's law:

$$q = -\frac{T}{b}\nabla h \tag{4}$$

where T is the fracture transmissivity and b is the fracture aperture. The fracture aperture is related to the transmissivity by way of the cubic law:

$$T = \frac{b^3 \rho g}{12\mu} \tag{5}$$

where ρ and μ are the density and dynamic viscosity of the fluid (water) and g is gravitational acceleration (Klimczak *et al.*, 2010; Witherspoon *et al.*, 1980). In combination, these laws assume a low Reynolds number of flow through a fracture segment with a constant aperture (envisioned as the fracture being bounded by parallel plates).

Finally, the transport through the DFNs was simulated. A random walk method was used in which the solute mass was discretized into particles of equal mass initially distributed over a 50 m × 50 m region along the upstream boundary (shown in Figure 11). The number of particles injected into each fracture segment was proportional to its flux (q). Each particle then proceeded through the segment at constant velocity:

$$\mathbf{v} = q\hat{\mathbf{u}} \tag{6}$$

where û is the unit vector parallel to the fracture segment. Once the particle reached the end of the fracture segment, it moved into a new segment (s_i) with a probability proportional to its flux (q_i). That is:

$$P(S_i) = \frac{q_i}{\sum_{i=1}^{n_{seg}} q_i} \tag{7}$$

where n_{seg} is the number of segments connected to the current segment. This treatment assumed that dispersion along the fracture length was negligible and that the concentration of solute across the fracture width was uniform. In other words, because of the fracture's low aspect ratio, the velocity distribution within the fracture was assumed to be sampled relatively quickly by the solute compared with the amount of time it spent in the fracture. Once the particle reached the boundary of the DFN, it was removed from the system (i.e., all boundaries were absorbing). Each simulation was run until all particles were removed. This random walk method is distinct from the upscaled models discussed in the next section, because the particles have access to the full details of the DFN and all segment selections depend on the spatial location of the particles and the flux of the connecting segments.

In addition to simulating transport over the entire DFN, a small 100 m × 100 m region along the upstream boundary was delineated to run another transport simulation. The particle trajectories obtained over this smaller region were then analyzed and used to create space and time step distributions for the set of upscaled models described in the "Upscaled Modeling" section. This region of the domain is referred as the "parameterization" region. To ensure that there were a large number of trajectories to analyze, 10^5 particles were used for the full DFN transport simulations and 10^6 particles were used for the parameterization simulations. For visualization purposes, Figure 11 shows the modeling domain and how it is partitioned into different regions.

Effect of Transmissivity Distribution on DFN Simulations

Equation 4 shows that an increase in the range of fracture fluxes occurs as the range of transmissivity increases (flux is proportional to transmissivity). The range of transmissivity is controlled by the standard deviation of the transmissivity distribution (σ). Figure 12 shows the probability density function (PDF) of the absolute value of fracture fluxes ($f_{|q|}(x = |q|)$ in m/s), where q_i is the measured flux through segment i, obtained from all segments in fifty realizations of transmissivity distributions with σ = 0, 0.5, and 1. The PDFs are bimodal (high probability associated with two ranges of velocities), with peak values generally decreasing as σ increases, which spreads the PDF out toward high flux fractures. This nonmonotonicity is a property that each of the upscaled models must be capable of simulating.

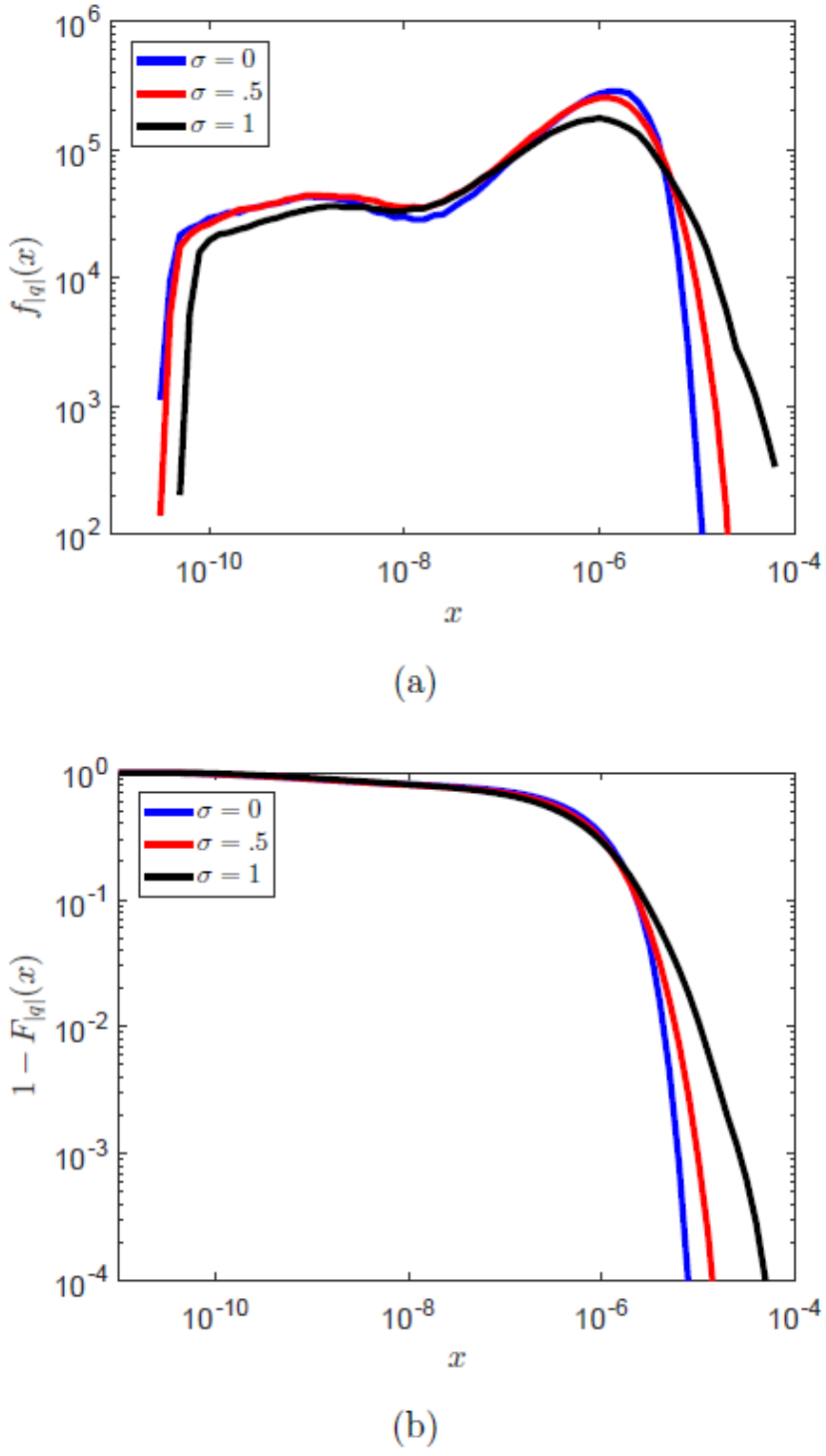

Figure 12. Fracture flux magnitude for various values of the standard deviation of the transmissivity distribution (σ): (a) PDF ($f_{|q|}(x)$) and (b) complementary cumulative density function (CCDF) ((1-$F_{|q|}(x)$).

However, the effect of the transmissivity distribution on the presence of connected high-velocity flow channels, or preferential pathways, is more difficult to capture in upscaled models. Figure 13 shows $\log_{10}(|q|)$ for one realization of a DFN for each transmissivity distribution (σ = 0, 0.5, and 1), in which all fracture properties are identical with the exception of transmissivity distribution. As σ increases, there are fewer high-velocity fractures but they are highly connected, so more preferential pathways form. This causes the fast-moving solute within the water to continue to move fast for long distances and times, which means the solute's velocity at a given time or location is not independent of its prior velocity history. This correlation between velocities persists for long times and distances.

In Figure 12 and in the remainder of this section, all results were derived from fifty realizations of the DFN for each value of σ. The number of realizations generated was chosen by comparing moments of breakthrough curves from each realization to moments of the ensemble breakthrough curve at the farthest distance from the inlet (1 km) and ensuring that the relative mean absolute deviation between moments were sufficiently minimized.

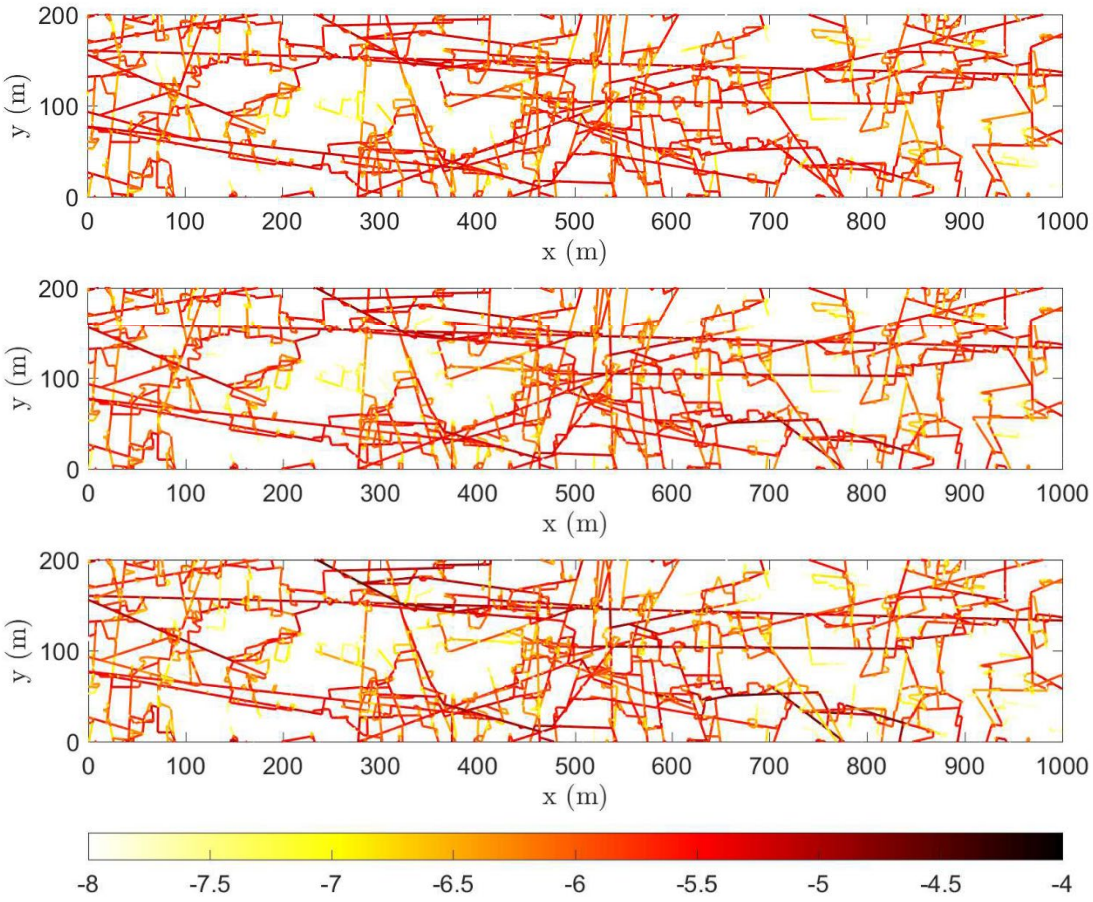

Figure 13. Flux magnitude ($\log_{10}(|q|)$) distribution for one realization of each transmissivity distribution of the DFN (top) σ = 0, (center) σ = 0.5, and (bottom) σ = 1. To better highlight the differences in the high-velocity fractures, we set the color scale so that all fractures with $|q| < 10^{-8}$ m/s are not seen. Numerical values on the color bar represents logarithm of the flux magnitude.

Upscaled Modeling

Following the extraction of the trajectory data from the small DFN simulations (done over the parameterization region), the numerical data was used to create distributions for the three upscaled random walk models. The goal was to use these models to predict the breakthrough at locations outside of the parameterization region. Although the upscaled models can be assessed by their ability to match the full-scale DFN simulations, they do not have access to the statistics of the full DFN, so their results are referred to as predictions. This section briefly introduces each of the upscaled random walk models used to predict transport in the DFNs.

Each of the models can be categorized as a CTRW (Berkowitz *et al.*, 2006). In CTRWs, the solute is discretized into particles of equal mass that take steps in space and time, sampled from a density $f(\delta x, \delta y, \delta t)$, in which δx, δy, and δt may or may not be coupled. For fracture networks, usually a step is considered to be the spatial and temporal jump a particle would make through a single fracture segment. To see the effect of modeling scale on the accuracy predictions, however, a variety of step definitions are considered. Once the concept of what constitutes a step is defined, particles are injected into the domain, and then each particle transitions through space and time according to:

$$\begin{aligned} x_n &= x_{n-1} + \delta x_n \\ y_n &= y_{n-1} + \delta y_n \\ t_n &= t_{n-1} + \delta t_n, \qquad n = 1, 2, 3, \ldots \end{aligned} \tag{8}$$

where the random triplet $(\delta x_n, \delta y_n, \delta t_n)$ comes from $f(\delta x, \delta y, \delta t)$ and may or may not depend on $(\delta x_{n-1}, \delta y_{n-1}, \delta t_{n-1})$. There is no requirement that δx, δy or δt be decoupled or fixed. Most often, $f(\delta x, \delta y, \delta t)$ is a parameterized probability density, which allows for analytical solution of concentration distributions in space and time if the space and time steps are uncoupled (Cortis *et al.*, 2005). Although it is less convenient, the theory allows for more general empirical densities, including coupled space and time steps. The key creating any CTRW model is the parameterization of $f(\delta x, \delta y, \delta t)$, which is assumed to be independent of particle position (i.e., statistically stationary in space).

Generally, steps are assumed to be independent and identically distributed, but this study considered both correlated and uncorrelated steps. This distinction may affect model predictions depending on how much correlation exists between successive steps in the DFN simulations (Bolster *et al.*, 2014; Sund *et al.*, 2015), which in turn depends on the structure of the DFN. In all three of the upscaled random walk models described in this section, each step a particle makes in space and time depends on its previous step. This correlation between steps was accounted for using a Markov chain. The CTRW models, without the added complexity of a Markov chain, have been used successfully in past studies to describe transport through fracture networks (Berkowitz and Scher, 1997, 1998). Further information on the CTRW is available in Berkowitz *et al.* (2006).

For each realization of all of the upscaled models, we injected 10^5 particles. The initial distribution of these particles matches the initial condition in the DFN simulations because they were initially distributed over a 50 m × 50 m region along the upstream boundary, where the number of particles that start at each location was weighted by fracture

segment flux. The absorbing boundary conditions were used to match those in the DFN simulations, meaning that particles that moved outside of the domain were removed from the simulation. Each simulation was run until all particles were removed from the domain.

Markov-directed Random Walk (MDRW)

The MDRW model was introduced in Painter and Cvetkovic (2005). In addition to modeling correlation between steps with a Markov chain, the model also provided further flexibility to explicitly model retention, a feature that was not required in this study because our DFN simulations did not model retention. The steps (δx_n, δy_n, δt_n) were defined to correspond to transport through a fixed number of fracture segments, k. This was done by splitting every trajectory from our parameterization simulations into groups of k segments and recording the distance and travel time from the beginning of the first segment in each group to the end of the kth segment in each group. Therefore, from each trajectory, depending on the number of segments it goes through, multiple samples were extracted that could be used to construct $f(\delta x_n, \delta y_n, \delta t_n)$. Figure 14 shows the full path of an individual particle and how it was partitioned into steps.

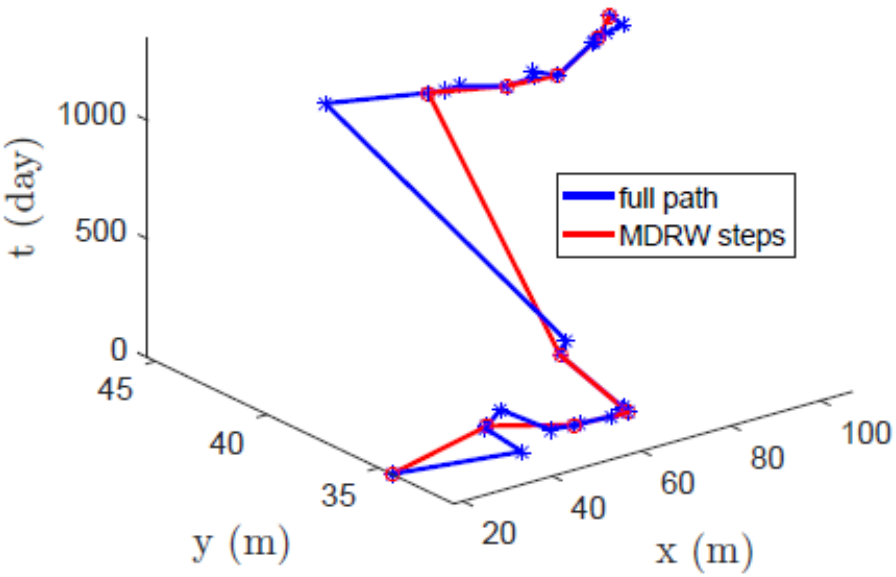

Figure 14. Method for partitioning particle trajectories into MDRW modeling steps.

To account for correlation between steps, a set of 20 discrete equiprobable states based on speed was first defined. Each state was defined by a range of speed, which for state s_i is from l_{i-1} to l_i, where $l_0 \equiv 0$. A particle was in state s_i at step n if its speed:

$$q_n = \frac{\sqrt{\delta x_n^2 + \delta y_n^2}}{\delta t_n} \tag{9}$$

was within the range of l_{i-1} to l_i. This means that low numbered states covered low speeds and high numbered states covered high speeds.

Given this definition, a Markov chain could be created that consisted of the initial (now discretized) distribution and a transition matrix using the trajectories from the DFN simulations. The transition matrix was the conditional probability that the speed at step n was in state s_i given that the speed at step $n-1$ was in state s_j, $P(q_n \in s_i | q_{n-1} \in s_j)$. Figure 15 shows the transition matrix, $P(q_n \in s_i | q_{n-1} \in s_j)$, averaged over all fifty realizations for each transmissivity distribution, using $k = 1$ fracture segment as the modeling step. All of the transition matrices were diagonally dominant, indicating a tendency for particles to remain in their current speed state. As the spread of the transmissivity distribution increased with σ, the probability of particles transitioning many states in one step decreased, which can be seen in the slendering of the bands around the diagonal. This indicates that particle speed does, in fact, increase with increasing σ. An MDRW model that uses only one speed state would have uncorrelated steps, so MDRW can easily be run in both correlated and uncorrelated forms. This is all the information necessary to run the MDRW simulations. Each particle transitions through space and time according to Equation 8, with:

$$f_{MDRW}(\delta x, \delta y, \delta t) = f(\delta x_n, \delta y_n, \delta t_n | q_n \in s_i)$$
$$P(q_n \in s_i | q_{n-1} \in s_j) \tag{10}$$

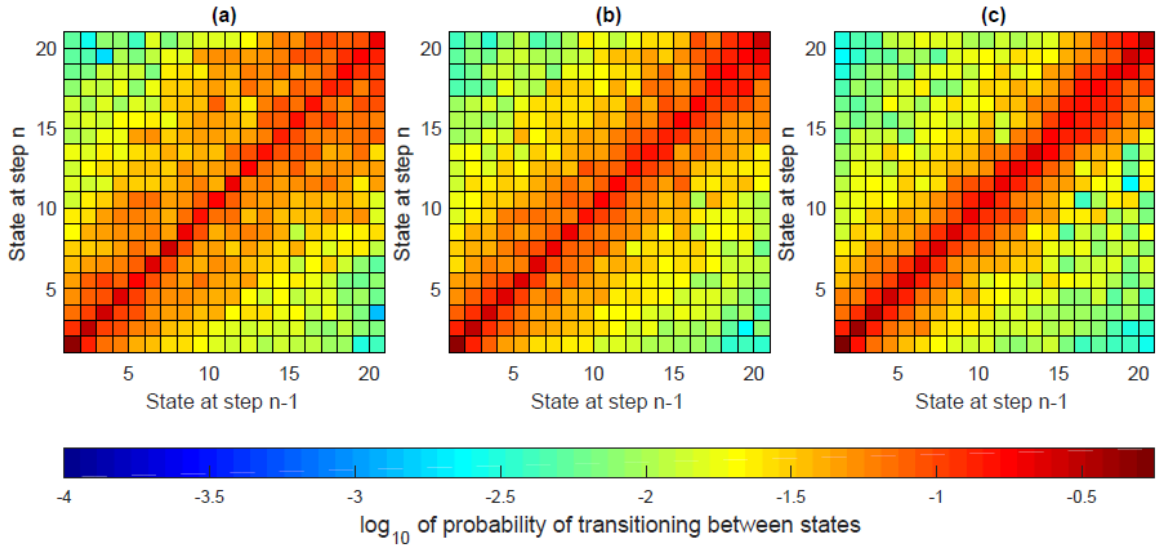

Figure 15. Ensemble averaged transition matrix ($P(q_n \in s_i | q_{n-1} \in s_j)$) over all realizations with modeling step size $k = 1$ fracture segments for transmissivity distributions with (a) $\sigma = 0$, (b) $\sigma = 0.5$, and (c) $\sigma = 1$.

Monte Carlo Solution of the Boltzmann Transport Equation (BTE)

The BTE model was introduced in Benke and Painter (2003). It models the correlation between steps with a Markov chain based on velocity (both speed and direction). It defines steps (δx_n, δy_n, δt_n) to correspond to transport through a fixed number of fracture

segments, k, so DFN particle trajectories are split in the same way as with the MDRW. Contrary to the MDRW methodology, the length of a particle's step as it travels at the velocity sampled from the DFN trajectories is also random (albeit dependent on velocity state), rather than the step being the same length as the corresponding trajectory segment. To do this, spatial steps are put in polar form:

$$\begin{aligned} \delta x_n &= d_n \cos\theta_n \\ \delta y_n &= d_n \sin\theta_n \end{aligned} \tag{11}$$

where d_n is log uniformly distributed between limits that depend on the velocity class and θ_n is the angle of the randomly chosen trajectory. To account for correlation between steps, and to define the distribution of d_n, a set of 10 discrete equiprobable states based on speed was first defined. Similar to MDRW, each state was defined by a range of speed, which for state s_p is l_{p-1} to l_p, where $l_0 \equiv 0$. Then, the average jump length of trajectory segments corresponding to each state was found, which for state s_p is r_p. The distance a particle travels at its current velocity, d_n is then generated as:

$$d_n = -\ln(U) r_p \tag{12}$$

where U is a uniform random number between 0 and 1. Therefore, in theory, a particle may continue at its current velocity until it travels a distance between 0 and ∞ times the length of the trajectory segment.

Next, the distribution of speed states was further discretized by angle to create velocity states. For our purposes, each speed state was split into two equiprobable angle bins (for a total of 10 speed × 2 angle = 20 velocity states) because the BTE needed to have the same number of states as the MDRW. The full range of possible angles was $[-\pi, \pi]$, with an angle of 0 aligned with the predominant flow direction. Because only two angle states for each speed bin were used, the angles were divided into "upstream" and "downstream," meaning that the absolute value of the step angle was used to set angle bin limits. A particle was in velocity state $s_i = 2(p-1) + q$ if its speed was in state s_p and the absolute value of its angle was between angle limits $l_{p,q-1}$ to $l_{p,q}$, where $l_{p,0} \equiv 0$, which were defined separately for each speed state, p. Given this definition, the transition matrix was then approximated, which was the conditional probability $P((q_n, \theta_n) \in s_i | (q_{n-1}, \theta_{n-1}) \in s_j)$, using the trajectories from the DFN simulations. Figure 16 shows the transition matrix averaged over all realizations for each transmissivity distribution, using $k = 1$ fracture segment as the modeling step. As σ increases, the correlation between successive velocities also increases, though the bandwidth of the transition matrices for velocities was larger than the transition matrices for speeds. As with the MDRW, a BTE model that used only one velocity state would have uncorrelated steps, so BTE could be run in both correlated and uncorrelated forms for comparison. Each particle transitions through space and time according to Equation 8, with:

$$\begin{aligned} &f_{BTE}(\delta x, \delta y, \delta t) = f(d_n \cos\theta_n, d_n \sin\theta_n, \delta t_n | (q_n, \theta_n) \in s_i) \\ &P((q_n, \theta_n) \in s_i | (q_{n-1}, \theta_{n-1}) \in s_j) \end{aligned} \tag{13}$$

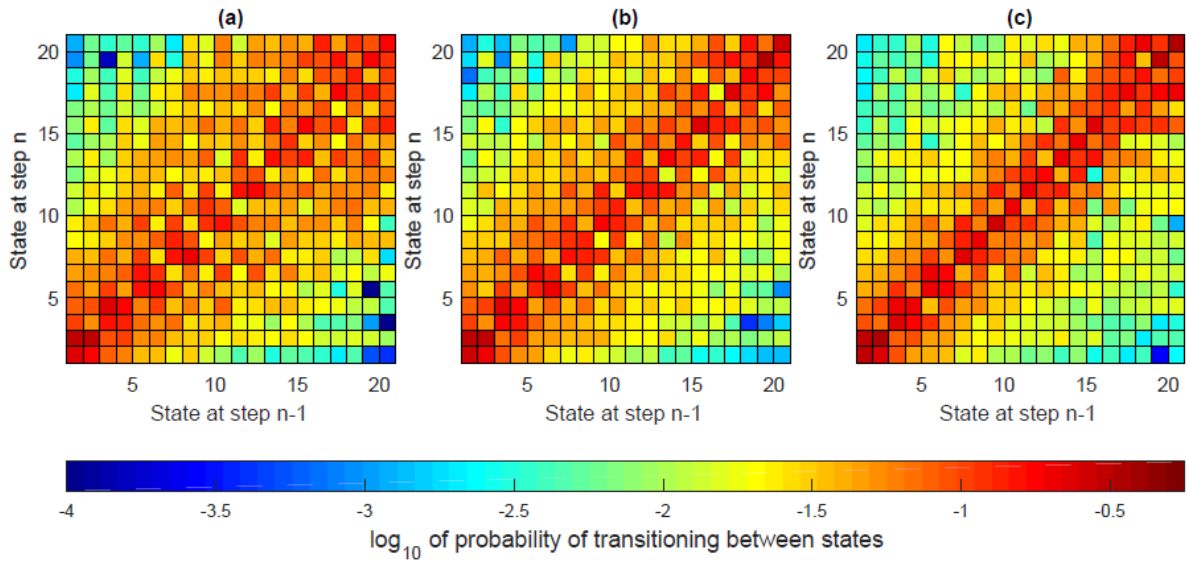

Figure 16. Ensemble averaged transition matrix ($P((q_n, \theta_n) \in si|(q_{n-1}, \theta_{n-1}) \in s_j)$) over all realizations with modeling step size $k = 1$ fracture segments for transmissivity distributions with (a) $\sigma = 0$, (b) $\sigma = 0.5$, and (c) $\sigma = 1$.

Spatial Markov Model (SMM)

The SMM model was introduced in Le Borgne *et al.* (2008). It models correlation between steps with a Markov chain based on speed over fixed longitudinal spatial increments of length L. It defines steps ($\delta x_n = L$, δy_n, δt_n) to correspond to transport over increments of length L in the longitudinal direction. In a sense, this means that the correlations between velocities at different spatial locations are projected onto the axis longitudinal to transport and implicitly assumed to be the dominant correlations in the DFN. To keep the average modeling scale the same for all models, $L = L_k$ was set to be the average longitudinal step taken by particles over k fracture segments:

$$L_k = \frac{1}{N}\sum_{i=1}^{N} r_i cos\theta_i \tag{14}$$

where r_i and θ_i are the length and angle of trajectory i over k segments, and N is the number of trajectories. For $k = 1, 2, 3$ fracture segments, $L_k = 3, 5, 7$ m, respectively. The trajectories from the DFN simulations were then used to create breakthrough curves along the parameterization region at increments of length L_k (e.g., for $k = 2$, we created 20 breakthrough curves, each at 5 m increments). Then, for each location X, the distribution of travel times, $f_t(X, t)$, was found using Equation 16.

To account for correlation between steps, a set of 20 discrete equiprobable states was defined based on travel times. Because L_k was fixed, this was equivalent to defining states based on speed, as in the MDRW. Each state was defined by a travel time range, which for state s_i is l_{i-1} to l_i, where $l_0 \equiv 0$. The transition matrix was then approximated, which was the conditional probability $P(\delta t_n \in s_i|\delta t_{n-1} \in s_j)$, using the trajectories from the DFN simulations.

Figure 17 shows the transition matrix averaged over all realizations for each transmissivity distribution. As with speeds (Figure 15) and velocities (Figure 16), as σ increased, the correlation between successive travel times also increased. The bandwidth of the SMM transition matrices was wider than that of the MDRW transition matrices, but smaller than that of the BTE transition matrices. As with both the MDRW and BTE models, an SMM model that used only one travel-time state would have uncorrelated steps, and therefore the SMM could also be run in both correlated and uncorrelated forms for comparison. Each particle transitions through space and time according to Equation 8, with:

$$f_{SMM}(\delta x, \delta y, \delta t) = \delta(L - \delta x_n) f(\delta y_n, \delta t_n | \delta t_n \in s_i) \\ P(\delta t_n \in s_i | \delta t_{n-1} \in s_j). \tag{15}$$

Versions of this model have been successfully applied to transport through DFNs (Kang *et al.*, 2011, 2017), and even in real fractured rock (Kang *et al.*, 2015). Further details of the model are provided in Le Borgne *et al.* (2008).

All three upscaled random walk models are quite similar and they all rely on Markov chains. The states of the Markov chains differ between models, from the simplest model that relies on longitudinal flux (SMM), to total flux (MDRW), to the most complicated model that relies on full velocity (BTE). Model intercomparison allows us to determine the extent of the velocity information required to properly account for correlation, whereas model intracomparison allows us to determine whether correlation needs to be accounted for at all. The challenge with all of the models is to ensure sufficient parameterization. This challenge was reduced for the uncorrelated versions of the models because the transition matrices required more information than the distribution $f(\delta x, \delta y, \delta t)$.

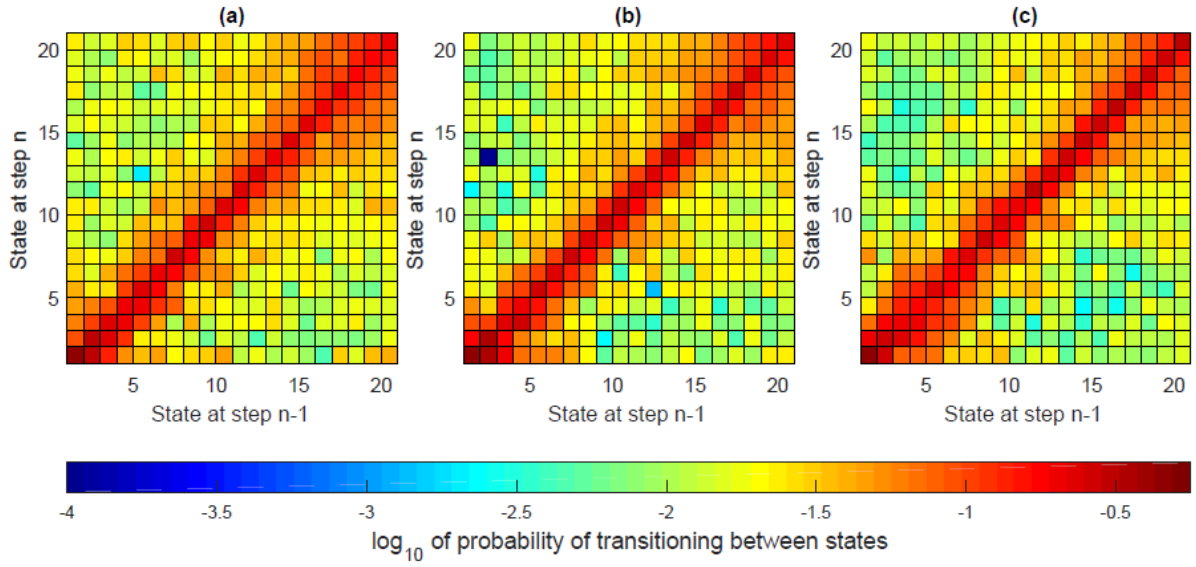

Figure 17. Ensemble averaged transition matrix ($P(\delta t_n \in s_i | \delta t_{n-1} \in s_j)$) over all realizations with modeling step size $L_k = 1$ (the average length of 1 fracture segment) for transmissivity distributions with (a) $\sigma = 0$, (b) $\sigma = .5$, and (c) $\sigma = 1$.

Results

This section compares the breakthrough results of the upscaled random walk models to the large-scale DFN simulations. Each upscaled model was run using three different modeling scales for which the number of fracture segments used to define a step was $k = 1, 2, 3$. Furthermore, each model was run in both correlated and uncorrelated forms. The uncorrelated forms differ from the correlated forms in that their corresponding Markov chains consist of a single state. Here, these uncorrelated models are referred to as uMDRW, uBTE, and uSMM.

A breakthrough curve at location X is a measure of concentration arriving at that location related to the distribution of the time it takes particles to arrive at the location by:

$$f_\tau(X,t) = \int_{-\infty}^{\infty} \frac{C(x=X,y,t)}{C_{tot}(X)}\,dy \tag{16}$$

where $f_\tau(X, t)$ is the probability of a particle arriving at location X at time t; $C(x = X, y, t)$ is the concentration of solute arriving at location X, y at time t; and $C_{tot}(X)$ is a normalization constant, which is the integral of $C(x = X, y, t)$ over all time. Because of the constant head boundary conditions in the transverse direction (as opposed to no-flow boundary conditions), particles are free to leave the model through the transverse boundaries, and therefore C_{tot} is not equal to the amount of concentration initially injected. The metrics used to test the accuracy of each model are:

1) Relative mean absolute error (MAE) in the ensemble cumulative travel time distributions, $F_\tau(X, t)$ at $X = 500$ m and $X = 1$ km.
2) Relative MAE in total mass in ensemble breakthrough curves, $C_{tot}(X)$, at ten intervals of 100 m length along the entire domain ($X = 100$, 200, ... 900, 1,000 m).

To calculate the relative MAE in $F_\tau(X, t)$, we discretize time into 100 one-day increments up to the longest travel time from the DFN simulations. The error is then defined as:

$$rMAE\left(F_{\tau,mod}(X)\right) = \frac{\sum_{i=1}^{n} |F_{\tau,DFN}(X,t_i) - F_{\tau,mod}(X,t_i)|}{\sum_{i=1}^{n} F_{\tau,DFN}(X,t_i)} \tag{17}$$

where $F_{\tau,DFN}(X, t_i)$ and $F_{\tau,mod}(X, t_i)$ are the cumulative travel time distributions at time t_i for the DFN and upscaled model simulations, respectively. The relative mean absolute error in $C_{tot}(X)$ is defined as:

$$rMAE(C_{tot}) = \frac{\sum_{i=1}^{10} |C_{tot,DFN}(X_i) - C_{tot,mod}(X_i)|}{\sum_{i=1}^{10} C_{tot,DFN}(X_i)} \tag{18}$$

where $C_{tot,DFN}(X_i)$ and $C_{tot,mod}(X_i)$ are the total mass in the breakthrough curves at location X_i for the DFN and upscaled model simulations, respectively.

These metrics were chosen so that errors in prediction of longitudinal and transverse transport were kept separate. The errors in the cumulative travel time distribution reflected how well the models were predicting longitudinal transport, whereas the total mass in the breakthrough curves reflected how well the models were predicting transverse transport, because any mass not contained in the breakthrough curve escaped the domain through a transverse boundary. Because of the boundary conditions and the high aspect ratio of the domain, C_{tot} was found to be a better measure of transverse behavior than spatial moments.

Longitudinal Predictions: Error in the Ensemble Cumulative Travel-time Distributions

Figure 18 shows the cumulative and complementary cumulative (defined as the probability of a variable taking a value greater than a specific number) travel time distributions at x = 500 m of DFN simulations with each transmissivity distribution (σ = 0, .5, 1) and of upscaled random walk model simulations with modeling step k = 1 and the corresponding error (calculated using Equation 17). By looking at the cumulative density function (CDF) on a log-log scale, one can zoom in on how well each model captured the pre-peak portion of the breakthrough curve. For σ = 0 (Figure 18a), the SMM predicted too much early breakthrough and the uBTE predicted too little, meaning that fast particles were too fast in the SMM model and too slow in the uBTE model. The predictions of the other models were nearly identical and close to the DFN result. By looking at the complementary cumulative density function (CCDF) on the same scale, one can zoom in on how well each model captured the tail of the breakthrough curve. The uSMM and SMM captured the tail of the DFN result well, but all other models predicted too much late breakthrough, meaning that the slow particles in these models were too slow. For σ = 0.5 (Figure 18b), the CDF showed that the MDRW and BTE overpredicted early breakthrough almost as much as the SMM did. The predictive capability of each model on the tailing behavior was unchanged with changing σ. This can be seen in the relative error in Figure 18d by the error in the SMM dipping below those of the MDRW and BTE. This indicates that for σ = 0.5, correlation was negligible and accounting for correlation in this situation led to increased error, particularly at early times. For σ = 1 (Figure 18c), the CDF showed that the uncorrelated models severely under predicted the early breakthrough, whereas the correlated models come closer to capturing the true DFN behavior. This indicated that for σ = 1, correlation was important and accounting for it led to decreased error. For this situation, the BTE model predicted the tailing behavior best. Both SMM models initially predicted the tailing behavior well, but deviated from the DFN result at very long times (over 105 days), likely because the transport process was projected onto the longitudinal axis for the SMM. With the significant difference in early breakthrough predictions, the correlated models edged out their uncorrelated counterparts in relative error, as shown in Figure 18d.

The only model that predicted both the early and late breakthrough well was the uSMM, which had the lowest relative error, and the only model that predicted both breakthroughs poorly was the uBTE, which had the highest relative error, with the error of the other models falling in between. Figure 18d also shows the range of errors of each individual realization of the DFN simulations (yellow boxes). These were not typical error bars, because the error in the ensemble prediction could be below the error bar (in fact, the ensemble error of the DFN simulations was by definition 0, whereas the realization error

range, shown in yellow, was not). The ensemble predictions for all models were within the range of error of an individual DFN simulation. This suggests that the upscaled ensemble models can predict ensemble DFN behavior as well as individual DFN realizations can.

The layout of Figure 19 is the same as Figure 18, but shows breakthrough results at $X = 1$ km. Qualitatively, model performance continued as shown in Figure 18, so how the models compared with each other didn't change when considering this farther breakthrough curve. The early breakthrough behavior of the BTE model for $\sigma = 0.5$ began to improve, as shown in Figure 19b, but this change did not greatly affect the overall relative error (shown in Figure 19d).

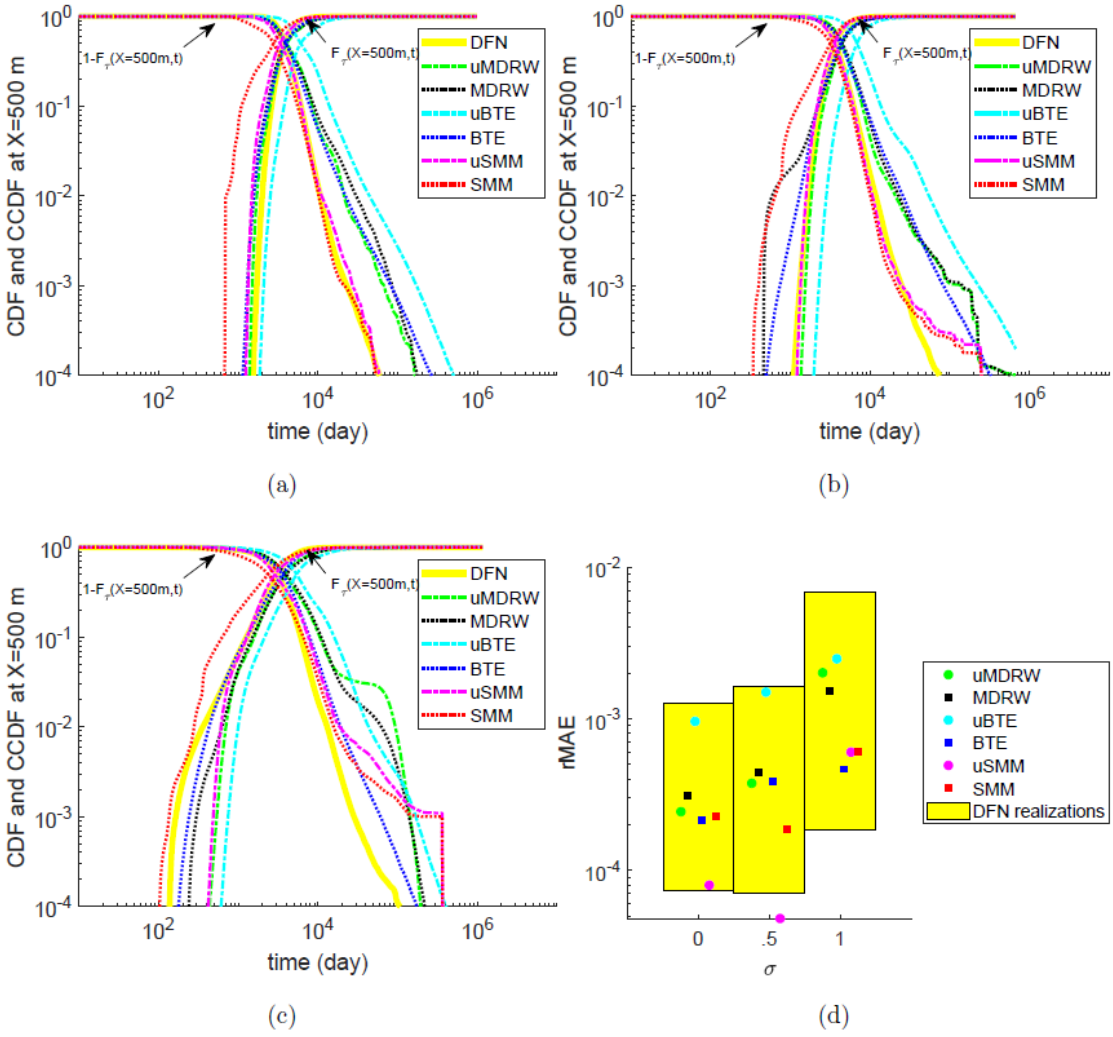

Figure 18. Ensemble cumulative and complementary cumulative travel time distributions at $x = 500$ m of DFN simulations and of upscaled random walk model simulations with modeling step size $k = 1$ with transmissivity distributions (a) $\sigma = 0$, (b) $\sigma = .5$, and (c) $\sigma = 1$, and (d) the corresponding relative error. The range of errors among individual realizations are also shown with error bars for the upscaled models and with a shaded yellow region for the DFN simulations.

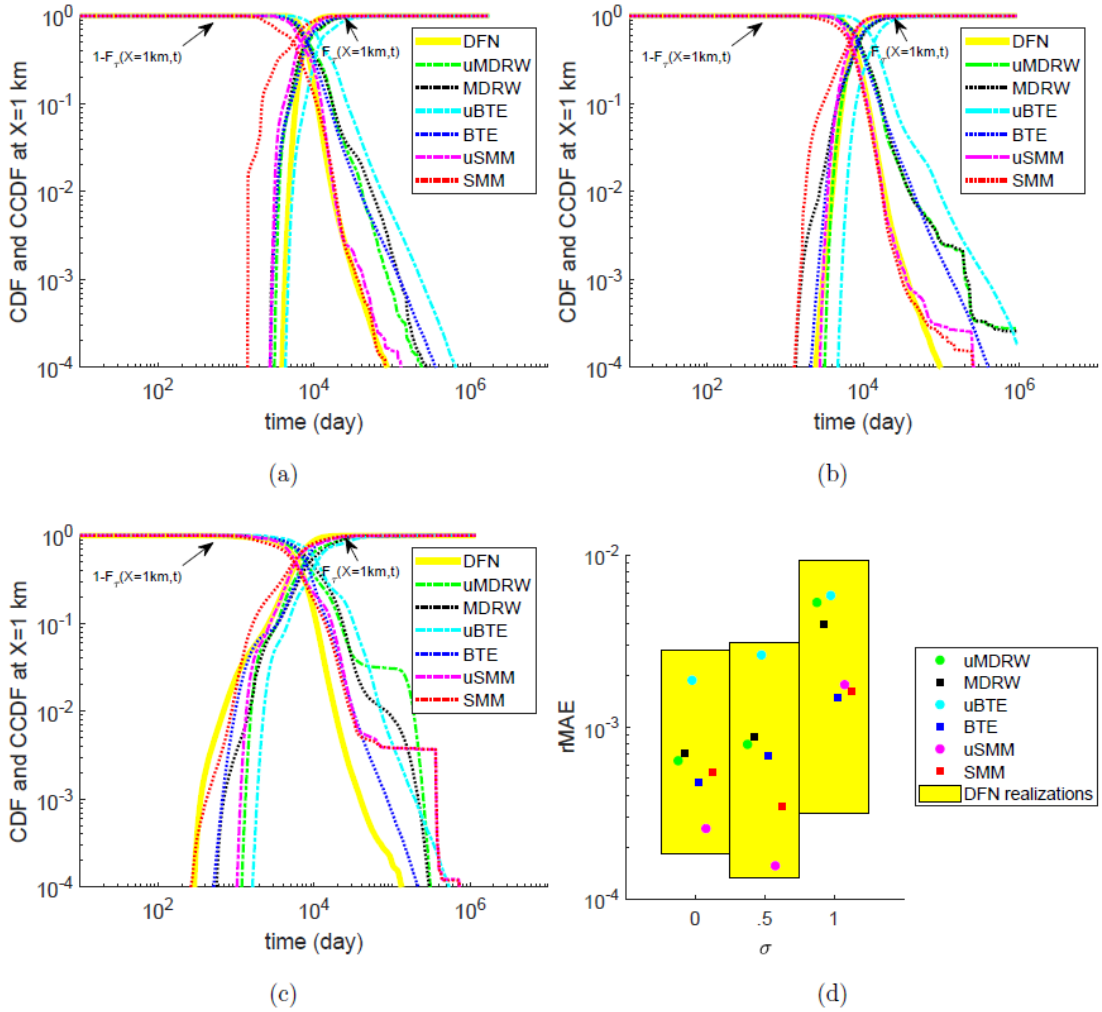

Figure 19. Ensemble cumulative and complementary cumulative travel time distributions at $x = 1$ km of DFN simulations and of upscaled random walk model simulations with modeling step size $k = 1$ with transmissivity distributions (a) $\sigma = 0$, (b) $\sigma = 0.5$, and (c) $\sigma = 1$, and (d) the corresponding relative error. The range of errors among individual realizations are also shown with error bars for the upscaled models and with a shaded yellow region for the DFN simulations.

Transverse Predictions: Error in Total Mass in Ensemble Breakthrough Curves

Figure 20 shows the total mass in each ensemble breakthrough curve, taken at 100 m increments, for each fracture transmissivity distribution ($\sigma = 0, .5, 1$) and the corresponding error (calculated using Equation 18). These predictions were made again using $k = 1$ fracture segment. The mass was calculated by letting the initial injected concentration $C_0 = 1$ so that if all particles arrived at the breakthrough location at some time, then $C_{tot} = 1$.

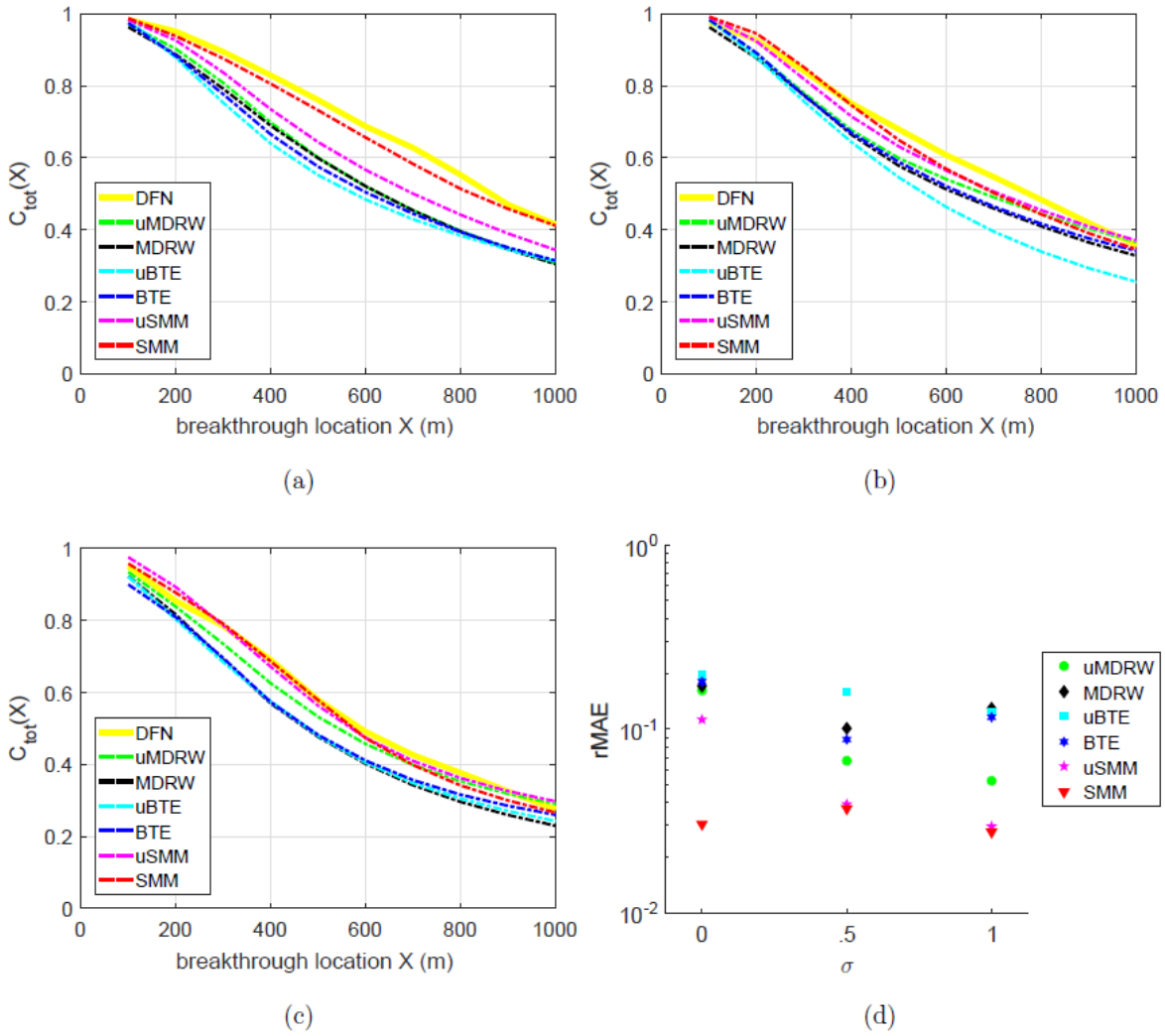

Figure 20. Total mass in ensemble breakthrough curves of DFN simulations and of upscaled random walk model simulations with modeling step size $k = 1$ with transmissivity distributions (a) $\sigma = 0$, (b) $\sigma = 0.5$, and (c) $\sigma = 1$, and (d) the corresponding average relative error.

For $\sigma = 0$ (Figure 20a), at the first breakthrough location ($X = 100$ m) all model predictions came close to the total mass in the breakthrough curves of the DFN simulations, but at farther distances, most of the models began to underpredict the total mass. This means that most of the models predicted an overly high degree of spreading in the transverse direction. The SMM outperformed all of the models at all breakthrough locations, followed by the uSMM. As the spread of fracture transmissivity increased, from Figure 20a through 20c, the total mass predictions of the uSMM and uMDRW improved and the results of the uSMM became similar to those of the SMM. These trends can also be seen in the error in Figure 20d. It was a surprise that the model that treated transverse behavior in the most trivial fashion (the SMM that takes δy from the transverse jump over fixed longitudinal steps, rather than from actual fracture segment geometry) was the one that best predicted the transverse behavior.

Effect of Changing Modeling Scale

Figure 21 shows how the model predictions changed as the modeling scale increased from $k = 1$ to $k = 3$ fracture segments for simulations with constant transmissivity distribution ($\sigma = 0$). Although the longitudinal errors tended to decrease with larger modeling scales, the transverse behavior of each model was not significantly changed by varying the modeling scale over this range, as can be seen in the relatively constant errors of each model as k increases. This trend existed for all three values of σ.

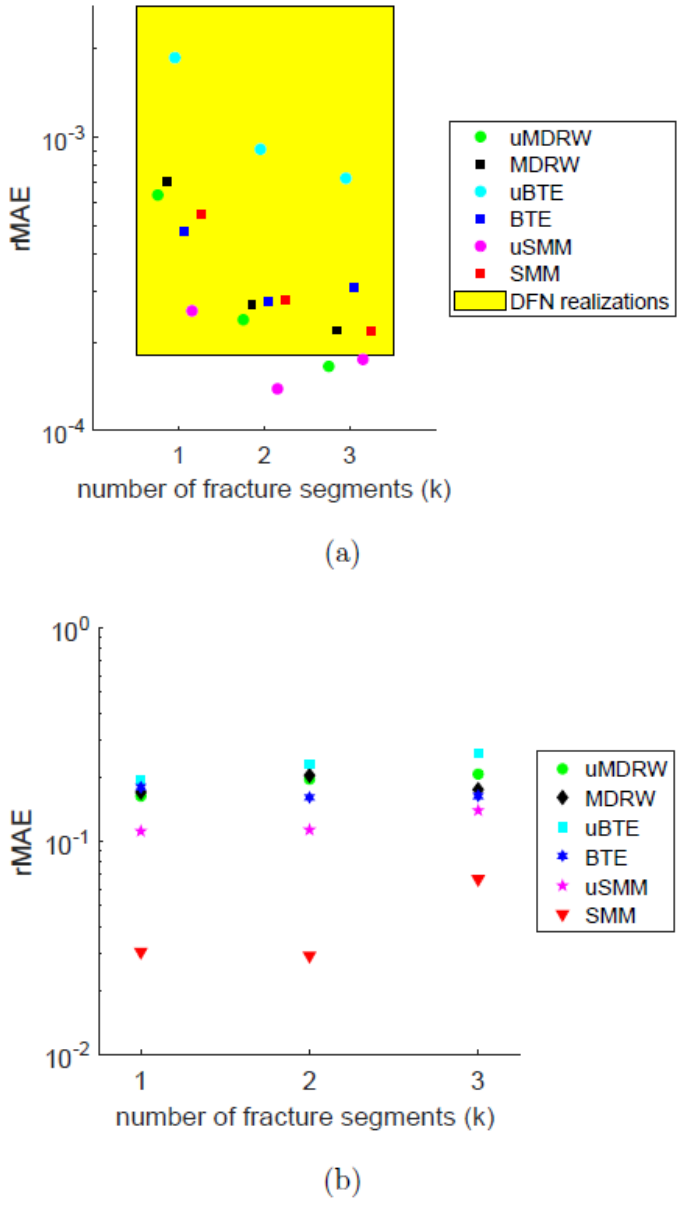

Figure 21. Relative errors in upscaled ensemble random walk model simulations as a function of modeling scale for $\sigma = 0$: (a) relative error in cumulative breakthrough at $X = 1$ km and (b) average relative error in mass.

Discussion of the Methods

All of the upscaled random walk models were able to predict the ensemble DFN breakthrough as well as a single DFN realization could (see the yellow boxes in the error plots in Figures 18 and 19 showing the range of errors in individual DFN realizations). However, there were differences in model predictions, so the best model to use depends on what behavior the model is meant to capture. As the distribution of fracture transmissivity widens, preferential pathways for solute form, creating correlation in particle velocities over successive steps. For the log-normal transmissivity distributions used here, models which take correlation into account begin to gain an advantage over their uncorrelated counterparts when $\sigma = 1$. Early breakthrough is best predicted by the uncorrelated models (uMDRW and uSMM) for $\sigma < 1$ and by the correlated models (MDRW, BTE, SMM) for $\sigma = 1$. Tailing behavior is best predicted by the SMM models (uSMM, SMM) for $\sigma < 1$ and by the correlated BTE model for $\sigma = 1$. In comparison to the effects of model choice and correlation, the effect of modeling scale (number of fracture segments used to define modeling steps) on model predictive performance is negligible, at least over the range covered here.

Throughout this section, particles represent a conservative solute. However, if the solute to be modeled is nonconservative and degrades over time, as in the case of radionuclides in Pahute Mesa, it is most important that the model predict early breakthrough well. Alternatively, for situations in which the solute is a contaminant and modeling pump-and-treat remediation is desired, it is most important that the model predict the breakthrough curve tail well. In these cases, the best model depends on the fracture transmissivity distribution. If there are no-flow boundary conditions on the transverse sides of the domain, then the error in total mass can be ignored. Otherwise, using an SMM, either correlated or uncorrelated, will better capture the transverse spreading.

CALIBRATION OF 3-D DFNs TO FLOW DATA

Full characterization of fractured rock masses was not possible because known fracture locations and their attributes consisted of an extremely small sample of the overall fracture network (i.e., any fracture characterization effort grossly undersampled a field site because of limited accessibility to the fractures themselves). However, fracture data can be used to generate representative, site-specific fracture networks through the derivation of probabilistic descriptions of fracture location, orientation, spacing, length, aperture, and values of network density. Of these different fracture properties and the network, aperture is generally the parameter that cannot be easily inferred from field data or inspection of the cores. However, fracture aperture has immense influence on flow and transport, and reducing its uncertainty is key to developing a model with an accurate description of groundwater velocity. This section focuses on using 3-D DFN models—built with site-specific probabilistic descriptions of fracture length, orientation, and density—to obtain realistic ranges of fracture aperture values by calibrating the model to field data of the hydraulic head distribution. The fracture aperture here refers to the distance between opposite walls of a fracture in a parallel plate model (i.e., the mechanical aperture). The hydraulic aperture (related to the flow capacity) or the transport aperture (related to the residence time) are not explicitly modeled here. The conceptualization of the problem here hinges on the assumption of smooth parallel plates where the entire void space of fractures is available for water flow

and solute transport. The model development and calibration approach used in this study was general in nature, and it was applied to WPM's BULLION FGE—a tracer test at the well field of ER-20-6 adjacent to the BULLION test conducted in the summer of 1997 (June 2 to August 28). The purpose of the BULLION FGE was to provide information relevant to the transport of radionuclides in groundwater.

DFN Model Development and Parametrization

Discrete fracture networks were generated stochastically, using the data from fractured rock characterizations studies. Data on the fracture attributes needed to generate a fracture network are: (1) mean fracture orientation for each fracture family and probability distribution for orientation; (2) fracture shape and size for each fracture family and probability distribution for fracture size; and (3) fracture intensity, P_{32} (m^2/m^3), defined as the ratio of total fracture surface area over volume, and relative intensity for each fracture family. The model was developed in dfnWorks, which has three modules: dfnGen, dfnFlow, and dfnTrans (see the "3-D DFN: dfnWorks" section). dfnGen stochastically generated 3-D DFNs, removed isolated fractures using the FRAM (Hyman *et al.*, 2014), and created high-quality conforming Delaunay triangular meshes on the generated DFNs using the LaGriT meshing toolbox (Los Alamos National Laboratory, 2013). Near fracture intersections, the mesh was refined to allow for smooth and accurate representation of high-pressure gradients and sharp velocity contrasts. Discretization of the mesh was coarsened farther away from fracture intersections to reduce computational costs. The FRAM overcame the principal issue of resolving a tiny feature in a DFN by prescribing a minimum length scale (h) and restricting the generation of the network to only create features of that size and larger. Once a network was constructed and meshed, the dfnFlow module solved for steady-state saturated flow conditions using the massively parallel, open-source, subsurface flow and reactive transport finite volume code PFLOTRAN (Lichtner *et al.*, 2015). Finally, dfnTrans, an extension of the WALKABOUT particle tracking method (Makedonska *et al.*, 2015; Painter *et al.*, 2012) was used to determine pathlines through the DFN and simulate solute transport. dfnWorks does not currently have a well package to simulate groundwater levels and particle tracking to a well. This study used the method presented in the "Representation of a Well in 3-D DFN" section to represent a well in a 3-D DFN.

Fractures were conceptualized as two parallel planes in DFN models. Rock matrix was considered impermeable and fracture networks were simulated explicitly. Fracture permeability was related to fracture aperture using the Cubic law:

$$k_f = b^2/12 \tag{19}$$

where k_f is fracture permeability and b is fracture aperture. Popular conceptualizations of fracture apertures are: (1) constant fracture apertures (CFA) in which fractures are assigned the same aperture values regardless of their size or geologic origin (e.g., tectonic fractures and joins), (2) lognormal distribution apertures (LNAs) in which fractures follow a lognormal distribution, and (3) the length correlated aperture (LCA) model (Klimczak *et al.*, 2010). Fracture apertures in LCA models are a function of fracture sizes such as:

$$b = FR^k \tag{20}$$

where F is a first parameter in the LCA model, k is a second parameter, and R is a mean radius of a polygon.

Boundaries in this study were either no flow, or constant values of hydraulic head were used to assign boundary conditions to a DFN model. For the scenario in which there was a pumping well, hydraulic head at the boundaries was adjusted to reflect increased drawdown because of water extraction.

Model Calibration

Model calibration was the process of adjusting model parameter values until a satisfactory fit between model outputs and field measurements (e.g., heads and concentrations) was achieved. Model calibration can be broadly grouped into manual model calibration based on trial-and-error methods, or automatic model calibration approaches. Manual model calibration based on trial-and-error methods was easy to apply but time-consuming. Trial-and-error methods also may not guarantee finding the best solutions because manipulations by different users may produce dissimilar solutions. This method is suitable for a simple, linear model with a small number of uncorrelated model parameters.

Automatic model calibration using optimization methods is efficient because of its ability to handle a high number of model parameters and the accuracy of solutions. Optimization methods can be classified as derivative-based and nonderivative-based search methods (global search methods). Derivative-based methods converge quickly, but solutions may be trapped to local optima. Global search methods have potential to find near-global solutions, as well as handle nondifferentiable and discontinuous functions. Popular global search methods applied to groundwater model calibration included genetic algorithms (El Harrouni *et al.*, 1996; Wang, 1997; Karpouzos *et al.*, 2001), simulated annealing and tabu search (Zheng and Wang, 1996), ant colony optimization (Abbaspour *et al.*, 2001), particle swarm (Gill *et al.*, 2006; Krauße and Cullmann, 2012), and shuffled complex evolution (SCE) (Vrugt *et al.*, 2003). The common disadvantage of global search methods is that a large number of model runs and iterations are needed to reach a near-global solution. For a computationally expensive simulation model, this method may become impractical. Reviews and comparisons of methods for model calibration can be found in many books and articles (Cooley, 1985; Sun, 1994; Hunt *et al.*, 2007; Hill and Tiedeman, 2007; Vrugt *et al.*, 2008; Hendricks Franssen *et al.*, 2009; Fienen *et al.*, 2009; Doherty, 2015; Yeh, 2015). Popular software for automatic groundwater model parameter estimation includes PEST (Doherty *et al.*, 1994), UCODE (Poeter and Hill, 1999), or MGO (Zheng and Wang, 2003).

Choosing a suitable approach depends on many factors, including the number of model parameters, the model run time, the model linearity (linear versus nonlinear). Two of the three aperture models used for this study (LNA and LCA) were two-parameter models. The CFA is a single-parameter model. dfnWorks, being a computationally intensive software, requires a long run time on parallel machines. However, the flow problem is linear because of the assumption of saturated conditions and Darcy flow. Because of these reasons, the simple trial-and-error based calibration method was used in this study.

Case Study: The BULLION Forced-gradient Experiment (FGE)

The BULLION FGE was designed to use tracer migration in groundwater to provide information on transport parameters (IT Corporation, 1998). A set of three wells, installed into fractured lava-flow aquifer and in alignment with the orientation of the major fracture system, was subjected to a tracer test. The downgradient well was pumped at a long-term average pumping rate of 632.32 m^3/day (116 gallons per minute). Tracers were injected into the other two wells, and tracer breakthrough curves were captured. The experiment was conducted for a long duration of 87 days to accommodate slower-than-predicted breakthrough of the tracers. Tracer concentrations for each well were determined at closely spaced time intervals to define the breakthrough curves. The objective was specifically to observe the transport process and characterize transport parameters (e.g., effective porosity, dispersivity, and matrix diffusion) for use in predictive modeling of contaminant transport (IT Corporation, 1998). Continuum models with regular structured meshing were used to meet this objective. The work presented here was motivated by the possibility of determining fracture properties more accurately when a DFN model was used in place of traditional approaches to simulate contaminant transport.

Figure 22 shows the location of the BULLION FGE in Pahute Mesa downgradient of the BULLION test. The well farthest from the test was pumped to produce a hydraulic gradient while tracers were injected into the other two wells. Tracer breakthrough curves were obtained for different flow path segments. Several methods were adopted to simulate

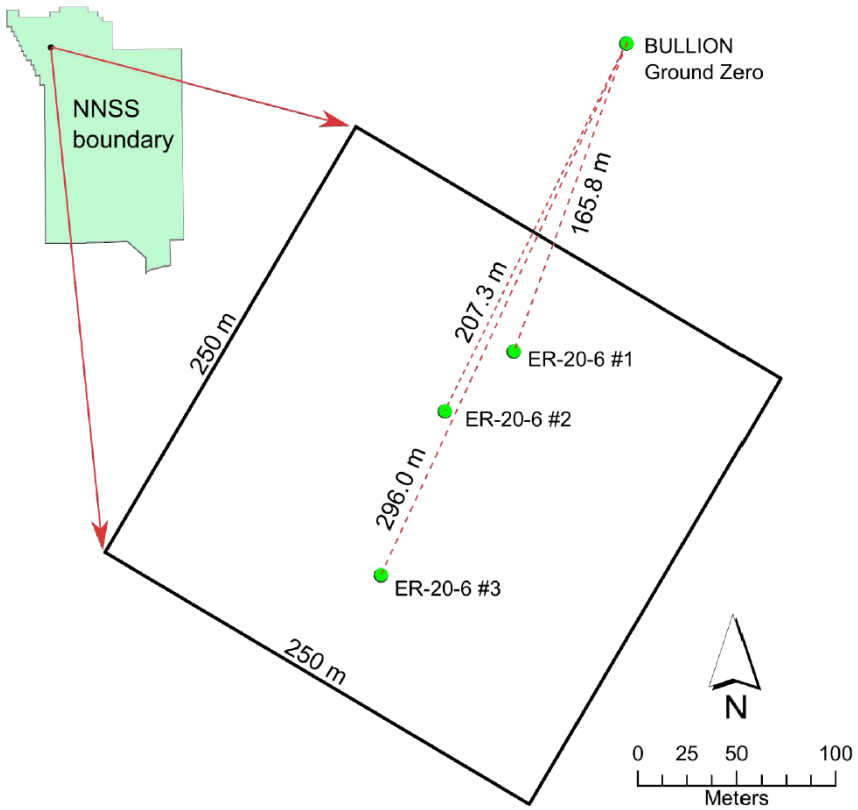

Figure 22. Location of the BULLION FGE in Pahute Mesa of the Nevada National Security Site.

the BULLION FGE (IT Corporation, 1998). The first method based on porous media theory (Theis analysis) indicated that the formation beneath the BULLION site could be modeled as a porous media, but is insufficient to fully capture the transport behavior of a fractured heterogeneous media. The second approach was based on dual-porosity analysis. Results revealed that the matrix conductivities were much lower than the fracture conductivities, supporting the conceptualization that fracture flow dominates groundwater movement.

DFN Model for BULLION FGE

This study focused on a portion of the BULLION FGE where particles were injected at well ER-20-6 #1 and pumping was conducted at well ER-20-6 #3 with a pumping rate of 7.32 L/s (116 gallons per minute). The flow direction was from well ER-20-6 #1 to well ER-20-6 #3. The flow condition at the end of pumping reached steady state. The drawdowns are 1.44 m, 1.61 m, and ~7.0 m at the end of the pumping test (87 days) for wells ER-20-6 #1, #2, and #3, respectively (Geldon, 2004). However, the observed drawdown was somewhat noisy and open to interpretation. IT Corporation (1998) estimated drawdowns at the three wells at approximately 1.15 m, 1.7 m, and 7 m, respectively.

The volcanic rocks that control groundwater flow beneath Pahute Mesa can be grouped into four volcanic hydrogeologic units (HGUs) based mainly on lithology and secondary alteration. These units are lava-flow aquifers (LFAs), welded-tuff aquifers (WTAs), vitric-tuff aquifers (VTAs), and tuff confining units (TCUs). The LFA is divided into four cooling subunits (CSU), or layers. Each layer consists of a mix of orthogonal cooling joints and tectonic fractures, which represent five different fracture sets (Tech. Mem., 2015). This study only focused on the thickest Stoney Lava interior layer. Three cooling joint sets are SP, DP (two steeply dipping, roughly orthogonally striking sets), and BP (gently to moderately dipping, bedding-related set). Two tectonic features were created during deformation across the Basin and Range Province: T1 and T2. Table 3 presents fracture characteristics for the LFA. The data were provided by Golder Associates.

dfnWorks 2.0 (Hyman *et al.*, 2015) was used to generate a 3-D fracture network and simulate flow and conservative transport of the BULLION FGE. Fractures were modeled as a rectangular plane. Three aperture conceptual models (CFA, LNA, LCA) were adopted to investigate fracture aperture and distribution, and how it affected flow and particle transport. Multiple DFN realizations were generated for each conceptual model. Model calibration was carried out for all DFN models.

Table 3. Fracture statistics used to generate 3-D fracture networks.

Orientation set probability model for cooling joints and tectonic fracture.

HSU ID	CSU ID	Fracture Set	Probability Distribution	Mean Pole (°)		Major Axis (°)		Fisher Concentration	
				Trend	Plunge	Trend	Plunge	K / K1	K2
LFA	All	SP	Univariate Fisher	89.12	27.35	n/a	n/a	18.34	n/a
LFA	All	DP	Univariate Fisher	350.48	28.06	n/a	n/a	26.24	n/a
LFA	All	BP	Univariate Fisher	19.39	53.21	n/a	n/a	35	n/a
LFA	All	T1	Univariate Fisher	319.06	18.73	n/a	n/a	35	n/a
LFA	All	T2	Univariate Fisher	48.39	7.85	n/a	n/a	35	n/a

Size model for cooling joints and tectonic fracture.

HSU ID	CSU ID	Fracture Set	Probability Distribution	Parameter Names	Distribution Parameters	Size Truncation	Aspect Ratio
LFA	All	SP	Unit Thickness		n/a	n/a	0.2
LFA	All	DP	Unit Thickness		n/a	n/a	0.2
LFA	All	BP	Exponential	Mean	3.373	Min = 1m	1
LFA	All	T1	Power Law	k_r, r_0	2.6, 1	Min = 1m, Max = 250m	5
LFA	All	T2	Power Law	k_r, r_0	2.01, 1	Min = 1m, Max = 250m	5

Alternative size model for cooling joints, based on outcrop and photographic observations in the Tiva Canyon Tuff.

HSU ID	CSU ID	Fracture Set	Probability Distribution	Parameter Names	Distribution Parameters (m)	Size Truncation	Aspect Ratio
TSA	All	CJ1	Lognormal	Mean, Std. Dev.	1.250, 0.877	Min = 1m, Max = CSU thickness	0.2
TSA	All	CJ2	Lognormal	Mean, Std. Dv.	1.250, 0.877	Min = 1m, Max = CSU thickness	0.2
TSA	All	CJ3	Exponential	Mean	3.373	Min = 1m	1.0

Relative set intensity

Set ID	Relative Set Intensity (%)
SP	50%
DP	13%
BP	4%
T1	32%
T2	1%

3-D Fractured Network Generation and Meshing

Each DFN has five fracture families (three cooling joint sets and two tectonic features). The mean fracture intensity (P_{32}) is 0.446 (m^2/m^3). After 3-D DFNs were generated, meshing for fractures was done automatically by dfnWorks. The parameter *h* (minimum length scale) needed to be carefully considered while constructing the dfnWorks model. As discussed in Hyman *et al.* (2015), *h* should be chosen such that all physical phenomena of interest have natural scales greater than *h*, so they can be well resolved by the

computational mesh while limiting computational expenses. If *h* is too large, then it will be difficult to generate a DFN that meets the density requirements. If *h* is too small, then the computational cost associated with meshing and solving the governing equations will increase. This study used a small *h* value of 0.25 m.

By gradually increasing the model domain sizes, this study found that the BULLION FGE could be simulated properly (in terms of the computational resources available) at a domain size of 250 m × 250 m × 100 m. This domain covers three wells and the entire LFA thickness at the BULLION site. Figure 22 shows the locations of the model domain and the three wells. The domain was simulated as one layer. The time required for generating the DFN network was short (roughly less than five minutes), but the time required for meshing was much longer (e.g., approximately four hours using four cores). To adequately capture the randomness in stochastically generated networks, a total of 30 statistically equivalent realizations of the network was generated. Table 4 summarizes the important statistics of the 30 DFN realizations before and after eliminating isolated fractures. The results showed that the mean and standard deviation of the number of fractures are 10,750±266 fractures. In general, the number of fractures after the isolation process is 10,751, which is 39.4 percent of the number before the isolation (60.6 percent fractures were removed because they were isolated from the backbone).

Figures 23 and 24 show examples of a 3-D DFN. This DFN realization generated 27,729 fractures to obtain a fracture intensity of 0.446 m^2/m^3 (area of fractures/volume of rock mass). Eliminating isolated fractures resulted in 10,892 fractures. For fracture families 1 through 5, the number of fractures were 5,450; 1,494; 306; 3,563; and 73, respectively. Fracture families 1 and 3 dominated the network.

Table 4. Statistics of 30 DFN realizations before and after eliminating isolated fractures**.**

	Mean	**1-stdv**
Before		
Number of fractures	27,267	845
Intersection length (m)	44,392	630
Fracture area (m^2)	2,801,080	4,408
After		
Number of fractures	10,751	266
Intersection length (m)	43,558	609
Fracture area (m^2)	2,221,164	15,630

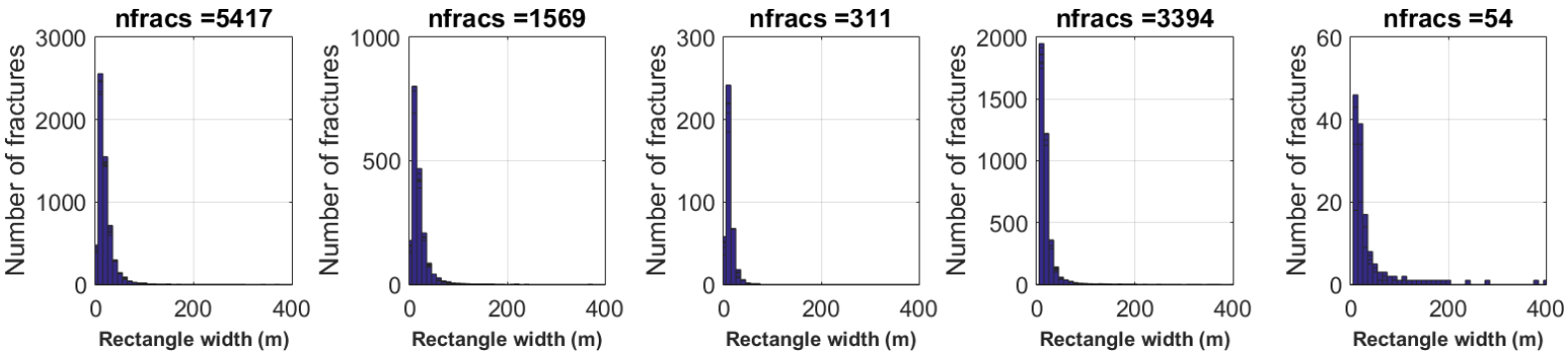

Figure 23. Fracture sizes and their distributions for each of the five fracture families (plots from left to right correspond to families 1 through 5) for a realization.

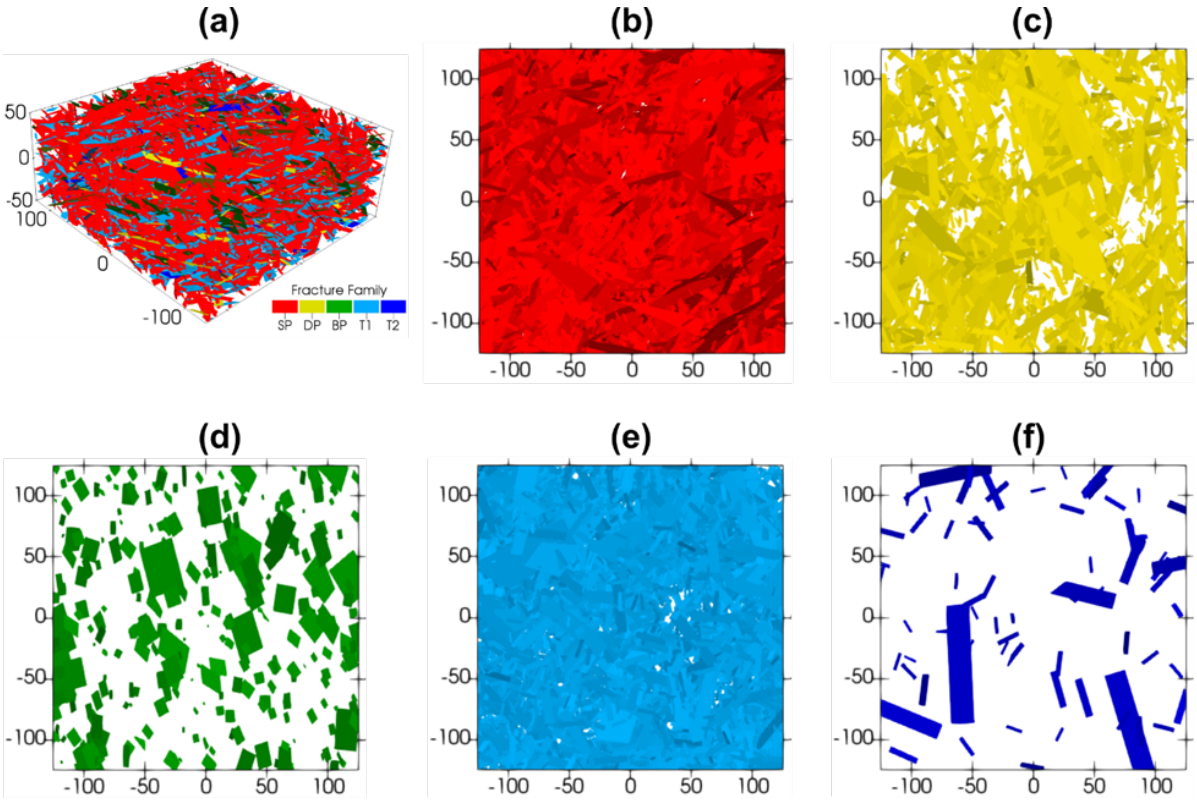

Figure 24. A DFN realization showing (a) all five fracture families, (b) cooling joints SP, (c) cooling joints DP, (d) cooling joints BP, (e) tectonic fracture T1, and (f) tectonic fracture T2.

Flow and Transport Simulation

Constant head boundary conditions were assigned to four sides of the model domain. No-flow boundary conditions were assigned to the top and bottom of the model domain as the LFA was separated from other aquifers by impermeable layers. Because no observation wells were located close to the model boundary, this study interpolated groundwater levels at the boundaries using available groundwater level measurements in the study area. Two sets of head gradients in the north-south directions were specified to consider uncertainty in boundary conditions.

In the first set of boundary conditions (BC1), groundwater levels at the north and south boundaries were extrapolated using observed static groundwater levels at the three wells on June 2, 1997. Groundwater levels at the east and west boundaries were interpolated using the groundwater levels from ER 20-6 #1, ER 20-6 #2, ER 20-6 #3, PM-1, U-20 WW, and UE-20bh 1. The first set represented a scenario of negligible drawdown at the model boundaries because of pumping at ER 20-6 #3. Because pumping would potentially cause drawdown at model boundaries, a second set (BC2) of hydraulic head values were developed to represent the uncertainty in boundary conditions. The second set was similar to BC1 except that the groundwater levels at the end of the pumping test (87 days) were the data used in the interpolation. The north-south hydraulic gradients assigned for BC1 and BC2 were 9/1000 and 11.3/1000, respectively.

An important step in modeling the BULLION FGE was to select a proper well skin radius using the well package described in the "DFN Methods for 2-D and 3-D Models" section to represent the three wells. Different well skin radii were tested by increasing the well skin radius incrementally from 1 m to 10 m. For each test, DFN flow and transport models were run and the number of active flow zones were identified. The study found that using a well skin radius of 10 m allowed adequate intersections between each well and the fracture backbone. One to five active flow zones were found by using the well skin radius of 10 m. This result was consistent with flow zone analyses that used the thermal logs of the three wells in which less than three active flow zones were found for each well.

Figure 25 presents the number of intersections between each well and the fracture backbone where each well was represented by two-orthogonal rectangular fractures of 100 m × 10 m. The number of intersections between fracture backbones and three wells were 11.87±2.42, 11.53±2.25, and 11.67±2.37 for wells ER 20-6 #1, ER 20-6 #2, and ER 20-6 #3, respectively. For the BULLION FGE, a single DFN flow simulation took roughly 50 minutes using four processors, but it only needed 15 minutes using 24 processors. Using the flow solution, dfnTrans was used to study conservative particle transport. For each DFN model run, 50,000 nonreactive particles were uniformly distributed along the well screen of the injection well ER 20-6 #1. Particles were collected at ER 20-6 #3 to analyze BTCs. Each dfnTrans simulation took roughly one hour using a single processor. The dfnTrans run time increased linearly with the number of particles injected and tracking of each particle was done sequentially in the code.

Model calibration was performed to estimate fracture apertures both in terms of the values of their ranges and shape of their distributions. The objection function used in model calibration was the mean of absolute error (MAE between observed and simulated groundwater levels at the two observation wells:

$$MAE = \sum_{i=1}^{n} \left| \bar{h}_i^{cal} - h_i^{obs} \right| / n \tag{21}$$

where n is the number of groundwater level measurements, and h_i^{obs} and $\bar{h}_i^{cal}$ are the observed groundwater levels and the mean of simulated groundwater levels found using 30 DFN model realizations at the location of observation well i.

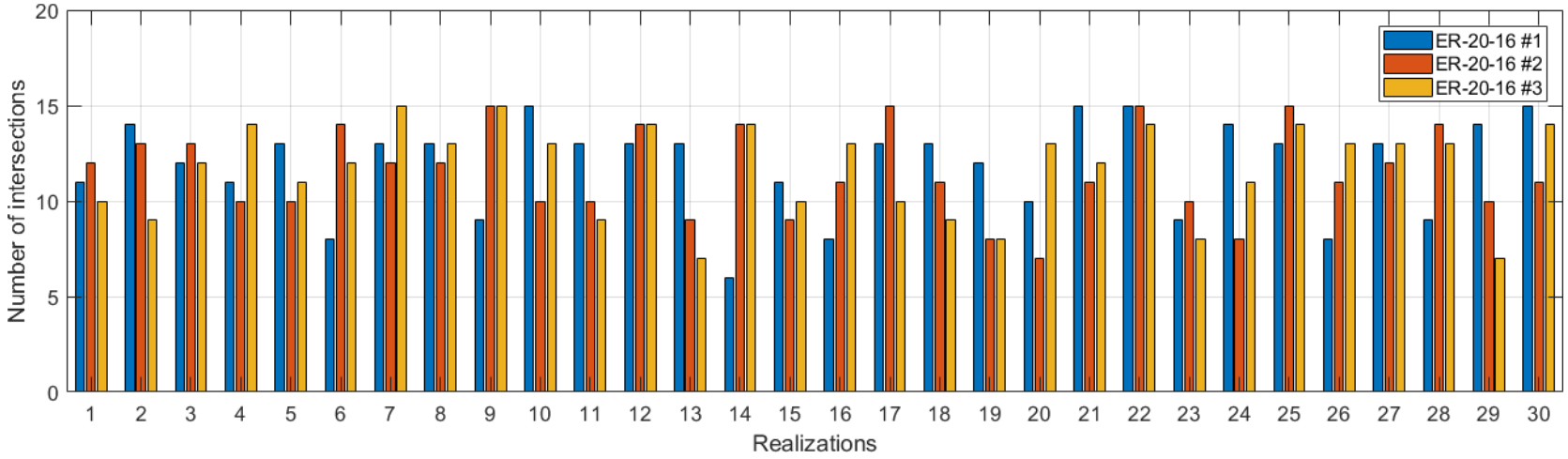

Figure 25. The simulated number of fracture intersections at three wells in the model domain.

Model calibration was conducted for 180 DFN models resulting from 30 realizations for each of the six modeling scenarios (three fracture aperture conceptual models and two sets of boundary conditions). We used the OASIS supercomputer housed at DRI to run model calibration in parallel. The parallel codes based on the embarrassingly parallel algorithm was adopted from Elshall *et al.* (2015). Trial-and-error model calibration was used because the linearity of the DFN models. Model calibration started with an initial guess of an aperture value or distribution and varying this value until the minimum MAE was found. Table 5 shows these results.

Figure 26 presents the trial-and-error runs for three conceptual models of fracture apertures under BC2 boundary conditions. The CFA models were calibrated first because they were the simplest model with only one parameter. Five trial-and-error batches were completed to find an optimal aperture value. For each batch, 30 DFN models were executed and the MAEs were calculated using Equation 21. The CFA model with an aperture value of 480 microns resulted in a minimum MAE of 0.10 m.

Using the estimated apertures from CFA models as a starting point, the LNA and LCA conceptual models were calibrated. Each of these models had two parameters. The strategy was to calibrate one parameter at a time. For LNA models, the mean of the fracture apertures varied from −7.9940 to −7.6417 (natural log base), whereas the standard deviation was as fixed at 0.4. This was equivalent to the mean values from approximately 340 microns to 480 microns (prior to deletion of isolated fractures and segments from the network), whereas the standard deviation was roughly 45 percent of the mean value, varying from 150 microns to 220 microns. The minimum MAE was 0.19 m. The lognormal distribution (−7.7063, 0.4) gave the best solution prior to deletion of isolated fractures and segments. This was equivalent to a fracture network with aperture values (over 30 DFN realizations and after deleting isolated fractures) of 487±203 microns. To calibrate the LCA models, the first parameter, F in Equation 20, was varied from 0.125×10^{-3} to 0.135×10^{-3}. The second parameter was fixed at 0.4. The minimum MAE was 0.10 m. The mean and standard deviation of fracture apertures for each trial model calibration run ranged from 227±61 microns to 255±69 microns. The optimized fracture aperture was 246±66 microns.

Table 5. Optimized fracture apertures and errors between observed and simulated groundwater levels at two observation wells. Fracture apertures were averaged over 30 DFN realizations and after deleting isolated fractures.

No.	Conceptual models	Aperture (microns)	MAE and 1-std deviation (m)		Overall MAE (m)
			ER 20-6 #1	ER 20-6 #2	
1	CFA_BC$_1$	410±0	0.63±0.72	0.52±1.21	0.57
2	LNA_BC$_1$	411±171	0.64±1.04	0.89±2.33	0.77
3	LCA_BC$_1$	208±56	0.64±1.43	0.58±3.17	0.61
4	CFA_BC$_2$	480±0	0.19±0.41	0.01±0.73	0.10
5	LNA_BC$_2$	487±203	0.21±0.59	0.17±1.34	0.19
6	LCA_BC$_2$	241±65	0.14±0.87	0.14±2.01	0.14

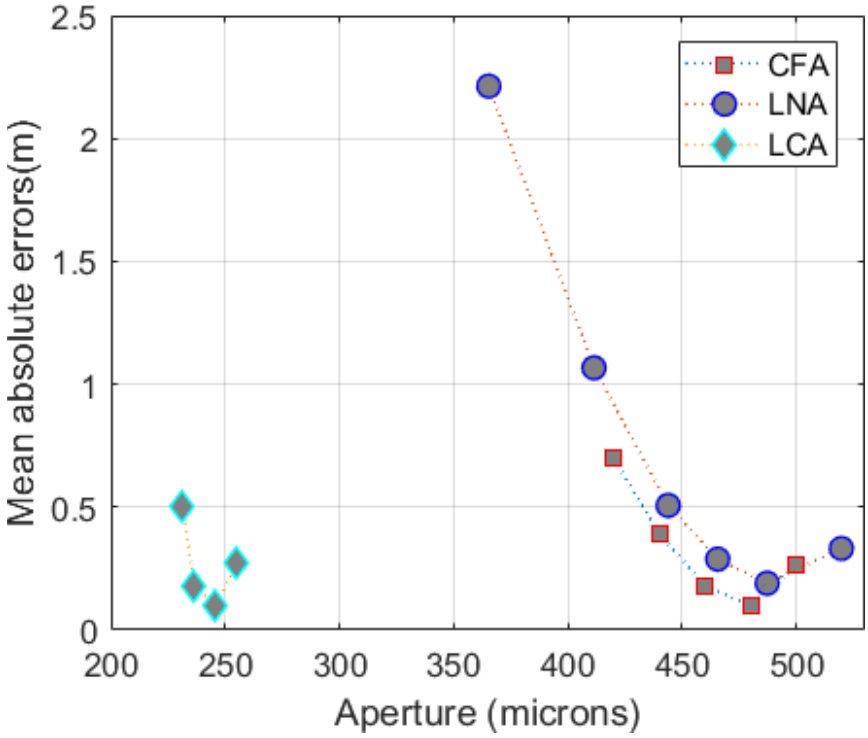

Figure 26. Model calibration convergence profile for the three conceptual models under BC2 boundary conditions. The x-axis shows the averaged fracture apertures by 30 DFN realizations.

Table 5 summarizes the MAEs and estimated fracture values for six calibrated DFN models. The values in Table 5 corresponds to the reduced density network in dfnWorks found after deleting isolated fractures and segments. All calibrated models showed good agreements between observed and simulated groundwater levels represented by overall MAEs of less than 1 m. The MAEs for BC1 models were considerable higher than MAEs for BC2 models. Figure 27 shows the distribution of fracture apertures for three calibrated models under the BC2 boundary conditions.

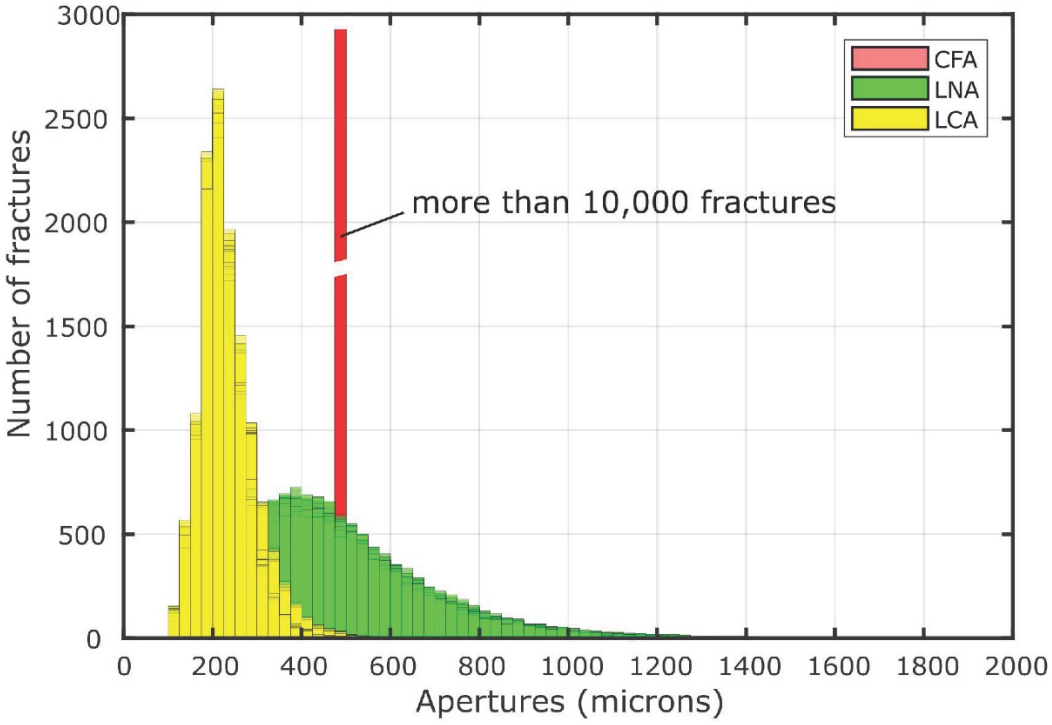

Figure 27. Fracture apertures of three calibrated DFN models under the BC2 boundary conditions. Data are from 30 DFN realizations.

Results

Simulated Groundwater Levels

Figure 28 presents the observed and simulated groundwater levels at observation well ER 20-6 #1 and ER 20-6 #2 for the six calibrated DFN models. Stochastically generated fracture networks showed significant impacts on simulated groundwater levels. Variances of simulated groundwater levels were found at both observation well locations for all six models. For example, the CFA-BC1 model showed one standard deviation of simulated groundwater of 0.72 m and 1.21 m at ER 20-6 #1 and ER 20-6 #2, respectively. The variance of simulated groundwater levels by CFA models were always lower than those simulated by LNA and LCA conceptual models. Uncertainty in groundwater levels at ER 20-6 #2 was always higher than ER 20-6 #1 because ER 20-6 #2 was closer to the pumping well ER 20-6 #3. Models with BC2 boundary conditions (i.e., MAEs varied from 0.10 m to 0.19 m) simulated the groundwater levels better than the models with BC1 boundary conditions (i.e., MAEs varied from 0.57 m to 0.77 m). The second set (BC2) of head gradient boundary conditions accounted for drawdown at four sides of the model domain. Better results with BC2 indicated that the impact of pumping on the boundaries should be accounted for in some way in DFN models. The DFN models with BC2 boundary conditions were therefore used in remainder of this study. Figure 29 shows different views of groundwater level distributions in a calibrated CFA-BC2 model for illustration.

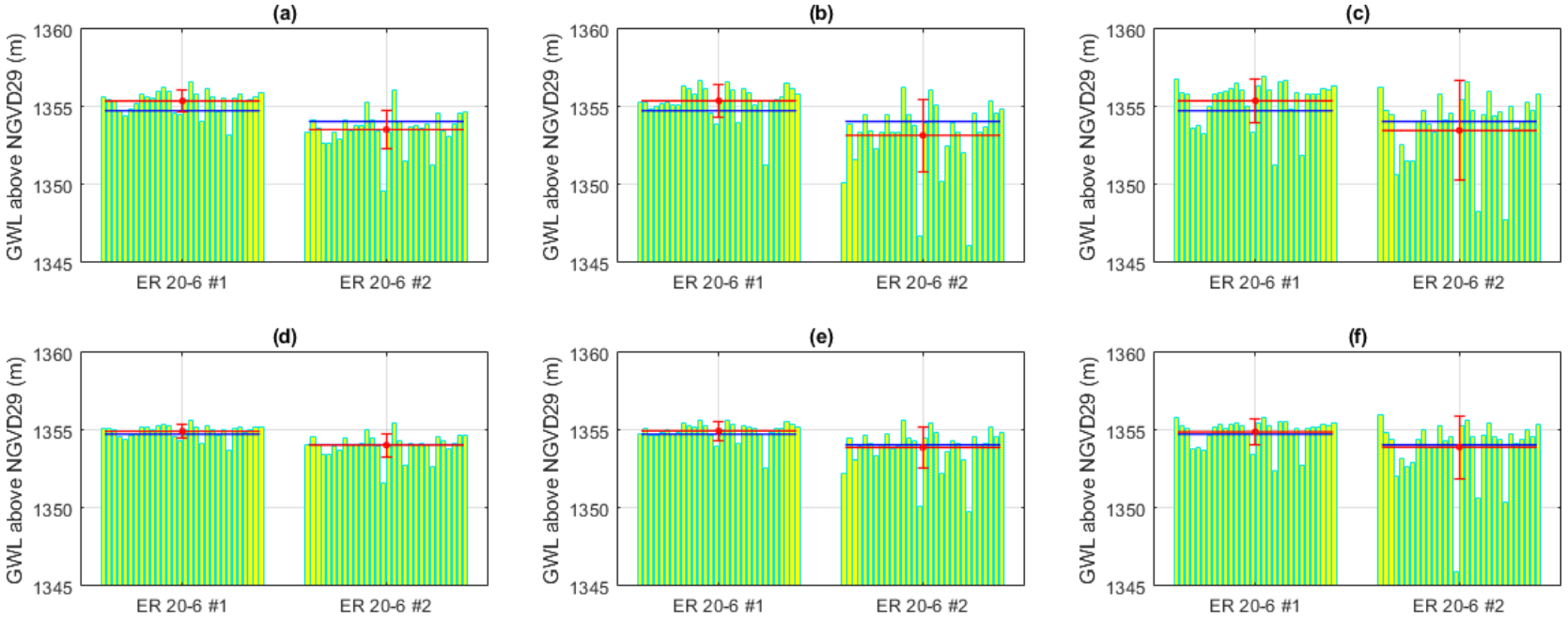

Figure 28. Model calibration results with the optimal model parameters: (a) CFA-BC1, (b) LOG-BC1, (c) LCA-BC1, (d) CFA-BC2, (e) LOG-BC2, and (f) LCA-BC2. Horizontal blue lines represents the observed groundwater level and the red lines represents the mean of the 30 realizations depicted by the yellow bars.

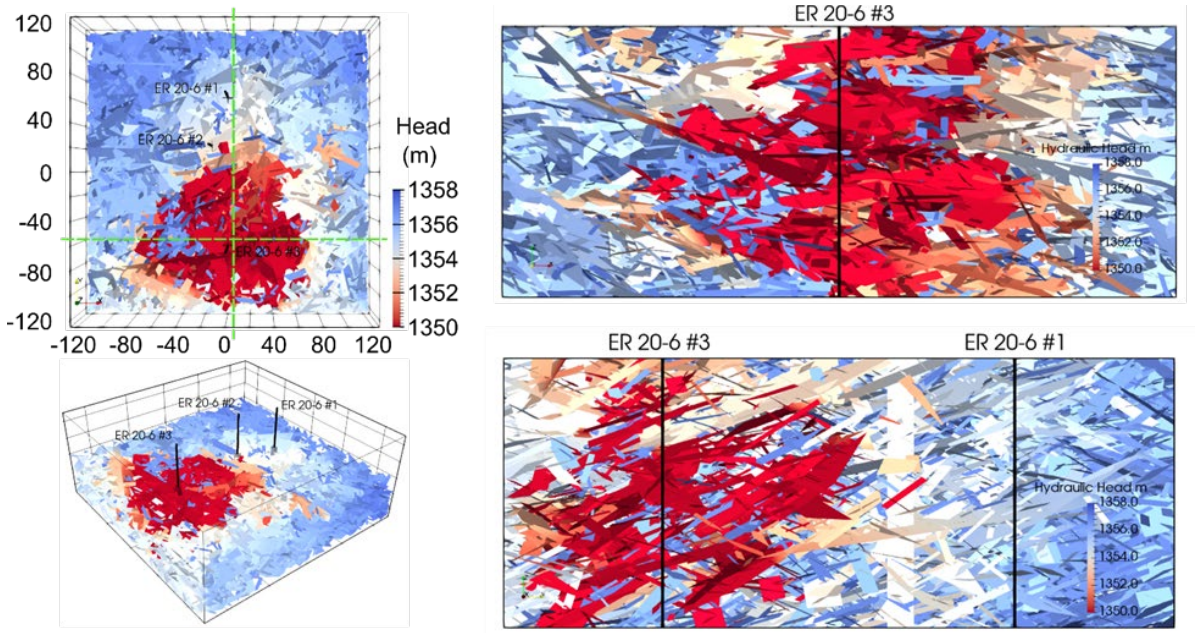

Figure 29. Simulated steady-state groundwater level solution for a calibrated model using the length-correlated fracture apertures.

Impacts of Aperture Distributions

Figure 30 shows the impacts of varying the second parameter of LNA and LCA models on simulated groundwater levels. This is the scale parameter in the context of LNA models and the parameter k in the context of LCA models (see Equation 20). The first parameter estimated during model calibration was fixed. The results showed that varying standard deviations of LNA models led to negligible impacts on simulated groundwater levels. For example, varying standard deviations of fracture apertures from 144.39 microns to 271.81 microns (the first parameter was fixed at −7.7063, which is equal to 487 microns) resulted in MAE variations from 0.18 m to 0.21 m. However, varying the second parameter in LCA models led to measurable impacts on simulated groundwater levels. For example, MAEs increased from 0.50 m to 0.85 m when varying k from 0.35 to 0.45 (which is equal to apertures from 54.67 microns to 80.25 microns).

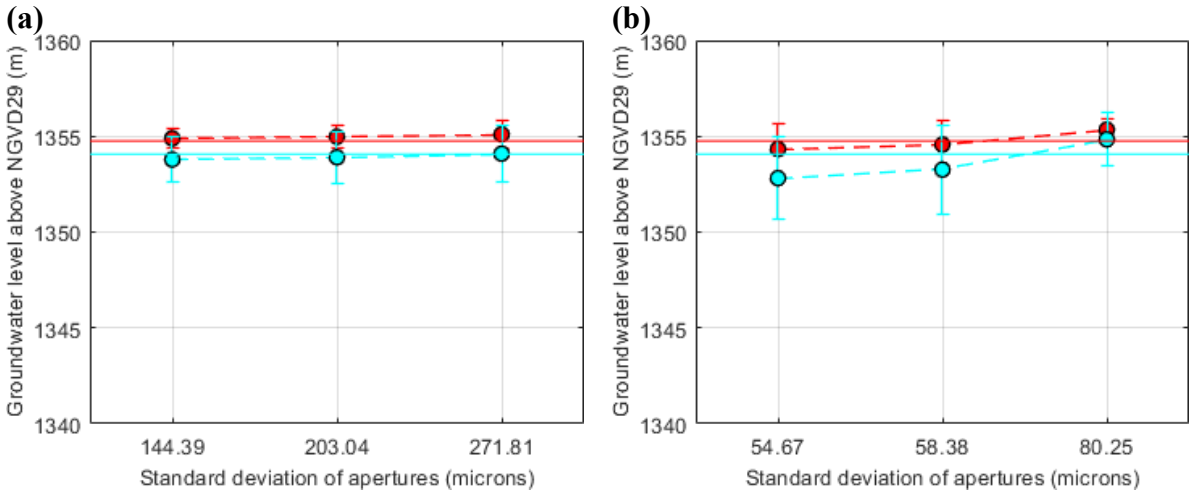

Figure 30. Impact of aperture distributions on simulated groundwater levels for (a) LNA models where standard deviations of fracture apertures were varied from 144.39 microns to 271.81 microns. The mean was fixed at 487 microns; and (b) LCA models where standard deviations of fracture apertures were varied from 54.67 microns to 80.25 microns. The mean was fixed at 241 microns. The solid red line and the solid cyan line show observed groundwater levels at ER 20-6 #1 and ER 20-6 #2, respectively.

Water Flow and Mass Conservation

The pumping well is at the center of the x-axis and the distance from the pumping well to the east and west boundary is 125 m (Figure 22). Figure 31 shows simulated flow from six faces of the model domain using calibrated models with BC2 boundary conditions. Inflows from the east were quite similar to inflows from west for all three models, which shows that the fractures are well connected. High uncertainty was found for simulated flow from east, west, and south. The LNA and LCA models showed higher uncertainty in simulated flow compared with CFA models. Additionally, the results revealed a key difference in simulated inflows and outflows among the three DFN conceptual models. For LCA models, inflows were from east, west, and from south with some probability; whereas inflows were only from east and west for CFA and LNA models.

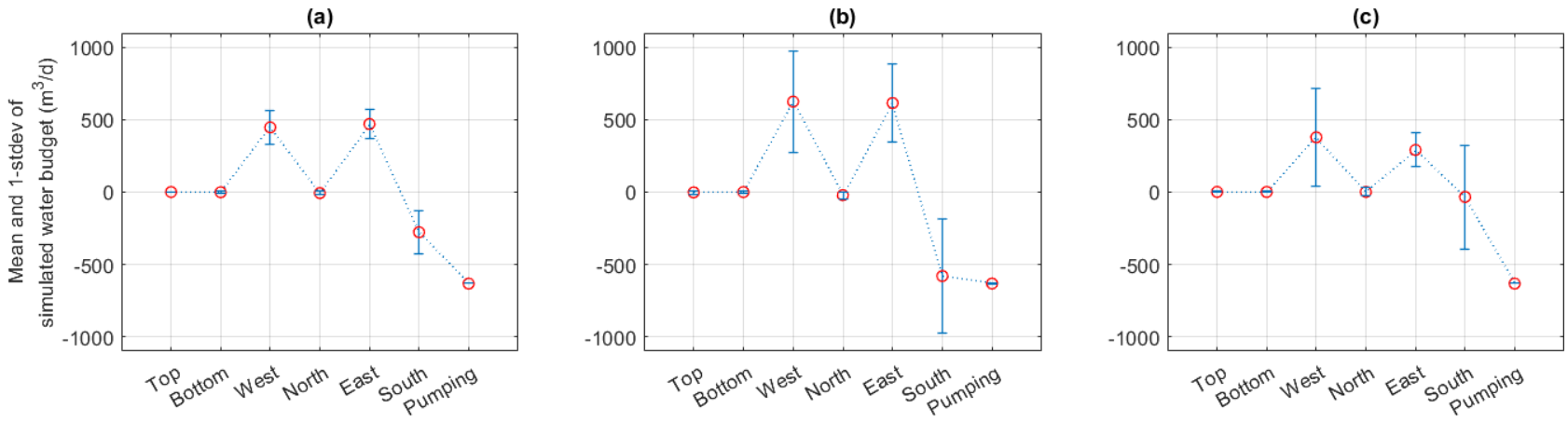

Figure 31. Simulated water inflow and outflow from the model domain: (a) CFA-BC2, (b) LNA-BC2, and (c) LCA-BC2.

Tortuosity and Breakthroughs

We define tortuosity as the actual travel length of particles normalized by the linear distance separating the source and the sink. Figure 32 presents tortuosity when particles were released at well ER 20-6 #1 and collected at well ER 20-6 #3 for 30 DFN realizations. Means of tortuosity varied from 1.53 to 2.48. The average of 30 DFN realizations was 1.89. One standard deviation of tortuosity varied from 0.17 to 0.50. The average of the standard deviation for 30 DFN realizations was 0.28. Figure 33 presents the observed and simulated BTCs at the pumping wells obtained from the three calibrated models under BC2. The results showed that the simulated BTCs did not match the observed BTC. The early arrival times for all six models ranged from 1.9 hours to 11.4 hours. This is significantly different from the observed BTC, for which the early arrival time was 150 hours. The peak of simulated BTCs were several orders of magnitude larger than the observed BTC. The observed deficiency of DFN models to produce site-specific, tracer-test breakthrough data forms the basis of developing a postprocessing methodology to account for matrix diffusion (which is presented in the next section).

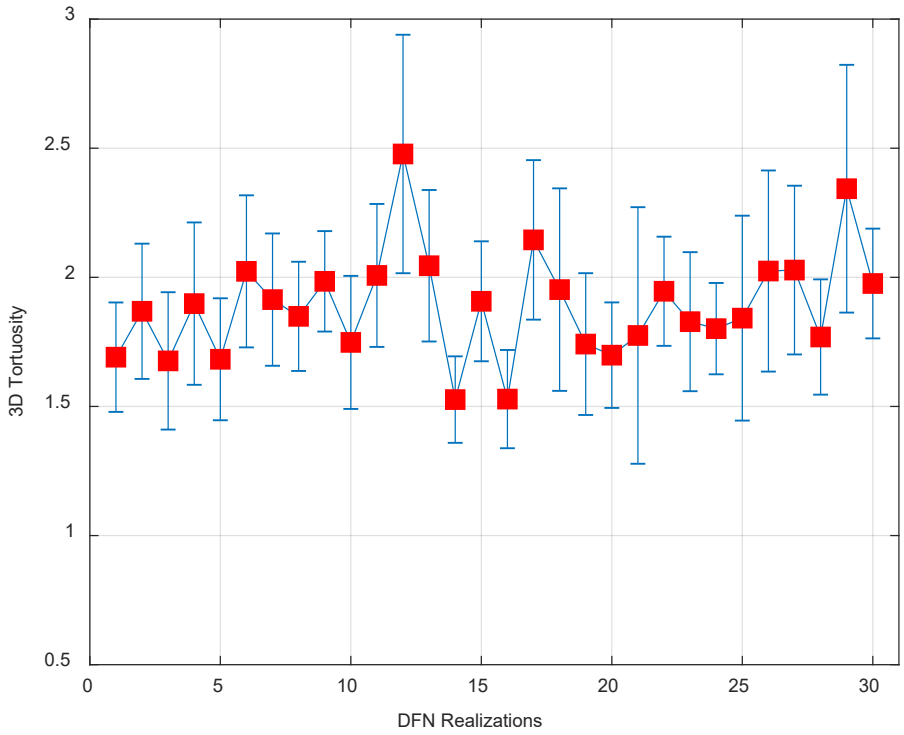

Figure 32. Simulated particle travel lengths from well ER 20-6 #1 to well ER 20-6 #3. The distance between the two wells is 131.4 m.

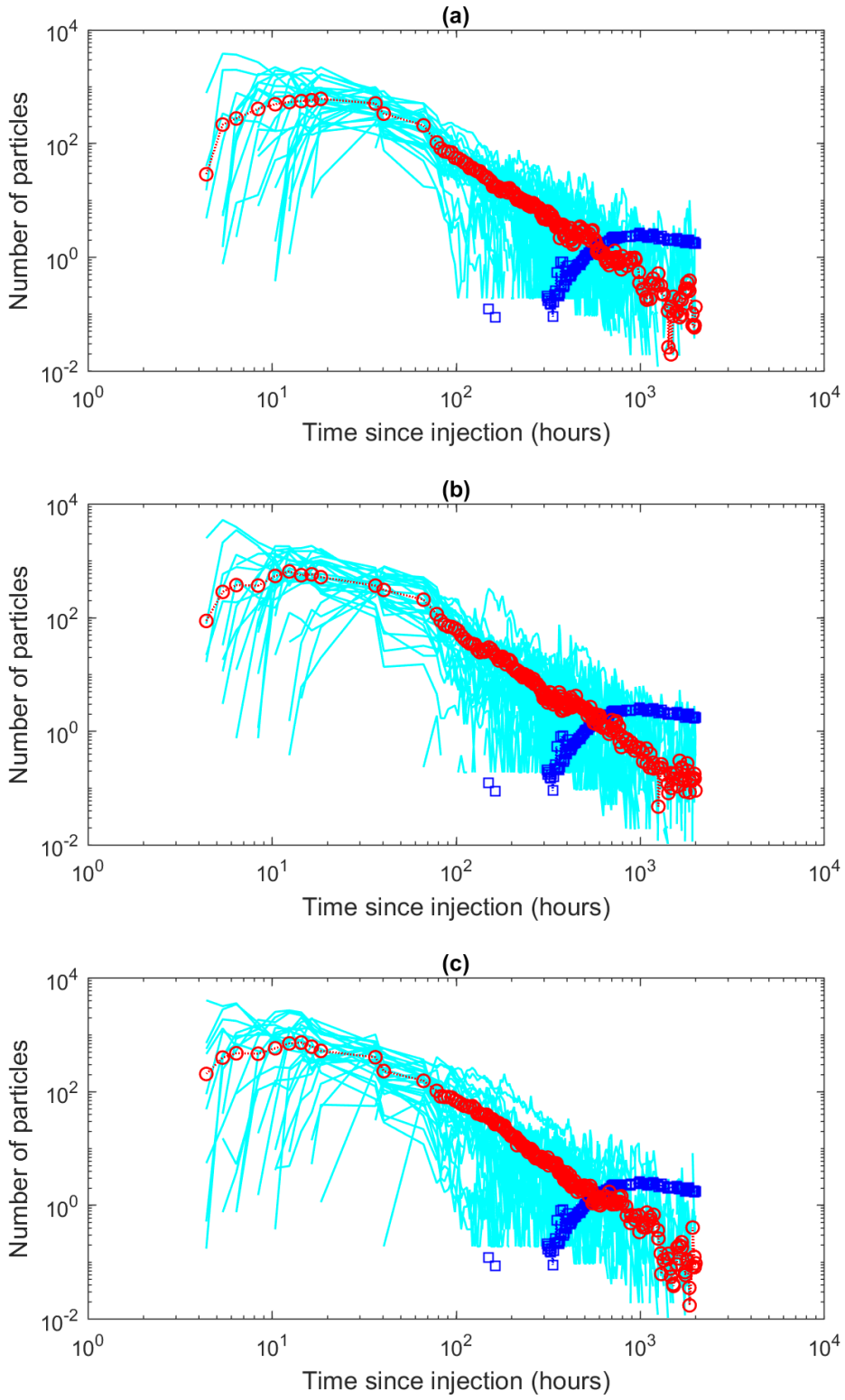

Figure 33. Simulated breakthrough curves for the three calibrated models under BC2 boundary conditions: (a) CFA-BC2, (b) LOG-BC2, and (c) LCA-BC2. Squares (in blue) are for the observed BTC, circles (in red) are the means of simulated BTCs obtained from 30 DFN realizations, and cyan lines are the 30 individual simulated BTCs.

Discussion

Developing a 3-D DFN flow and transport model in a highly fractured rock aquifer, such as the example at the site of the BULLION FGE, was a challenging exercise. Thirty fracture network realizations were generated stochastically using Monte Carlo approaches. Together with the uncertainty in boundary conditions and fracture aperture conceptualizations, this study needed to calibrate and analyze 180 DFN models. Each model run required at least 32 gigabytes (GB) of memory (depending on the number of particles released during transport simulations) and outputted roughly 40 GB of results. The model domain was restricted to 250 m × 250 m in the lateral direction for the BULLION FGE given the high number of models that needed to be calibrated and the availability of computational resources.

Boundary conditions showed significant impacts on simulated groundwater levels and estimated fracture aperture values. Using the BC1 and BC2 boundary conditions with CFA models, the optimal aperture values were estimated at 410 microns and 480 microns, respectively. Similar aperture values were found when using LNA and LCA models. The BC1 boundary conditions were less realistic than the BC2 boundary conditions, which accounts for drawdown at the model boundaries. Because BC2 provided a much better match between the simulated and observed groundwater levels (see Table 5), no more alterations of boundary conditions were considered for this study.

Fracture aperture conceptualizations showed significant impacts on estimated fracture aperture values. The study found two significantly different ranges of fracture apertures using the three fracture aperture models. The CFA and LNA models produced larger apertures (410 microns to 487 microns) and the LCA models produced smaller apertures (208 microns to 241 microns). In the LCA models, fractures with large sizes were assigned large apertures. These fractures then exerted a dominant control on the network because of its large size and aperture. The resulting network was strongly connected and the flow was channelized along a few major features. In contrast, apertures were assigned randomly in LNA models, which potentially created weakly connected networks. Therefore, larger apertures were needed to conduct a similar volume of flow. The approach presented here builds up on mechanistic understanding of flow between fracture walls and avoids the over homogenization and physically unrealistic depiction of fracture networks found in traditional approaches based on representative elementary volume concept.

High uncertainty was found in both the simulated groundwater levels and water balances based on 30 DFN realizations of network. The CFA models resulted in the lowest uncertainty and the LCA models resulted in highest uncertainty. Additionally, computed water balance values were found to be very sensitive to aperture changes in LNA and LCA models, but less sensitive to aperture changes in the CFA model. Multiple sets of model parameters produced good agreement with the observation data. For example, by adjusting apertures, this study found three aperture ranges that matched almost equally well with the observed groundwater levels (Figures 28a, 28b, and 28c). This showed the nonuniqueness of DFN solutions. Additional datasets are needed to discriminate among aperture conceptual models and identify the best choice for a site.

Simulated BTCs did not match well with the observed tracer test data. Simulated arrival times were shorter than the observed arrival time. The simulated recovery rates were higher than the observed recovery rate. The DFN models were designed to only simulate advective transport of particles. The poor match between the BTCs highlights the importance of other transport processes (e.g., dispersion and matrix diffusion) at the BULLION FGE.

CALIBRATION OF 3-D DFNs TO TRANSPORT DATA

As described in the previous section, using dfnWorks to develop a calibrated model for the BULLION FGE succeeded in capturing the trends of the groundwater levels in the observation wells but failed at matching the breakthrough curves of tracers arriving at the pumping well (see Figure 33). This poor match between simulated and observed BTCs was mainly attributed to the absence of capabilities in a DFN model to simulate transport processes other than advection through a connected set of fractures. The purpose of this section is to account for neglected transport processes in advection-only transport simulations by postprocessing the breakthrough curves. In this case, the neglected processes were diffusive. Solute diffuses in all directions throughout the field test, but does not diffuse in the DFN transport simulations. Mathematically, this manifests itself in two ways. In the direction longitudinal to the predominant flow, normal to plane where the breakthrough curve is measured, travel times to arrive at the plane are modified by dispersion. In the transverse directions, the travel times are modified by diffusion into the rock matrix.

To account for dispersion, a kernel method was used to smooth the breakthrough curve, using the dispersion length scale as the bandwidth of the kernel. The contribution of each particle to the mass in the breakthrough curve was spread out using the kernel method, which is discussed in the following section. To account for matrix diffusion, a mobile-immobile model is used. Of all the nonlocal-in-time random walk models, the mobile-immobile model stands out because it leaves the physical meaning of the parameters of the spatial operator intact (i.e., the model is based on the premise that total concentration splits into mobile and immobile components, which interchange locally). The rock matrix was envisioned to be completely immobile (no flow) and infinite in extent. This led to the use of a fractional mobile-immobile model, which is discussed in the "Matrix Diffusion" section.

Dispersion

A kernel method, that is use of a functional tool to transform the concentrations into a new output, was used to distribute the mass of solute particles across time according to dispersion. Let there be n_p particles, each with mass m_p. To calculate the breakthrough curve in the absence of the kernel, the contribution of this mass was distributed according to a delta distribution:

$$C(t) = \sum_{i=1}^{n_p} m_p \delta(t - t_i), \tag{22}$$

where t_i is the arrival time at the breakthrough plane of particle i. If the particle were to disperse, its arrival time would be uncertain. Dispersion was assumed to follow Fick's law and was modeled using a normal distribution. Therefore, the random walk of the particle is:

$$\Delta x = v\Delta t + \sqrt{2D\Delta t}\xi \tag{23}$$

where v is the particle's average velocity, D is the dispersion coefficient, and ξ is a random variable distributed according to a standard normal distribution (with mean 0 and variance 1). For this case, $D = \alpha v$, where the dispersivity, α, comes from the field test report (Reimus and Haga, 1999).

The parameters Δx (the distance to the breakthrough plane) and Δt (the arrival time) were known from the advection-only random walk on a discrete fracture network:

$$\Delta x = v\Delta t, \tag{24}$$

and were used to find v (the average velocity). It was assumed that this average velocity was unaffected by the process of dispersion. To find the uncertainty in the breakthrough time of the particle, a random variable τ was inserted into the random walk equation:

$$\Delta x = v(\Delta t - \tau) + \sqrt{2D(\Delta t - \tau)}\xi. \tag{25}$$

To find the distribution of τ, the above equation was reduced such that τ could explicitly be determined. The advective contribution was assumed to dominate the dispersive contribution, that is:

$$v(\Delta t - \tau) \gg \sqrt{2D(\Delta t - \tau)}\xi. \tag{26}$$

Therefore, the contribution of τ to the dispersive jump was neglected, and we have:

$$\Delta x = v(\Delta t - \tau) + \sqrt{2D\Delta t}\xi, \tag{27}$$

which can be rearranged to obtain:

$$\tau = \Delta t - \frac{\Delta x}{v} + \frac{\sqrt{2D\Delta t}\xi}{v} = \frac{\sqrt{2D\Delta t}}{v}\xi. \tag{28}$$

Substituting for D and v, we find:

$$\tau = \sqrt{\frac{2\alpha\Delta t^2}{\Delta x}}\xi \tag{29}$$

and therefore τ is distributed according to a normal distribution with mean 0 and variance $\frac{2\alpha\Delta t^2}{\Delta x}$. The concentration can then be calculated according to:

$$C(t) = \sum_{i=1}^{n_p} \frac{m_p}{\sigma_i\sqrt{2\pi}} \exp\left(-\left(\frac{t - t_i}{\sigma_i\sqrt{2}}\right)^2\right), \tag{30}$$

where $\sigma_i = \sqrt{\frac{2\alpha(t-t_i)^2}{\Delta x}}$.

Matrix Diffusion

A fractional mobile-immobile model was used to account for solute diffusion into and out of the rock matrix. It was assumed that solute that enters the rock matrix experiences no transport. In the absence of matrix diffusion, the governing equation for concentration of the solute is:

$$\frac{d}{dt}C = AC \tag{31}$$

where A is the spatial operator governing transport (advection and dispersion in this case). In the mobile-immobile model, the concentration was split into mobile and immobile phases, where the total concentration was the sum of the mobile and immobile concentrations:

$$C_{tot} = \theta_m C_m + \theta_{im} C_{im} \tag{32}$$

The total concentration followed the same conservation equation, which is also the case with no matrix diffusion:

$$\frac{d}{dt}C_{tot} = AC_m \tag{33}$$

except that transport only occurs for the mobile concentration, C_m. Using the relationship between the concentration phases (Eq. 32), we find:

$$\frac{d}{dt}C_m + \frac{d}{dt}C_{im} = AC_m \tag{34}$$

The immobile concentration is further related to the mobile concentration by convolution with a memory kernel:

$$C_{im} = k * C_m \tag{35}$$

The memory kernel, *k*, encodes the rate of entry into and the distribution of exit times out of the immobile zone (rock matrix) and can be any monotonically decreasing function. The key modeling choice is the choice of the memory kernel, discussed below.

Once k is chosen, the equation for total concentration (Equation 34) is transformed into the Laplace domain:

$$s\widehat{C_m} + s\hat{k}\widehat{C_m} + C_0 = A\widehat{C_m} \tag{36}$$

where s is the Laplace variable, the hats signify transformed functions, and C_0 is the initial concentration. The solution is:

$$\widehat{C_m} = \frac{-C_0}{s(1+\hat{k}) - A} \tag{37}$$

Notice that the solution for concentration in the absence of matrix diffusion (Equation 31) is:

$$\hat{C} = \frac{-C_0}{s - A}, \tag{38}$$

Therefore to account for diffusion, we shifted the Laplace variable by $s\hat{k}$. Therefore, the breakthrough curve was numerically transformed into Laplace space with the Laplace variable $s(1 + \hat{k})$ and the inverse transform was performed to find the breakthrough curve, which accounts for matrix diffusion.

For this study, the fractional case considered in Schumer *et al.* (2003) was assumed to model the memory kernel as:

$$k = \frac{\beta t^{-\gamma}}{\Gamma(1 - \gamma)}, \tag{39}$$

where $\beta > 0$ and $0 < \gamma \leq 1$ are constants and represent the ratio of porosity in the immobile and mobile zones, and the rate of mass transfer between mobile and immobile zones (when the memory function follows a power law), respectively. These two parameters are used in this study as curve fitting parameters to improve the match between observed and simulated breakthroughs. The term Γ denotes the Gamma function. In this case, $\frac{d}{dt}(k * C_m)$ is a fractional Riemann-Liouville derivative. Other commonly used cases are listed in Haggerty *et al.* (2000) (see Table 1 $g(t)$ column) and in Ginn *et al.* (2017) (see Table 1 $g(t)$ column times β).

Metrics to Assess Model Error

Using the best-fit values for β and γ corresponding to the aperture distributions, the error in breakthrough was calculated over the time range $[t_{min}\ t_{max}]$, where t_{min} is the first point in time when solute was extracted in the pumping well (in the BULLION FGE) and t_{max} is the point in time when the pumping test ended. A vector of times in this range was created with 1000 log spaced times to calculate breakthrough and error. At each of these times, the breakthrough of the ensemble of the simulations ($C_{pred}(t)$) and of the field test ($C_{act}(t)$) are calculated.

The absolute error at that time is calculated at each time, t_j:

$$E(t_j) = \left|C_{pred}(t_j) - C_{act}(t_j)\right| \tag{40}$$

then summed and normalized to produce the breakthrough absolute relative error ($BARE$):

$$BARE = \frac{\sum_j E(t_j)}{\sum_j C_{act}(t_j)} \tag{41}$$

The head error, *HE*, is the absolute difference between the observed and the simulated head values computed using the dfnWorks model presented in the "Calibration of 3-D DFNs

to Flow Data" section. Weighted error, WE, was calculated as the geometric mean of the $BARE$ and the HE:

$$WE = \sqrt{(BARE)(HE)} \tag{42}$$

Table 6 summarizes the best-fit values for various aperture models presented in the "Calibration of 3-D DFNs to Flow Data" section and the corresponding error metrics.

Table 6. Best-fit values for the parameters of the memory kernel and the error metrics for various aperture distribution models under BC1 and BC2.

BC	Distribution	1st parameter	2nd parameter	β	γ	$BARE$	HE	WE
1	CFA	410	~	10.2	.72	.1536	.57	.296
2	CFA	480	~	9.1	.81	.1617	.10	.127
1	LNA	380	0.1	10.2	.72	.2090	.80	.409
1	LNA	380	0.3	10.2	.72	.1291	.78	.317
1	LNA	380	0.4	10.2	.72	.1199	.80	.310
2	LNA	450	0.3	9.1	.81	.1769	.21	.193
2	LNA	450	0.4	9.1	.81	.1478	.21	.176
2	LNA	450	0.5	9.1	.81	.1748	.18	.177
1	LCA	1.1	0.3	10.2	.72	.2156	4.46	.981
1	LCA	1.1	0.4	10.2	.72	.2186	.63	.371
1	LCA	1.1	0.5	10.2	.72	.2168	1.67	.602
2	LCA	1.275	0.35	9.1	.81	.4331	.93	.635
2	LCA	1.275	0.4	9.1	.81	.2842	.15	.207
2	LCA	1.275	0.45	9.1	.81	.2764	.65	.424

Results

To use the postprocessing technique, the two parameters for the fractional kernel (β and γ) were found by curve fitting. The parameters were fitted from the breakthrough curves corresponding to the CFA model for each boundary condition. Figures 34a and 34b show the original breakthrough curve from dfnWorks for delta distributed aperture for each boundary condition (BC1 and BC2), which consistently predicts early arrivals. Also shown on each figure is the best-fit breakthrough curve after postprocessing, which is a significantly closer match to the field data. Table 6 shows the values of the parameters used in these simulations.

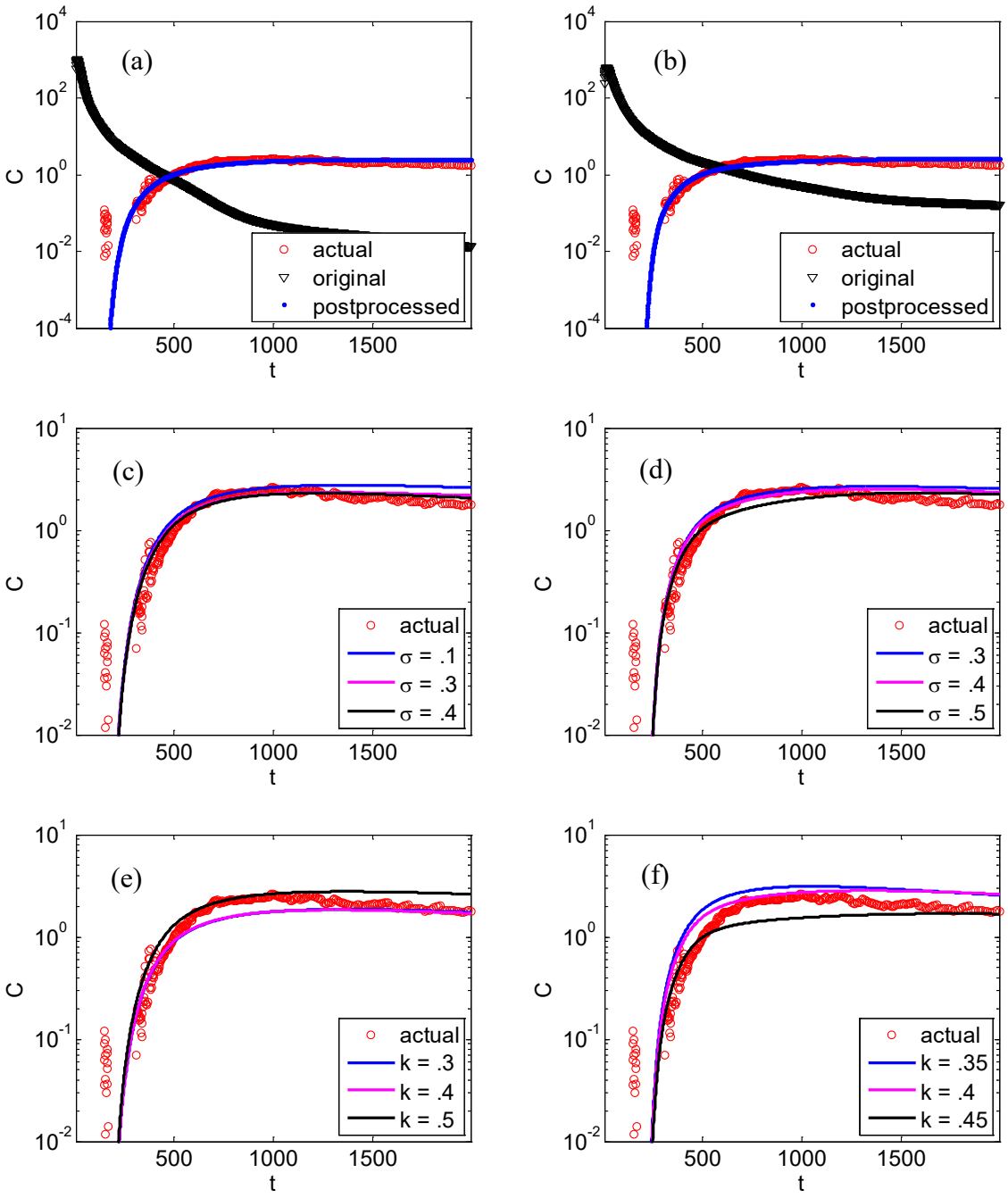

Figure 34. Comparison between observed breakthrough curve (actual) and postprocessed breakthrough curve for: (a) CFA model using BC1, (b) CFA model using BC2, (c) LNA model using BC1, (d) LNA model using BC2, (e) LCA model using BC1, and (f) LCA model using BC2. The CFA model results ([a] and [b]) also show the original (unprocessed) simulated breakthrough curves.

Figure 34c shows the postprocessed breakthrough curves for the LNA for various values of standard deviation (σ) using BC1. In this case, considering the error in head alone, it would be assumed that $\sigma = 0.3$ was closest to the standard deviation of the actual aperture distribution, even though all three choices have similar errors. However, the error in the breakthrough curve with $\sigma = 0.4$ was the lowest. Figure 34d is the same as Figure 34c, but for BC2. In this case, the lowest head error was for $\sigma = 0.5$ and the lowest breakthrough error was for $\sigma = 0.4$. By weighing the errors, the lowest error for $\sigma = 0.4$ was found for both cases.

Figure 34e shows the postprocessed breakthrough curves for the LCA distributions for various values of the constant k (see Equation 20) using BC1. In this case, considering the error in head alone, it would be assumed that $k = 0.4$ was closest to the parameter of the actual aperture distribution. However, the error in the breakthrough curve with $k = 0.3$ was the lowest, even though all three choices had similar errors. Figures 34f and 34e are the same, except for BC2. In this case, the lowest head error was for $k = 0.4$ and the lowest breakthrough error was for $k = 0.45$. By weighing the errors, the lowest error for $k = 0.4$ was found for both cases.

Discussion

By accounting for errors in both simulated hydraulic head and in postprocessed breakthrough curves, which accounted for diffusive processes, it was predicted that if the aperture distribution was lognormal, then $\sigma = 0.4$, and if the distribution was length correlated, then $k = 0.4$. Furthermore, when comparing errors between aperture distributions, the lognormal distribution was more likely to perform better than the length-correlated distribution. Finally, the weighted error in the CFA distributions was lower than the corresponding lognormal distributions (for both BCs). Although CFA breakthrough curves were used to fit the parameters of the fractional kernel in the postprocessor, this alone did not explain the lower errors because breakthrough errors were actually higher for the CFA models than the corresponding LNA models.

The work presented in this section in conjunction with the flow calibration work presented in the "Calibration of 3-D DFNs to Flow Data" section establishes a method to develop calibrated models for fractured rock aquifers. These models are highly useful because they allow fracture aperture uncertainty to be reduced, which in turn helps to more accurately describe groundwater flow and transport. The flow calibration part alone ("Calibration of 3-D DFNs to Flow Data") narrows down the choices of aperture distribution model and aperture ranges, but it does not provide a unique solution. Using the set of solutions obtained from the flow calibration, transport calibration was performed via postprocessing techniques (as described in this section), which helped to develop a high degree of confidence for specific aperture distributions and ranges of values.

SUMMARY AND CONCLUSIONS

Discrete fracture network modeling approaches were used to study techniques for upscaling transport in fractured rocks and to develop model calibrated to observed hydraulic head and transport data using fracture aperture as a calibration tool. The upscaling study was based on solutions obtained from 2-D DFN models (Parashar and Reeves, 2012). The flow and transport calibration part of the project was based on solutions obtained from dfnWorks,

a state-of-art, 3-D DFN simulator developed at the Los Alamos National Laboratory (Hyman *et al.*, 2015a). Field data for the calibration study was obtained from the BULLION FGE, a tracer test experiment conducted over a span of 87 days in the summer of 1997 on Pahute Mesa in Area 20 of the NNSS (IT Corporation, 1998).

An extensive model development exercise was undertaken to create a well package for dfnWorks. This well package was easy to implement in dfnWorks and was tested for accuracy against solutions obtained from examples in MODFLOW. The method modified three source code files, so a user would need to modify these files before compiling dfnWorks. The recompiling process was the same as the original dfnWorks. Two new parameters were introduced: a well skin radius and well skin permeability. Two examples of simple deterministic fracture networks and one example of a complex stochastic fracture network were constructed to test the functioning of dfnWorks with an integrated well package, as well as to test the influence of the new well parameters on flow and transport. The results of the three examples revealed that the method enhanced the connectivity between a well and fracture backbones, as well as simulated the physical process of flow and transport along and around the wells in DFNs. It was found that:

1) The radius and permeability of well skin at an injection well had significant effects on simulated BTCs. Ideally, the radius of injection well skin could be determined using observed one-dimensional fracture intensity P_{10}. If there were no available data on fracture intensity, the well skin parameters could be treated as adjustable model parameters to help produce a close match to field observations.
2) The skin radius and skin permeability of a pumping well showed negligible effect on the BTCs. One could increase the pumping well skin radii to strengthen connection between the pumping well and backbone to reduce numerical issues.

The random walk method provided a framework for modeling non-Fickian transport through fracture networks by using probability distributions to generate particle jump lengths and residence times spanning multiple orders of magnitude. Examples of random walk upscaling methods used in this study are: Markov directed random walk (MDRW), Monte Carlo solution of the Boltzmann transport equation (BTE), and the spatial Markov model (SMM). We focused specifically on random walk models to determine what aspects of the space and time step distributions (e.g., correlation and coupling) must be accounted for to get the most accurate predictions of transport in a 2-D fracture network. The solution obtained from a 2-D DFN model was treated as the ground truth, and the random-walk-based upscaling methods were evaluated for their performance under varying scenarios. By comparing scenarios with different fracture transmissivity distributions (with $\sigma = 0, .5, 1$), upscaling models, and modeling step definitions, we noted the following major highlights:

1) As the distribution of fracture transmissivity widened, preferential pathways for solute formed, creating correlation in particle velocities over successive steps. For the lognormal transmissivity distributions, models that incorporate correlation gained an advantage over their uncorrelated counterparts when $\sigma = 1$.

2) Early breakthrough was best predicted by the uncorrelated models (uMDRW and uSMM) for $\sigma < 1$ and by the correlated models (MDRW, BTE, SMM) for $\sigma = 1$.

3) Tailing behavior was best predicted by the SMM models (uSMM, SMM) for $\sigma < 1$ and by the correlated BTE model for $\sigma = 1$.

4) Comparing the effects of model choice and correlation showed that the effect of modeling scale (number of fracture segments used to define modeling steps) on model predictive performance was negligible, at least over the range (~ 1 km) covered in this study.

For each DFN realization of the 2-D network, upscaled simulations for six different models (MDRW, uMDRW, BTE, uBTE, SMM, and uSMM) at three different length scales were conducted. The uBTE performed the poorest, and all three length scales gave similar predictions. For future research, more than two-thirds of the model runs can be eliminated by excluding uBTE and the two smaller length scales for all models, leaving just five models and one length scale, which will allow us to assess the effect of varying DFN parameters other than transmissivity distribution and to expand the model to 3-D.

For the site-specific calibration part of the project, DFN models were developed using dfnWorks and calibrated to drawdowns obtained from the BULLION FGE. Fracture aperture was used as a calibration parameter. Thirty DFN realizations of fracture network, three conceptual models of fracture apertures, and two sets of boundary conditions were considered in model calibration and in uncertainty quantification. The results showed that fracture network structures, fracture aperture conceptualization, and the boundary conditions had significant impacts on the estimated values of fracture apertures and simulated groundwater levels and water budgets. It was found that the boundary conditions in a DFN model needed to be adequately adjusted when a pumping well was included.

Constant fracture aperture models showed the least uncertainty in simulated groundwater levels and water budgets and were a good starting point for developing calibrated 3-D DFN models. Model calibration found optimal fracture apertures at the BULLION site ranging from 241±65 microns to 487±203 depending on the conceptual model selected for the fracture apertures. The estimated apertures could be used to compute the equivalent permeability of fractured rock masses.

Although the flow calibration exercise in a DFN modeling framework led to a fairly constrained range of aperture values, the solution was not completely unique. More than one model conceptualization and magnitude of fracture apertures could give rise to similar matches with the field-observed values of hydraulic drawdowns. The simulated BTCs by dfnWorks were also not in good agreement with the observed tracer test data because the DFN models were designed to simulate only advective transport through the connected sets of fractures in a network. To include the influence of longitudinal dispersion and matrix diffusion in breakthrough responses, a set of postprocessing methods were developed to numerically transform the BTC data. The postprocessor was based on a memory kernel method that relies on two parameters. The best-fit parameters resulted in a good match of the simulated BTC with the observed BTC. This also allowed to the aperture ranges to be further constrained, and therefore it greatly reduced the uncertainty present in the model prior to application of the postprocessor. The latest version of dfnWorks has incorporated a Time

Domain Random Walk (TDRW) methodology to provide correction to a particle's travel time because of matrix diffusion. In TDRW, the time a particle spends in a fracture, T, is found as the sum of advective time and a time related to diffusion process between fracture and matrix. In future studies, it will be worthwhile to compare the results from TDRW based simulations to results of the post-processing techniques presented in this report.

The work presented in this report is expected to constrain fracture aperture values in Pahute Mesa to realistic ranges, inform and support other flow and transport models in the Corrective Action Unit, help understand the key transport trends that are manifested in fractured aquifer units, and provide ways to effectively upscale transport for potential integration to large-scale models.

REFERENCES

Abbaspour, K.C., R. Schulin, and M.Th. van Genuchten, 2001. Estimating unsaturated soil hydraulic parameters using ant colony optimization. *Advances in Water Resources* 24:827–841. doi: 10.1016/S0309-1708(01)00018-5

Barbier, E., 2002. Geothermal energy technology and current status: An overview. *Renewable and Sustainable Energy Reviews* 6:3–65. doi: 10.1016/S1364-0321(02)00002-3

Bear, J., 1988. *Dynamics of Fluids in Porous Media*. Courier Dover Publications.

Bennett, G.D., A.L. Kontis, S.P. Larson, 1982. Representation of Multiaquifer Well Effects in Three-Dimensional Ground-Water Flow Simulation. *Groundwater* 20:334–341. doi: 10.1111/j.1745-6584.1982.tb01354.x

Berkowitz, B., 2002. Characterizing flow and transport in fractured geological media: A review. *Advances in Water Resources* 25 (8) 861–884.

Benke, R., and S. Painter, 2003. Modeling conservative tracer transport in fracture networks with a hybrid approach based on the Boltzmann transport equation. *Water Resources Research* 39 (11) SBH 6–1–11.

Berkowitz, B., A. Cortis, M. Dentz, and H. Scher, 2006. Modeling non-Fickian transport in geological formations as a continuous time random walk. *Reviews of Geophysics* 44 (2) 1-49.

Berkowitz, B., and H. Scher, 1997. Anomalous transport in random fracture networks. *Physical Review Letters* 79 (20) 4038.

Berkowitz, B., and H. Scher, 1998. Theory of anomalous chemical transport in random fracture networks. *Physical Review E* 57 (5) 5858.

Berrone, S., C. Canuto, S. Pieraccini, and S. Scialò, 2018. Uncertainty Quantification in Discrete Fracture Network Models: Stochastic Geometry. *Water Resources Research* 0, https://doi.org/10.1002/2017WR021163.

Bodvarsson, G.S., W. Boyle, R. Patterson, and D. Williams, 1999. Overview of scientific investigations at Yucca Mountain—the potential repository for high-level nuclear

waste. *Journal of Contaminant Hydrology* 38:3–24. doi: 10.1016/S0169-7722(99)00009-1.

Bogdanov, I.I., V.V. Mourzenko, J.-F. Thovert, and P.M. Adler, 2002. Pressure drawdown well tests in fractured porous media. *Water Resources Research* 39, https://doi.org/10.1029/2000WR000080.

Bolster D, Y. M´eheust, T.L. Borgne, J. Bouquain, and P. Davy, 2014. Modeling preasymptotic transport in flows with significant inertial and trapping effects: The importance of velocity correlations and a spatial Markov model. *Advances in Water Resources* 70 (0) 89-103.

E. Bonnet, O. Bour, N.E. Odling, P. Davy, I. Main, P. Cowie, and B. Berkowitz, 2001. Scaling of fracture systems in geological media. *Reviews of Geophysics* 39 (3) 347–383.

Brunner, P., and C.T. Simmons, 2012. HydroGeoSphere: A Fully Integrated, Physically Based Hydrological Model. *Ground Water* 50:170–176. doi: 10.1111/j.1745-6584.2011.00882.x.

Cacas, M.C., E. Ledoux, G. de Marsily, A. Barbreau, P. Calmels, B. Gaillard, and R. Margritta, 1990a. Modeling fracture flow with a stochastic discrete fracture network: Calibration and validation: 2. The transport model. *Water Resources Research* 26, 491–500. https://doi.org/10.1029/WR026i003p00491.

Cacas, M.C., E. Ledoux, G. de Marsily, B. Tillie, A. Barbreau, E. Durand, B. Feuga, and P. Peaudecerf, 1990b. Modeling fracture flow with a stochastic discrete fracture network: calibration and validation: 1. The flow model. *Water Resources Research* 26, 479–489. https://doi.org/10.1029/WR026i003p00479.

Cooley, R.L., 1985. A Comparison of Several Methods of Solving Nonlinear Regression Groundwater Flow Problems. *Water Resources Research* 21:1525–1538. doi: 10.1029/WR021i010p01525.

Cortis, A., and B. Berkowitz, 2005. Computing “anomalous” contaminant transport in porous media: The CTRW MATLAB toolbox. *Ground Water* 43 (6) 947–950.

Council, N.R., 1996. *Rock Fractures and Fluid Flow: Contemporary understanding and applications*. National Academies Press.

Cvetkovic, V., S. Painter, N. Outters, and J.O. Selroos, 2004. Stochastic simulation of radionuclide migration in discretely fractured rock near the Äspö Hard Rock Laboratory. *Water Resources Research* 40, W02404. https://doi.org/10.1029/2003WR002655.

Davy, P., 1993. On the frequency-length distribution of the San Andreas fault system. *Journal of Geophysical Research: Solid Earth* 98 (B7) (1993) 12141–12151.

de Dreuzy, J.-R., Y. Méheust, and G. Pichot, 2012. Influence of fracture scale heterogeneity on the flow properties of three-dimensional discrete fracture networks (DFN). *Journal of Geophysical Research: Solid Earth* 117:B11207. doi: 10.1029/2012JB009461.

Dershowitz, W.S., G. Lee, J. Geier, S. Hitchcock, and P. La Pointe, 1993. FracMan user documentation. Golder Associates, Inc., Seattle.

Doherty, J., 2015. *Calibration and Uncertainty Analysis for Complex Environmental Models*. Watermark Numerical Computing, Brisbane, Australia.

Doherty, J., L. Brebber, and P. Whyte, 1994. PEST: Model-independent Parameter Estimation. Watermark Computing, Corinda, Australia, p. 122.

Drellack, S. L., L. B. Prothro, K. E. Robersom, B. A. Schler, and E. H. Price, 1997. Analysis of fractures in volcanic cores from Pahute Mesa, Nevada Tests site, DOE/NV/11718-160

El Harrouni, K., D. Ouazar, G.A. Walters, and A.H.-D. Cheng, 1996. Groundwater optimization and parameter estimation by genetic algorithm and dual reciprocity boundary element method. *Engineering Analysis with Bound Elements* 18:287-296. doi: 10.1016/S0955-7997(96)00037-9.

Elshall, A.S., H.V. Pham, F.T.-C. Tsai, L. Yan, and M. Ye, 2015. Parallel inverse modeling and uncertainty quantification for computationally demanding groundwater-flow models using covariance matrix adaptation. *Journal of Hydrologic Engineering* 20, 04014087. https://doi.org/10.1061/(ASCE)HE.1943-5584.0001126.

Erhel, J., J. de Dreuzy, and B. Poirriez, 2009. Flow Simulation in Three-Dimensional Discrete Fracture Networks. *SIAM Journal on Scientific Computing* 31:2688–2705. doi: 10.1137/080729244.

Fenelon, J. M., Sweetkind D.S., Laczniak R. J., 2010, Groundwater flow systems at the Nevada Test Site, Nevada: A synthesis of potentiometric contours, hydrostratigraphy, and geologic structures: U.S. Geological Survey Professional Paper 1771, p. 54, 6pls.

Fienen, M.N., C.T. Muffels, and R.J. Hunt, 2009. On Constraining Pilot Point Calibration with Regularization in PEST. *Ground Water* 47:835–844. doi: 10.1111/j.1745-6584.2009.00579.x.

Geldon, A.L., 2004. Hydraulic Tests of Miocene Volcanic Rocks at Yucca Mountain and Pahute Mesa and Implications for Groundwater Flow in the Southwest Nevada Volcanic Field, Nevada and California. Geological Society of America, Boulder, Colorado.

Gill, M.K., Y.H. Kaheil, A. Khalil, N. McKee, and L. Bastidas, 2006. Multiobjective particle swarm optimization for parameter estimation in hydrology. *Water Resources Research* 42:W07417. doi: 10.1029/2005WR004528.

Ginn, T.R., L.G. Schreyer, and K. Zamani, 2017. Phase exposure-dependent exchange. *Water Resources Research*, *53*(1), 619-632.

Hadgu, T., S. Karra, E. Kalinina, N. Makedonska, J.D. Hyman, K. Klise, H.S. Viswanathan, and Y. Wang, 2017. A comparative study of discrete fracture network and equivalent continuum models for simulating flow and transport in the far field of a hypothetical nuclear waste repository in crystalline host rock. *Journal of Hydrology* 553:59–70. doi: 10.1016/j.jhydrol.2017.07.046.

Haggerty, R., S.A. McKenna, and L.C. Meigs, 2000. On the late-time behavior of tracer test breakthrough curves. *Water Resources Research*, *36*(12), 3467-3479.

Harbaugh, A.W., 2005. MODFLOW-2005, The U.S. Geological Survey Modular Ground-Water Model - the Ground-Water Flow Process. In: Book 6. Modeling techniques, Section A. Ground Water. U.S. Department of the Interior, U.S. Geological Survey, Virginia, p. 253.

Hammond, G.E., P.C. Lichtner, C. Lu, and R.T. Mills, 2012. PFLOTRAN: Reactive flow & transport code for use on laptops to leadership-class supercomputers. Zhang Al31 pp. 141-159.

Hammond, G.E., P.C. Lichtner, and R.T. Mills, 2014. Evaluating the performance of parallel subsurface simulators: An illustrative example with PFLOTRAN. *Water Resources Research* 50, 208-228. https://doi.org/10.1002/2012WR013483.

Hendricks Franssen, H.J., A. Alcolea, M. Riva, M. Bakr, N. van der Wiel, F. Stauffer, and A. Guadagmini, 2009. A comparison of seven methods for the inverse modelling of groundwater flow. Application to the characterization of well catchments. *Advances in Water Resources* 32:851-872. doi: 10.1016/j.advwatres.2009.02.011.

Hill, M.C., and C.R. Tiedeman, 2007. Effective Groundwater Model Calibration: With Analysis of Data, Sensitivities, Predictions, and Uncertainty, 1st edn. Wiley-Interscience.

Hunt, R.J., J. Doherty, and M.J. Tonkin, 2007. Are Models Too Simple? Arguments for Increased Parameterization. *Ground Water* 45:254–262. doi: 10.1111/j.1745-6584.2007.00316.x.

Hyman, J., C. Gable, and S. Painter, and N. Makedonska, 2014. Conforming Delaunay Triangulation of Stochastically Generated Three Dimensional Discrete Fracture Networks: A Feature Rejection Algorithm for Meshing Strategy. *SIAM Journal on Scientific Computing* 36:A1871–A1894. doi: 10.1137/130942541.

Hyman, J.D., S. Karra, N. Makedonska, C.W. Gable, S.L. Painter, and H.S. Viswanathan, 2015a. dfnWorks: A discrete fracture network framework for modeling subsurface flow and transport. *Computers & Geosciences* 84:10–19. doi: 10.1016/j.cageo.2015.08.001.

Hyman, J.D., S.L. Painter, H. Viswanathan, N. Makedonska, and S. Karra S, 2015b. Influence of injection mode on transport properties in kilometer-scale three-dimensional discrete fracture networks. *Water Resources Research* 51:7289-7308. doi: 10.1002/2015WR017151.

Hyman, J.D., G. Aldrich, H. Viswanathan, N. Makedonska, and S. Karra, 2016. Fracture size and transmissivity correlations: Implications for transport simulations in sparse three-dimensional discrete fracture networks following a truncated power law distribution of fracture size. *Water Resources Research* 52:6472–6489. doi: 10.1002/2016WR018806.

Hyman, J.D., and J. Jiménez-Martínez, 2018. Dispersion and Mixing in Three-Dimensional Discrete Fracture Networks: Nonlinear Interplay Between Structural and Hydraulic Heterogeneity. *Water Resources Research* 0: doi: 10.1029/2018WR022585.

Hyman, J.D., S. Karra, J.W. Carey, C.W. Gable, H. Viswanathan, E. Rougier, and Z. Lei, 2018. Discontinuities in effective permeability due to fracture percolation. *Mechanics of Materials* 119:25-33. doi: 10.1016/j.mechmat.2018.01.005.

IT Corporation, 1998. Report and Analysis of the BULLION Forced-Gradient Experiment.

Kang, P.K., M. Dentz, T. Le Borgne, and R. Juanes, 2011. Spatial Markov model of anomalous transport through random lattice networks. *Physical Review Letters* 107 (2011) 180602.

Kang, P.K., M. Dentz, T. Le Borgne, S. Lee, and R. Juanes, 2017. Anomalous transport in disordered fracture networks: Spatial Markov model for dispersion with variable injection modes. *Advances in Water Resources* 106 (2017) 80-94.

Kang, P.K., T. Le Borgne, M. Dentz, O. Bour, and R. Juanes, 2015. Impact of velocity correlation and distribution on transport in fractured media: Field evidence and theoretical model. *Water Resources Research* 51 (2) 940–959.

Karpouzos, D.K., F. Delay, K.L. Katsifarakis, and G. de Marsily, 2001. A multipopulation genetic algorithm to solve the inverse problem in hydrogeology. *Water Resources Research* 37:2291–2302. doi: 10.1029/2000WR900411.

Karra, S., N. Makedonska, H.S. Viswanathan, S.L. Painter, and J.D. Hyman, 2015. Effect of advective flow in fractures and matrix diffusion on natural gas production. *Water Resources Research* 51:8646-8657. doi: 10.1002/2014WR016829.

Klimczak, C., R.A. Schultz, R. Parashar, and D.M. Reeves, 2010. Cubic law with aperture-length correlation: implications for network scale fluid flow. *Hydrogeology Journal* 18, 851–862. https://doi.org/10.1007/s10040-009-0572-6.

Konikow, L.F., G.Z. Hornberger, K.J. Halford, and R.T. Hanson, 2009. Revised multi-node well (MNW2) package for MODFLOW ground-water flow model: U.S. Geological Survey Techniques and Methods 6-A30, p. 67.

Krauße, T., and J. Cullmann, 2012. Towards a more representative parametrization of hydrologic models via synthesizing the strengths of Particle Swarm Optimisation and Robust Parameter Estimation. *Hydrology and Earth System Sciences* 16:603-629. doi: 10.5194/hess-16-603-2012

Le Borgne, T., M. Dentz, and J. Carrera, 2008. Spatial Markov processes for modeling Lagrangian particle dynamics in heterogeneous porous media. *Physical Review E* 78 026308.

Lewicki, J.L., J. Birkholzer, and C.-F. Tsang, 2007. Natural and industrial analogues for leakage of CO2 from storage reservoirs: identification of features, events, and processes and lessons learned. *Environmental Geology* 52:457. doi: 10.1007/s00254-006-0479-7

Lichtner, P.C., G.E. Hammond, C. Lu, S. Karra, G. Bisht, A. Benjamin, R. Mills, and J. Kumar, 2015. PFLOTRAN User Manual: A Massively Parallel Reactive Flow and Transport Model for Describing Surface and Subsurface Processes. Los Alamos National Lab. (LANL), Los Alamos, NM (United States); Sandia National Lab. (SNL-NM), Albuquerque, NM (United States); Lawrence Berkeley National Lab.

(LBNL), Berkeley, CA (United States); Oak Ridge National Lab. (ORNL), Oak Ridge, TN (United States); OFM Research, Redmond, WA (United States).

Liu, R., B. Li, Y. Jiang, and N. Huang, 2016. Mathematical expressions for estimating equivalent permeability of rock fracture networks. *Hydrogeology Journal* 24 (7) 1623-1649.

Long, J.C.S., P. Gilmour, and P.A. Witherspoon, 1985. A Model for Steady Fluid Flow in Random Three-Dimensional Networks of Disc-Shaped Fractures. *Water Resources Research* 21, 1105–1115. https://doi.org/10.1029/WR021i008p01105.

Los Alamos National Laboratory, 2013. LaGriT: Los Alamos Grid Toolbox. In: http://lagrit.lanl.gov. http://lagrit.lanl.gov/. Accessed March 29, 2017.

Maillot, J., P. Davy, R.L. Goc, C. Darcel, and J.R. de Dreuzy, 2016. Connectivity, permeability, and channeling in randomly distributed and kinematically defined discrete fracture network models. *Water Resources Research* 52, 8526–8545. https://doi.org/10.1002/2016WR018973.

Makedonska, N., S.L. Painter, Q.M. Bui, C.W. Gable, and S. Karra, 2015. Particle tracking approach for transport in three-dimensional discrete fracture networks. *Computational Geosciences* 19:1123-1137. doi: 10.1007/s10596-015-9525-4.

Makedonska, N., J.D. Hyman, S. Karra, S.L. Painter, C.W. Gable, and H.S. Viswanathan, 2016. Evaluating the effect of internal aperture variability on transport in kilometer scale discrete fracture networks. *Advances in Water Resources* 94:486-497. doi: 10.1016/j.advwatres.2016.06.010.

Margolin, G., B. Berkowitz, and H. Scher, 1998. Structure, flow, and generalized conductivity scaling in fracture networks. *Water Resources Research* 34 (9) 2103-2121.

Merrien-Soukatchoff, V., T. Korini, and A. Thoraval, 2012. Use of an Integrated Discrete Fracture Network Code for Stochastic Stability Analyses of Fractured Rock Masses. *Rock Mechanics and Rock Engineering* 45, 159-181. https://doi.org/10.1007/s00603-011-0136-7.

Mustapha, H., and K. Mustapha, 2007. A New Approach to Simulating Flow in Discrete Fracture Networks with an Optimized Mesh. SIAM Journal on Scientific Computing 29:1439-1459. doi: 10.1137/060653482.

Neuman, S.P., 2005. Trends, prospects and challenges in quantifying flow and transport through fractured rocks, *Hydrogeology Journal* 13 (1) 124-147.

Oda, M., 1985. Permeability tensor for discontinuous rock masses, *Geotechnique* 35 (4) (1985) 483-495.

Odling, N.E., 1997. Scaling and connectivity of joint systems in sandstones from western Norway. *Journal of Structural Geology* 19 (10) 1257-1271.

O'Malley, D., S. Karra, R.P. Currier, N. Makedonska, J.D. Hyman, and H.S. Viswanathan, 2016. Where Does Water Go During Hydraulic Fracturing? *Groundwater* 54:488-497. doi: 10.1111/gwat.12380.

Painter, S., and V. Cvetkovic, 2005. Upscaling discrete fracture network simulations: An alternative to continuum transport models. *Water Resources Research* 41(2).

Painter, S.L., C.W. Gable, and S. Kelkar, 2012. Pathline tracing on fully unstructured control-volume grids. *Computational Geosciences* 16, 1125-1134, https://doi.org/10.1007/s10596-012-9307-1.

Parashar, R., and D.M. Reeves, 2012. On iterative techniques for computing flow in large two-dimensional discrete fracture networks. *Journal of Computational and Applied Mathematics* 236:4712-4724, doi: 10.1016/j.cam.2012.02.038.

Pichot, G., J. Erhel, and J. de Dreuzy, 2012. A Generalized Mixed Hybrid Mortar Method for Solving Flow in Stochastic Discrete Fracture Networks. *SIAM Journal on Scientific Computing* 34:B86–B105. doi: 10.1137/100804383.

Poeter, E.P., and M.C. Hill, 1999. UCODE, a computer code for universal inverse modeling. *Computers & Geosciences* 25:457-462.

Pollock, D.W., 2012. User guide for MODPATH version 6: A particle tracking model for MODFLOW. U.S. Department of the Interior, U.S. Geological Survey.

Reeves, D.M., R. Parashar, and Y. Zhang, 2012. Hydrogeologic characterization of fractured rock masses intended for disposal of radioactive waste. INTECH Open Access Publisher.

Reeves, D.M., R. Parashar, G. Pohll, R. Carroll, T. Badger, and K. Willoughby, 2013. The use of discrete fracture network simulations in the design of horizontal hillslope drainage networks in fractured rock. *Engineering Geology* 163:132–143. doi: 10.1016/j.enggeo.2013.05.013.

Reeves, D.M., R. Parashar, K. Pohlmann, C. Russell, and J. Chapman, 2014. Development and calibration of dual-permeability flow models with discontinuous fault networks. *Vadose Zone Journal*, doi:10.2136/vzj2013.10.0183.

Reimus, P.W., and M.J. Haga, 1999. Analysis of tracer responses in the BULLION Forced-Gradient Experiment at Pahute Mesa, Nevada. Los Alamos National Lab (LANL), Los Alamos, NM (United States).

Renshaw, C.E., 1999. Connectivity of joint networks with power law length distributions. *Water Resources Research* 35 (9) 2661-2670.

Sahimi, M., 2011. Flow and transport in porous media and fractured rock: from classical methods to modern approaches. John Wiley & Sons.

Sayler, C., M. Cardiff, and M.D. Fort, 2018. Understanding the Geometry of Connected Fracture Flow with Multiperiod Oscillatory Hydraulic Tests. *Groundwater* 56, 276–287. https://doi.org/10.1111/gwat.12580.

Schumer, R., D.A. Benson, M.M. Meerschaert, and B. Baeumer, 2003. Fractal mobile/immobile solute transport. *Water Resources Research* 39(10).

Sun, N.-Z., 1994. Inverse Problems in Groundwater Modeling. 1994 edition, Springer.

Sund, N., D. Bolster, S. Mattis, and C. Dawson, 2015. Pre-asymptotic transport upscaling in inertial and unsteady flows through porous media. *Transport in Porous Media* 109 (2) 411-432.

Tsang, YW, Witherspoon PA (1981) Hydromechanical behavior of a deformable rock fracture subject to normal stress. *Journal of Geophysical Research: Solid Earth* 86:9287–9298. doi: 10.1029/JB086iB10p09287

Tsang C-F, Birkholzer J, Rutqvist J (2008) A comparative review of hydrologic issues involved in geologic storage of CO2 and injection disposal of liquid waste. *Environmental Geology* 54:1723–1737. doi: 10.1007/s00254-007-0949-6

Valera, M., Z. Guo, P. Kelly, S. Matz, V.A. Cantu, A.G. Percus, J.D. Hyman, G. Srinivasan, and H.S. Viswanathan, 2018. Machine learning for graph-based representations of three-dimensional discrete fracture networks. *Computational Geosciences* 22, 695–710. https://doi.org/10.1007/s10596-018-9720-1.

Vrugt, J.A., H.V. Gupta, W. Bouten, and S. Sorooshian, 2003. A Shuffled Complex Evolution Metropolis algorithm for optimization and uncertainty assessment of hydrologic model parameters. *Water Resources Research* 39:1201. doi: 10.1029/2002WR001642.

Vrugt, J.A., P.H. Stauffer, T. Wöhling, B.A. Robinson, and V.V. Vesselinov, 2008. Inverse Modeling of Subsurface Flow and Transport Properties: A Review with New Developments. *Vadose Zone Journal* 7:843-864. doi: 10.2136/vzj2007.0078.

Wang, Q.J., 1997. Using genetic algorithms to optimise model parameters. *Environmental Modelling & Software* 12:27-34. doi: 10.1016/S1364-8152(96)00030-8.

Witherspoon, P.A., J.S.Y. Wang, K. Iwai, and J.E. Gale, 1980. Validity of Cubic Law for fluid flow in a deformable rock fracture. *Water Resources Research* 16:1016–1024. doi: 10.1029/WR016i006p01016.

Yeh, W.W.-G., 2015. Review: Optimization methods for groundwater modeling and management. *Hydrogeology Journal* 23:1051–1065. doi: 10.1007/s10040-015-1260-3.

Zheng, C., and P. Wang, 1996. Parameter structure identification using tabu search and simulated annealing. *Advances in Water Resources* 19:215–224. doi: 10.1016/0309-1708(96)00047-4.

Zheng, C., and P.P. Wang, 2003. MGO–A modular groundwater optimizer incorporating modflow/mt3dms, documentation and user's guide. University of Alabama Groundwater Systems Research, Ltd., Tuscaloosa, AL.

STANDING DISTRIBUTION LIST

John Myers
UGTA Activity Lead
U.S. Department of Energy
Environmental Management Nevada Program
100 N. City Parkway, Suite 1750
Las Vegas, NV 89106
John.Myers@emcbc.doe.gov

Wilhelm Wilborn
Deputy Program Manager, Operations
U.S. Department of Energy
Environmental Management Nevada Program
100 N. City Parkway, Suite 1750
Las Vegas, NV 89106
Bill.Wilborn@emcbc.doe.gov

Ken Rehfeldt
Navarro
100 N. City Parkway, Suite 1750
Las Vegas, NV 89106
Ken.Rehfeldt@emnv.doe.gov

Jeff Berger
Nevada Field Office
National Nuclear Security Administration
U.S. Department of Energy
P.O. Box 98518
Las Vegas, NV 89193-8518
Jeff.Berger@nnsa.doe.gov

Ed Kwicklis
Los Alamos National Laboratory
P.O. Box 1663
Los Alamos, NM 87544
kwicklis@lanl.gov

Paul K. Ortego
Mission Support and Test Services, LLC
P.O. Box 98521
M/S NLV082
Las Vegas, NV 89193-8521
ortegopk@nv.doe.gov

Jeffrey Sanders
U.S. Geological Survey
Nevada Water Science Center
160 N. Stephanie St.
Henderson, NV 89074-8829
jvsanders@usgs.gov

Andy Tompson
Lawrence Livermore National Laboratory
P.O. Box 808, L-231
Livermore, CA 94551-0808
Tompson1@llnl.gov

Brian Haight
Navarro
100 N. City Parkway, Suite 1750
Las Vegas, NV 89106
Brian.Haight@emnv.doe.gov

Chuck Russell
Division of Hydrologic Sciences
Desert Research Institute
755 E. Flamingo Road
Las Vegas, NV 89119-7363
Chuck.Russell@dri.edu

Patrick Sawyer
DOE Program Manager
Division of Hydrologic Sciences
Desert Research Institute
755 E. Flamingo Road
Las Vegas, NV 89119-7363
Patrick.Sawyer@dri.edu

*****Nevada State Library and Archives
State Publications
100 North Stewart Street
Carson City, NV 89701-4285

Archives Getchell Library
University of Nevada, Reno
1664 N. Virginia St.
Reno, NV 89557
tradniecki@unr.edu

DeLaMare Library/262
University of Nevada, Reno
1664 N. Virginia St.
Reno, NV 89557
tradniecki@unr.edu

Document Section, Library
University of Nevada, Las Vegas
4505 Maryland Parkway
Las Vegas, NV 89154
sue.wainscott@unlv.edu

†Library Southern Nevada Science Center
Desert Research Institute
755 E. Flamingo Road
Las Vegas, NV 89119-7363

‡Martha DeMarre
Nuclear Testing Archive
Mission Support and Test Services (MSTS)
Contractor for the Nevada National Security Site
Mail Stop 400
PO Box 98521
Las Vegas, NV 89193-8521
demarrme@nv.doe.gov
(2 CDs)

§Office of Scientific and Technical Information
U.S. Department of Energy
P.O. Box 62
Oak Ridge, TN 37831-9939

All on distribution list receive one electronic PDF copy, unless otherwise noted.

***** 7 paper copies
† 2 paper copies; CD with pdf (from which to print)
‡ compact disc only
§ electronic copy (pdf) only